Christian-Albrechts-Universität zu Kiel
Mathematisch-Naturwissenschaftliche Fakultät
Institut für Experimentelle und Angewandte Physik
Arbeitsgruppe Plasmatechnologie

Computer modeling for improvement of a High Efficiency Multistage Plasma Thruster

Dissertation
zur Erlangung des Doktorgrades
der Mathematisch-Naturwissenschaftliche Fakultät
der Christian-Albrechts-Universität zu Kiel
vorgelegt von

Tim Brandt

Kiel, 2017

Erster Gutachter: Prof. Dr. Holger Kersten, Universität Kiel

Zweiter Gutachter: Prof. Dr. Claus Braxmaier, DLR Bremen / ZARM

Tag der mündlichen Prüfung: 29. November 2017

Abstract

This thesis presents an in-depth investigation of a downscaled High Efficiency Multistage Plasma Thruster (HEMPT) by computer modeling. The aim is to evaluate methods for improvements to reach the design goals of this downscaled thruster, which is also called micro-HEMPT. These design goals are low thrust and low thrust noise required for the LISA (Laser Interferometer Space Antenna) mission. In LISA, three formation flying spacecraft form a space-based laser interferometer for a mission to measure gravitational waves. The HEMPT was selected for downscaling, because it has a simple and robust design, similar to a HALL thruster, while its unique magnetic field topology enables efficient plasma confinement. The confinement is of high importance due to the fact that the neutral gas leaving the thruster increases the thrust noise. Therefore, the high ionization efficiency of the HEMPT must be retained in the downscaled version. To accomplish this, a detailed understanding of the physical properties of the micro-HEMPT is deemed necessary. Due to the small size of the micro-HEMPT internal plasma diagnostics is not feasible. However computer modeling is possible and a diagnostic for the thruster plume distribution can be used for validation. The so-called Particle-in-Cell (PiC) method was selected to perform these simulations. The PiC code used in this work is developed by the Computational Science group of the University Greifswald. Specific adaptations on this code were carried out to simulate the micro-HEMPT. To include the specific adaptations correctly, an understanding of the thruster specific plasma physics and this code was necessary, which is described in the theory section of the Ph.D. thesis. The scaling laws developed by Taccogna et al. are studied with focus on the practical application for the micro-HEMPT. While the physical characteristics and the operational conditions of regular sized HEMPTs are well understood, this was not the case for the micro-HEMPT. For the first time, the physical characteristics and the operational conditions of the micro-HEMPT are examined in detail by this Ph.D. thesis. The simulations show that the near exit region of the micro-HEMPT is particularly sensitive to downscaling due to the reduction in space charge. That means the reduced space charge causes a decreased bulk of positive potential at the thrusters exit, which amounts to less electrons that are pulled into the discharge chamber. These electrons gain high energy from the potential drop and are decisive for the performance, which consequently is reduced for the micro-HEMPT. Therefore several ways for improvements were investigated, such as improved geometry of the permanent magnets and their replacement by electromagnets. The limitations and drawbacks of these improvements became evident in detail. Moreover the conditions at the micro-HEMPT exit remain an inherent problem of the downscaling. In contrast the findings from this Ph.D. thesis may be applied in future into the opposite direction: from the regular

sized HEMPT upscaling to unusually large, high power HEMPT.

Abstrakt

Diese Dissertation präsentiert eine tiefgreifende Untersuchung eines herunterskalierten 'High Efficiency Multistage Plasma Thrusters' (HEMPT) mittels Computermodellierung. Das Ziel ist es Methoden zu untersuchen, welche für Verbesserungen nötig sind, um die Designziele dieses herunterskalierten Triebwerks zu erreichen, welches auch als Mikro-HEMPT bezeichnet wird. Diese Designziele sind niedriger Schub und niedriges Schubrauschen, was für die LISA (Laser Interferometer Space Antenna) Mission gefordert wurde. In LISA bilden drei in Formation fliegende Raumfahrzeuge ein weltraumgestütztes Interferometer zur Messung von Gravitationswellen. Das HEMPT wurde für die Herunterskalierung ausgewählt, weil es ein einfaches und robustes Design hat, ähnlich dem HALL Triebwerk, wobei seine einzigartige Magnetfeld-Topologie effizienten Plasma Einschluss ermöglicht. Der Einschluss ist von besonderer Wichtigkeit, aufgrund der Tatsache, das Neutralgas, welches das Triebwerk verlässt, das Schubrauschen erhöht. Daher muss die hohe Ionisationseffizienz des HEMPT auch in der herunterskalierten Version erhalten bleiben. Um dies zu erreichen, wird ein detailliertes Verständnis der physikalischen Eigenschaften des Mikro-HEMPTs für notwendig erachtet. Infolge der geringen Größe des Mikro-HEMPT ist Plasma Diagnostik in seinem Inneren nicht durchführbar. Aber Computer Modellierung für das Mikro-HEMPT ist möglich, und die experimentell vermessene Ionenstrahl-Verteilung kann zur Verifizierung genutzt werden. Für diese Simulationen wurde die sogenannte Particle-in-Cell (PiC) Methode ausgewählt. Der in dieser Arbeit verwendete PiC Code wurde von der AG Computational Sciences der Universität Greifswald entwickelt. Spezielle Anpassungen an diesen Code wurden durchgeführt, um den Micro-HEMPT zu simulieren. Um diese spezifischen Anpassungen korrekt einzuführen, war ein Verständnis der für dieses Triebwerk relevanten Plasma Physik und dieses Codes notwendig, welches in dem Theorie Abschnitt dieser Dissertation beschrieben wird. Die Skalierungsgesetze, welche von Taccogna et al. entwickelt wurden, werden untersucht mit besonderem Blick auf die praktische Anwendung für das Micro-HEMPT. Während die physikalischen Eigenschaften und die operationellen Bedingungen für das normalgroße HEMPT gut verstanden sind, war dies für das Mikro-HEMPT nicht der Fall. Durch diese Dissertation werden erstmalig die physikalischen Eigenschaften und operationellen Bedingungen eines Mikro-HEMPTs im Detail untersucht. Diese Simulationen zeigen, dass die Ausgangsregion des Mikro-HEMPT besonders empfindlich auf die Herunterskalierung reagiert, wegen der Reduzierung der Raumladung. Das heißt, eine reduzierte Raumladung bewirkt eine kleinere Ausbuchtung des positiven Potentials am Treibwerksausgang, was die Anzahl der Elektronen, welche in die Entladungskammer gezogen werden, reduziert. Diese Elektronen erlangen hohe Energie von der Potentialstufe und sind entscheidend für die Performance, welche folglich für das Mikro-HEMPT reduziert ist. Daher wurden mehrere Verbesserungswege untersucht, wie etwa verbesserte Ge-

ometrie für die Permanentmagneten und die Ersetzung dieser durch Elektromagneten. Jedoch wurden die Begrenzungen und Nachteile dieser Verbesserungen im Detail deutlich. Außerdem bleiben die Bedingungen am Ausgang ein dem Mikro-HEMPT innewohnendes Problem der Herunterskalierung. Im Gegensatz dazu könnten die Erkenntnisse aus dieser Dissertation zukünftig in die entgegengesetzte Richtung angewendet werden: vom normalgroßen HEMPT hochskalieren zu einen ungewöhnlich großen, hochleistungs-HEMPT.

Contents

1 Introduction and motivation

1.1 Requirements due to upcoming formation flying missions

Electrical thrusters have a broad and even growing range of applications. This range includes high power applications like orbital changing or interplanetary flight as well as low but very precise thrust for station keeping. One new application that expands the lower envelope, but also generates new requirements are formation flying satellites and space probes. In these missions typically two or more spacecrafts form a space-based laser interferometer. They can measure variations in the Earth's magnetic field [1], determine the space-time drag effect [2] or even should be able to detect gravitational waves [3]. The recent discovery of gravitational waves [4] by a ground-based interferometer emphasizes the opportunity of a quite new branch of astronomy [5] (Fig. 1.1). A space environment would be highly beneficial since it has much less disturbance and allows for interferometer arm-lengths that would be impossible to build on Earth. Therefore, space-based observations would allow for a much higher sensitivity and a much broader frequency range. However, since a spacecraft cannot be fixed in space thrusters are needed to keep them in position. Thereby, unprecedented requirements are necessary regarding low thrust and thrust stability for the interferometer to work properly. Also, continues operation for several years is needed. The thrust requirements reach into the micro-Newton regime and a very stable thrust is necessary where the root of the noise spectral density is $\leq 0.1\mu N/\sqrt{Hz}$. The minimum thrust of the most common electrical thrusters is more than one order of magnitude too high for this application. Hence, several attempts currently exist to downscale the common types into the thrust regime required for formation flying missions [6].

This work will focus on computer modeling for downscaling of a particular thruster type: The High Efficiency Multistage Plasma Thruster (HEMPT). The downscaled version is called micro-HEMPT. A breadboard level model [7] of this thruster type has been developed by Airbus Defence and Space. Details of the thruster type will be explained in more detail later. The project of development includes a highly precise thrust balance and a metrology system [8]. Moreover, the presented study will describe computer modeling to support this development. The computer modeling expands the cooperation with the Center of Applied Space Technology and Microgravity (ZARM) of the University

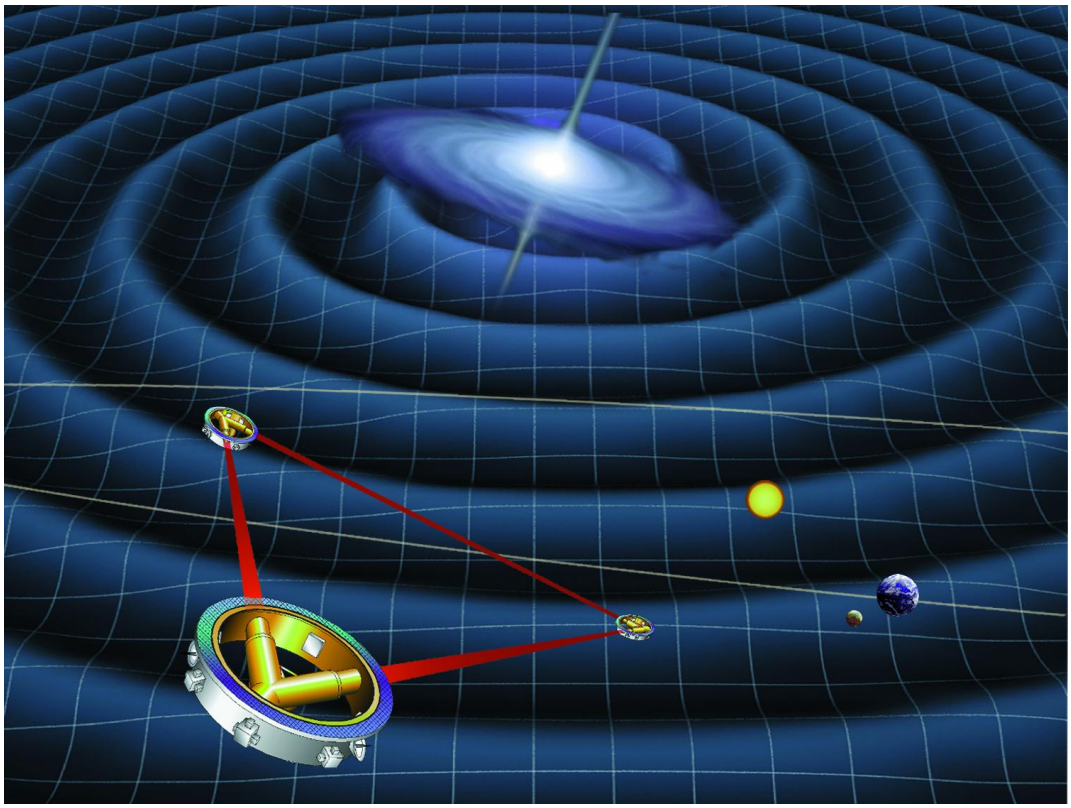

Figure 1.1: Artist's impression of LISA (Laser Interferometer Space Antenna), consisting of three satellites with laser beams for the detection of gravitational waves (© NASA).

Bremen, the German Aerospace Center (DLR), the Christian-Albrechts University (CAU) Kiel and the Institute of Physics of the University Greifswald.

1.2 A candidate for downscaling: HEMP thruster

The basic concept of HEMP thrusters (Fig. 1.2) originates in experiments with Traveling Wave Tubes (TWTs) at Thales Electron Devices, which has a periodic permanent magnet arrangement. The HEMPT design had been patented by Thales [9]. Except for its magnetic field topology it shares many similarities with a HALL thruster [10]. Basically, it is a grid-less thruster where magnetically trapped neutralizer-electrons act as a virtual cathode near the thrusters exit. An anode at the sealed end of the discharge chamber causes an electric potential difference. Thus, a direct current discharge is generated, where the electric field supplies the energy for electron-neutral impact ionization as well as for the acceleration of the ions. The magnetic field of a HEMPT is generated by a periodic arrangement of ring-shaped permanent magnets. These magnets

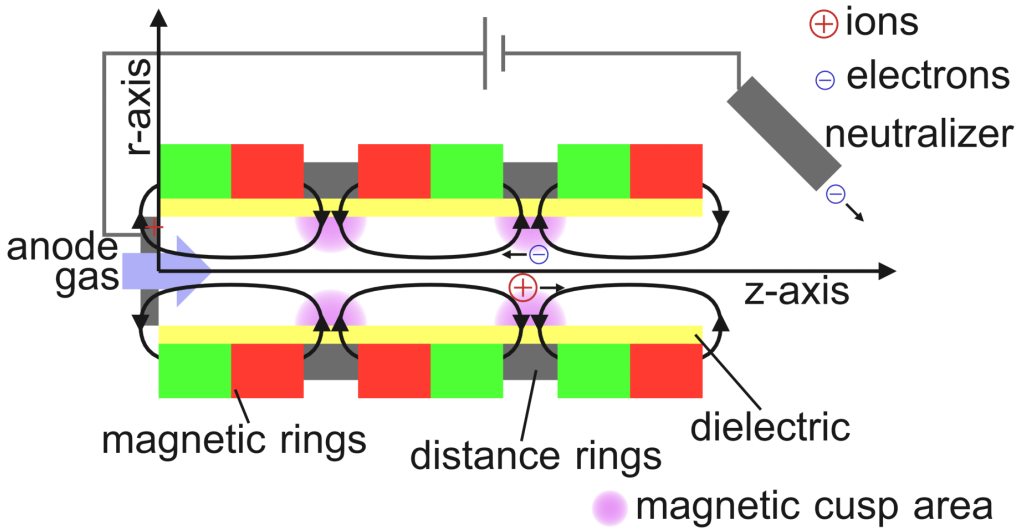

Figure 1.2: HEMP thruster principle.

have an alternating orientation parallel to the axial direction. The opposing magnetic fields create a so-called magnetic cusp with a radial magnetic field, while between the cusps the field is mostly axial. Following the magnetic field lines, the electrons can reach the discharge chamber wall only near the cusps [11]. The ions are not directly affected by the magnetic field, and a significant amount of them is accelerated outwards by the main potential drop near the thrusters exit, thereby generating the thrust. Due to the surface and space charges resulting from the electrons, the ions mostly reach the discharge chamber surface at the cusps region. The potential difference between the plasma bulk and the surface is relatively low. Therefore, the ion energy at impact on the surface does not reach the threshold for sputtering [12]. Consequently, the channel wall erosion is low which should help to satisfy one of the requirements, namely a continuing operation for several years. Due to the simplicity of its hardware components this thruster design seems applicable for downscaling.

1.3 Necessity of understanding the properties of a downscaled HEMP thruster

Keeping the properties of a common large HEMPT (Fig. 1.3 a) for a downscaled version (Fig. 1.3 b) is a great challenge. Obviously, due to the change in surface to volume ratio plasma wall interactions become more prominent and the plasma properties can be changed remarkably. Also the magnetic field strength and the neutral gas density need to apply to specific scaling laws in order to keep the properties [13]. The rate at which the neutral gas leaves the

Table 1.1: Typical design and operational parameters of a micro-HEMPT

Thruster channel length	$L = 14$ mm
Thruster channel radius	$R = 1.5$ mm
Discharge voltage	$U_a = 400$ V
Anode current	$I_a = 4.5$ mA
Mean magnetic field	$B = 0.6$ T
Neutral density	$n_n = 10^{21} - 10^{20}$ m^{-3}

thruster needs to be kept as low as possible since it creates significant thrust noise. The efficiency of the ionization needs to be as high as possible in order to reduce the amount of neutral gas which leaves the thruster. A high ionization also means high fuel efficiency which is desirable in regards to the long operational time. These requirements and the fixed (given) maximum magnetization of used permanent magnets put several constraints for the design. Strong deviations from the most typical ratios of discharge chamber length to radius are already experientially investigated [14]. The result of each design iteration needs to be well understood to make a successful plan to proceed for optimization. Unfortunately, downscaling makes measurements inside the thruster practically impossible. For example, the ceramic tubes of Langmuir probes would cause disturbances of the plasma properties since even a 0.5 mm radius would be a significant fraction of the discharge chamber radius. The only quantity measured from the interior of the thruster is the anode current. Furthermore, the anode voltage and the neutral gas flow are given in the experimental setup (table 1.1). Additionally, there is an external diagnostic which determines the intensity and energy of the ion beam with an angular resolution. For an optimization of the micro-HEMPT setup it is definitely desirable to have a computer modeling which calculates the internal properties of this thruster and which can be compared with the experimental values.

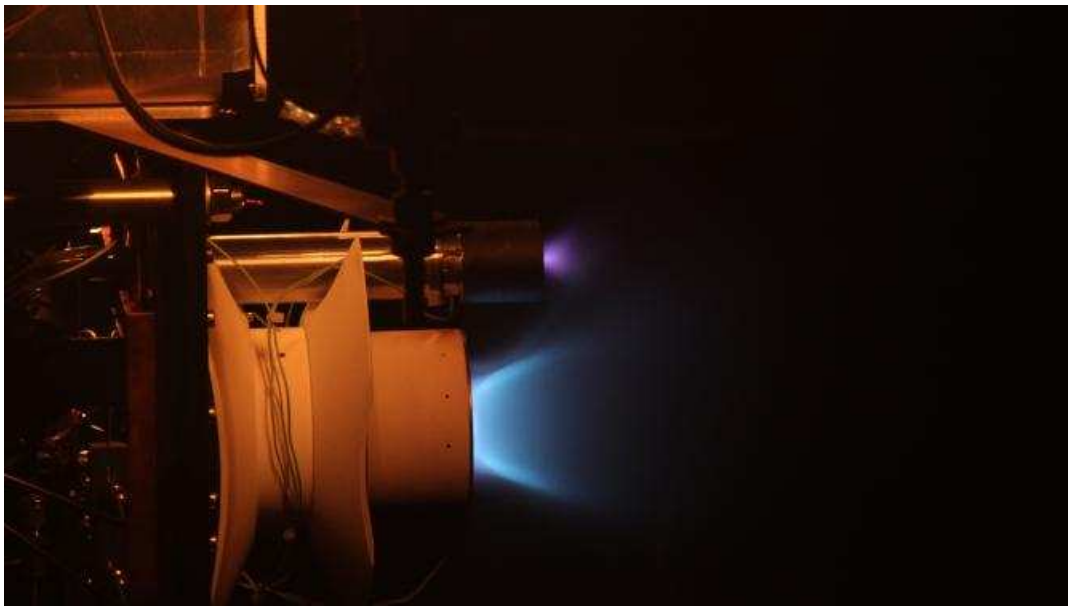

(a)

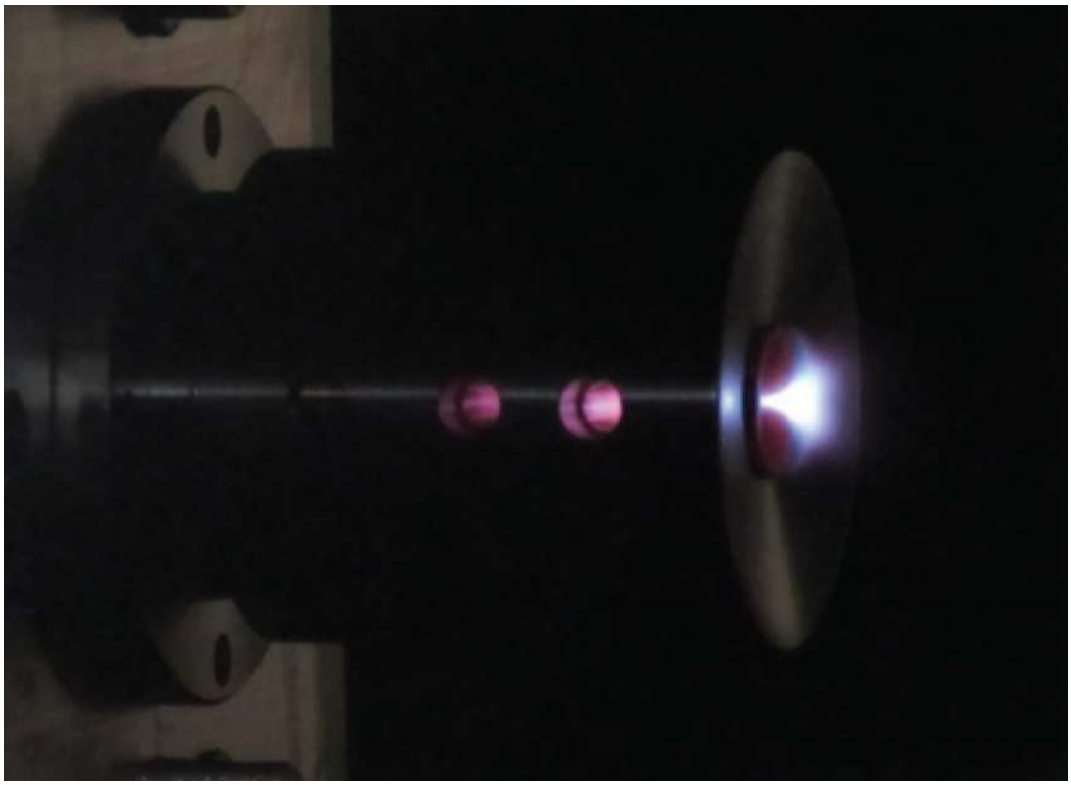

(b)

Figure 1.3: HEMP truster: a) orignal (large) version (©Thales. Small glow from the neutralizer on top.), and b) developed model of a downscaled configuration (©Airbus. Circular windows to see plasma discharge.).

1.4 Simulation approach

A common simulation approach for plasma devices is using a magnetohydrodynamic fluid simulation [15]. This approach is computationally relatively inexpensive since it does not need to trace single particles. For a thruster, however, the ions need to be treated as particles since the ion beam leaving the thruster cannot be regarded as a fluid (due to the decreasing density the ions become practically collisionless). Therefore, e.g. for a Hall thruster usually a hybrid model is used, where the ions are considered as individual particles and the electrons are treated as a magnetized fluid [16]. However, inside a HEMP thruster the magnetic cusps create a highly non-Maxwellian velocity distribution for the electrons [17]. Therefore, unfortunately the electrons cannot be treated as a fluid. Instead, they have to be considered as particle species, too [18].

These restrictions indicate that a fully kinetic code has to be used. For this purpose, a Particle-in-Cell (PiC) code with Monte Carlo collisions (MCC), which has been developed by the Computational Sciences Group of the University of Greifswald [19] is used in this work. It was applicable for modeling the micro-HEMPT without in-depth modification of the code. Parameters like particle source positions and magnetic field were adjusted to replicate the micro-HEMPT conditions.

The boundary conditions for the performed simulation are derived from the real experimental devices. Typical quantities from the already build and tested thrusters like anode voltage and neutral gas inflow are inherent parts of the model setup.

1.5 Outline of the thesis

In this thesis three interconnected major challenges are studied: First, application and usage with the Particle-in-Cell (PiC) code for use in micro-HEMPT plasma modeling. Second, self-similarity scaling laws and their effect on HEMP thrusters are investigated. These scaling laws were originally developed for HALL thrusters [20]. The physical properties of a HEMP thruster of regular size are well understood both by experiment and computer modeling. Possible changes of these properties that result from downscaling of the thruster type into the micro-Newton thrust regime, however, had not been well examined so far. Therefore, in this work the effects of downscaling from individual physical properties to complete HEMP thruster will be investigated. Thirdly, attempts are made to use the optained knowledge in order to retain the performance characteristics of the original sized HEMPT for the micro-HEMPT.

Chapter (2) will provide a detailed overview of the plasma properties typical for this thruster type whose understanding is essential for the simulations. It will include general topics like Debye length but also thruster specific ones such as Bohm diffusion.

The Particle-in-Cell (PiC) simulation [18] method (PiC code developed by the computational science group of the University Greifswald) will be described and discussed in chapter (3) along with its relation to the plasma properties of the investigated thruster type.

Chapter (4) is based on the self-similarity scaling schema by Taccogna et al. [13]. For this work, however, a more detailed derivation of scaling schema has been developed which is presented in this chapter. For further importance will be the common praxis in thruster simulation to use the self-similarity for saving computational time. Particular care needs to be taken due to possible deviations from the original system that is to be simulated.

Chapter (5) deals with the practical restrictions in the application of the self-similarity scaling schema due to the use of permanent magnets with limited field strength. The basis is a fundamental model of a cylindrical discharge with an axial magnetic field. This method is used to describe this downscaling by analytical means. As the next step, the same kind of models will be simulated by use of the PiC-method. These models are used to investigate the effects of downscaling in more detail. In particular, there are two downscaled versions with increased and non-increased magnetic field, whereas the latter represents a micro-HEMP thruster. Comparisons between the versions are made to validate the previous analytical considerations. This chapter ends the theoretical part and begins the computer modeling part of this work.

In chapter (6) this simulation is followed by computer modeling for the same geometry but with a magnetic cusp. This approach will be closer to the real thruster but still be comparable to the previous run. The effect of the material properties concerning the magnetic field strength will be considered for downscaling, too.

Next, the application of the self-similarity scaling schema for downscaling of an actual thruster will be investigated. The simulation will be described and presented in chapter (7). Analyses of the results will be performed both for the discharge channels interior as well as the outer thrusters exit region. The simulation is compared with the experimental results from a downscaled thruster which has already been build (micro-HEMPT) [21].

In he following chapter (8) various options to improve a downscaled HEMPT

by modified elements, including an experiment, will be evaluated. The limits of the technically possible (although not necessarily technically feasible) modifications will also be simulated by strengthening the magnetic field using superconducting electromagnets.

Finally, the study will conclude in chapter (9) with a simulation of an unscaled version of the same design to determine the scaling characteristics by direct comparison. The conclusion will provide a summary of the results and an outlook for further investigations in the future.

2 Physical properties of the simulated plasma

2.1 Origin of the simulated plasma device

Ion-based propulsion systems like HEMP and Hall thrusters have some similarities with a direct-current plasma discharge (Fig. 2.1). In both thruster types electrons are accelerated by an externally applied drop of the electric potential. The electrons transfer a large amount of their kinetic energy (received by acceleration in the electric field) by impact ionization. Additional electrons are created by the ionization events so that the discharge is ignited by an avalanching effect. The discharge reaches a steady state when the amount of generated ions and their losses are in equilibrium [22].

A common case of plasma is a glow discharge generated in a low-pressure gas tube at about 100 to 1000 Pa. The gas is usually one with a low ionization threshold, like xenon or argon. The potential drop is applied by metallic electrodes with the anode being at one end and the cathode at the other end. Most of this potential drop is at the cathode, where most of the secondary electrons and ions are generated as well as a significant amount of excitation. This is called the negative glow region. Near this region, the energy of the electrons is insufficient to excite neutral atoms, which is visible in a lack of glow. Therefore, this area is called the Faraday dark space. Usually, the largest volume is taken by the positive column. Even though the electric field of the positive column

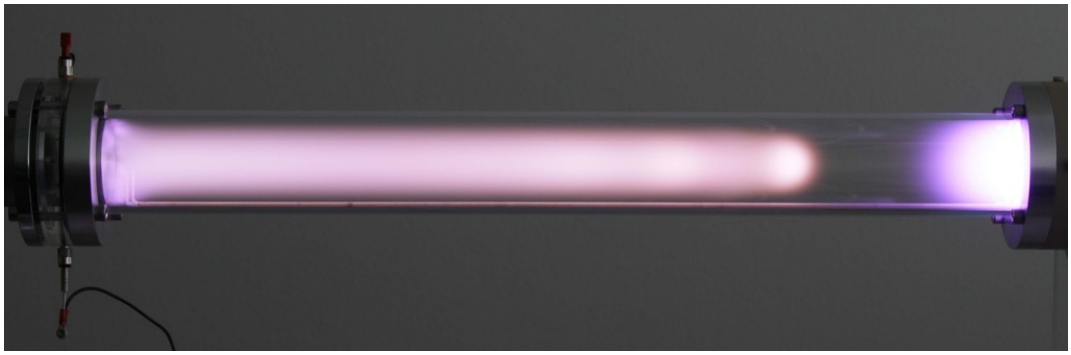

Figure 2.1: A typical gas discharge tube. © Max Planck Institute for Plasma Physics.

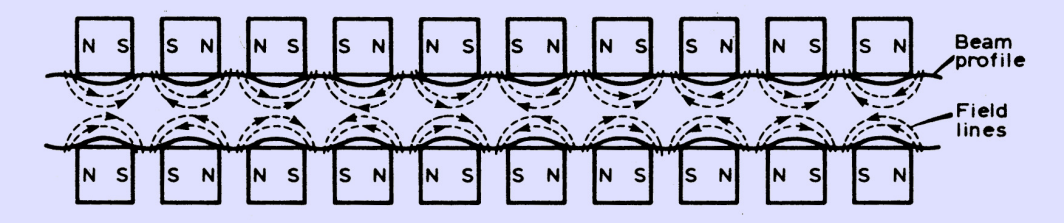

Figure 2.2: Cusped magnetic field in a Traveling Wave Tube. © Greek Microwave Group.

is weak, electrons energy gain is sufficient to reach the ionization threshold.

Within a long cylindrical discharge chamber, most losses (of ions and electrons) are to the cylindrical wall, by radial diffusion. One end of the HEMP thrusters cylindrical discharge chamber is open and losses of ions at this end are desired, since they are the reaction mass of the drive generating the thrust. Like for other electric thrusters, one main aim of a HEMPT design is to shift the ion losses towards the open end and away from the cylinder walls. This is achieved by a cusped (convex) magnetic field. It is based on experience at Thales Electron Devices with Traveling Wave Tubes using periodic focusing by permanent magnets (Fig. 2.2). This specific magnetic field topology is generated by an arrangement of toroidal permanent magnets with periodically alternating polarity. The field focuses the plasma electrons to the discharge chambers central axis and reduces losses to the walls.

2.2 Debye length

In a natural state, a gas always has a certain, if low, degree of ionization. A gas is called to be in a plasma state if its charged particle density is high enough that the frequency of the electron oscillations (electron plasma frequency) is higher the electron-neutral collision frequency, the distance of the electrostatic shielding is small compared to the plasma dimensions and there is a statistically significant number of charged particles within this shielding range. In general, plasmas are 'quasineutral', the number of electrons and ions is almost equal. Nevertheless, internal electric fields do exist due to variations in the charge on smaller scales. These variations are compensated on larger scales by the electrostatic shielding, which will be described in the following.

For the descriptions within the simulations we will differentiate between the non-ionized atoms, which we call the background neutral gas, and the actual plasma consisting of ions and electrons. The characteristic distance of the electrostatic shielding is called Debye length. Beyond this distance the remaining

plasma is shielded from an electrostatic disturbance. This disturbance can be described as a small object of charge Q inside the plasma. For simplicity, this object is assumed to be a point charge. This charge generates a radial electric field E. Therefore, it is appropriate to define a spherical coordinate system whose origin is at the position of this object. Due to this choice, the polar and azimuthal angle components of the electric field are zero and need not to be considered. Only the radial distance r needs to be taken into account. Within this coordinate system the charge density $\rho(r)$ can be described mathematically by a Dirac delta function $\delta(r)$, the spike is at $r = 0$:

$$\rho(r) = Q\delta(r) \ .$$

The relation between the electric potential Φ and the charged plasma particles is defined by the Poisson equation:

$$\epsilon_0 \Delta\Phi = \sum q_j n_j - \rho(r) \ . \tag{2.1}$$

Where q_j and n_j are the charge carried by each particle and the density of each particle species, respectively (species type is indexed with j). ϵ_0 is the vacuum permittivity.

The general particle movement, described by the velocity vector $\boldsymbol{v_j}$, is altered in response to the Lorentz force $\boldsymbol{F_{L,j}}$:

$$\boldsymbol{F_{L,j}} = q_j \cdot (\boldsymbol{E} + \boldsymbol{v_j} \times \boldsymbol{B}) \ , \tag{2.2}$$

with $\boldsymbol{E}$ and $\boldsymbol{B}$ being the electric and magnetic field vectors, respectively.

Examining a case where no magnetic field is present, it is reduced to the Coulomb force;

$$\boldsymbol{F_{C,j}} = q_j \cdot \boldsymbol{E} = q_j \cdot \nabla\Phi \ . \tag{2.3}$$

If the particles are assumed to be in thermodynamic equilibrium with temperature T each particle species velocity ($\boldsymbol{v_j}$) probability has a Maxwell-Boltzmann distribution [23],

$$f_j(v_j) = 4\pi v_j^2 \cdot \left(\frac{m_j}{2\pi k_B T_j}\right)^{3/2} exp\left(\frac{-m_j v_j^2}{2k_B T_j}\right) \ , \tag{2.4}$$

where m_j is the particle's mass and k_B the Boltzmann constant.

If the electric potential is defined as a thermodynamic mean field the concentration of the particles is the Boltzmann distribution,

$$n_j(r) = n_{0,j} \cdot exp\left(\frac{-q_j\Phi}{k_B T_j}\right) \ , \tag{2.5}$$

where $n_{0,j}$ is the mean particle density in the plasma bulk.

In general, for an ideal plasma a high temperature and, thus, weak coupling can be assumed: $q_j\Phi(r) << k_B T_j$. Then a simple Taylor expansion of the exponent is sufficient:

$$exp\left(\frac{-q_j\Phi}{k_B T_j}\right) \cong 1 - \left(\frac{-q_j\Phi}{k_B T_j}\right) \ .$$

This simplifies to the linearized Poisson-Boltzmann equation [24]:

$$\epsilon_0 \Delta\Phi = -\sum q_j n_{0,j} + \sum \frac{n_{0,j} q_j^2}{k_B T_j}\Phi - \rho(r) \ .$$

The first term on the right hand side of the equation vanishes for an electric neutral system, and we can define the characteristic length scale

$$\lambda_D^{-2} = \sum \frac{-n_{0,j} q_j^2}{\epsilon_0 k_B T_j} \ , \tag{2.6}$$

by considering the differential equation

$$\Delta\Phi = \lambda_D^{-2}\Phi - \frac{\rho(r)}{\epsilon_0} \ .$$

For the point charge $\rho(r) = Q\delta(r)$, this yields:

$$\Phi(r) = \frac{Q}{r} \cdot exp\left(\frac{r}{\lambda_D}\right) \ . \tag{2.7}$$

The point charge that represents the disturbance is exponentially shielded by the collective of charged particles.

The characteristic length of electrostatic shielding, λ_D, is called the Debye length. In the simplest case for a plasma the charged particles are singly charged ions and electrons, with $n_{0,i}$ and $n_{0,e}$ being their mean densities. Their

charges q_i and q_e are the positive and negative elementary charges, respectively. Then the Debye length is:

$$\lambda_D = \sqrt{\frac{\epsilon_0 k_B T_e}{n_{0,e} q_e^2} + \frac{\epsilon_0 k_B T_i}{n_{0,i} q_i^2}} \, .$$

In the case of fast changing disturbances the ions inertia is too high to play a significant role in the Debye shielding. Then the Debye length can be assumed as

$$\lambda_D = \sqrt{\frac{\epsilon_0 k_B T_e}{n_{0,e} q_e^2}} \, , \tag{2.8}$$

which scales with $\sqrt{\frac{T_e}{n_{0,e}}}$.

In this definition, every single electron or ion can be defined as the point charge. Contemplating this, it becomes evident that the particles only directly influence each other within a sphere whose radius is the Debye length. Only if this Debye sphere includes a statistically significant number of particles, this definition is effective.

For PiC simulations this implies that the computational grid must resolve the Debye length λ_D in space to display the plasma properties correctly. Therefore, the grid cell size ΔX must satisfy the condition $\Delta X \leq \lambda_D$. If this condition is not fulfilled it can result in numerical instabilities, which may cause non-physical self-heating. It can cause, for example, exponential growth of the particle numbers, which finally render the entire simulation useless. As it can be seen in equation (2.8), the Debye length becomes smaller with increasing electron density. Therefore, if a uniform grid is used, and the plasma density is non-uniform, the grid cell size must resolve the volume of the highest plasma density.

2.3 Gyration motion

For typical plasma discharges, the effect of gravity is negligible since a particle hits the discharge chamber wall before its trajectory is significantly altered by the gravitational force. Under this condition, a collision-less trajectory of each charged particle is solely determined by the Lorentz force. In case that only a magnetic field and no electric field exists the Lorentz force reduces to $\boldsymbol{F} = q \cdot \boldsymbol{B} \times \boldsymbol{v}$, which is always perpendicular to the direction of the charged particles motion.

Without loss of generality a Cartesian coordinate system with e_x, e_y, e_z shall be oriented such that its z-axis being parallel to the direction of an unidirectional magnetic field. Then for a particle with an initial speed of v_x, v_y, v_z, the z-component of the Lorentz force is zero since v_z and the magnetic field are parallel. Therefore the z-velocity of the particle is not altered by the magnetic field. The particle motion can be distinguished between velocity components parallel and perpendicular to the magnetic field, which are $v_{||} = v_z$ and $v_\perp = \sqrt{v_x^2 + v_y^2}$, respectively.
For the Cartesian components v_x, v_y, v_z, their differential equations of motion are

$$\ddot{v}_x = -\frac{q}{m} B v_y \ ,$$

$$\ddot{v}_y = \frac{q}{m} B v_x \ ,$$

$$\ddot{v}_z = 0$$

(with $B_x = B_y = 0$ and $B = B_z$ due to choice of coordinate system) resolving to [25]:

$$v_x = v_\perp \cdot sin(\omega_g t + \alpha) \tag{2.9}$$

$$v_y = v_\perp \cdot cos(\omega_g t + \alpha) \ , \tag{2.10}$$

and

$$v_z = const. \ . \tag{2.11}$$

This is a gyration motion with the frequency $\omega_g = q \cdot B/m$. α is an arbitrary phase angle that can be set to zero. The center of the gyration motion can be defined as a guide center which moves with the constant velocity v_z. The particles path is then a helix with a guide line which itself is equal to a magnetic field line.

The gyration radius r_g can be easily derived from equalizing the Lorentz force and the centrifugal force, giving $r_g = v_\perp \cdot m/e \cdot B$. For ions, the gyration radius r_g is about the same size of the micro-HEMPTs discharge chamber or even larger. Hence, their gyration motion can be neglected. For the electrons the radius is significantly smaller and with their helical motion on the macroscopic level they follow the magnetic field lines. To calculate this movement, the gyration part of this motion must be resolved by the time steps Δt of the PiC simulation. A typical value is $\Delta t \leq 0.2/\omega_g$.

2.4 Magnetic mirror

The magnetic flux density inside a micro-HEMPTs discharge chamber is highly non-uniform due to its increased strength at the magnetic cusps. Therefore, electrons following the magnetic field lines on their helix trajectory pass through increasing flux density where the field lines are converging. Due to the distance (gyration radius) from its guide line a gyrating electron experiences a field component that is perpendicular to this line (due to the converging field lines).

This field component generates a Lorentz force parallel to the guide line and, thus, parallel to the direction of motion of the electrons guide center. It slows down and can finally invert this motion. Therefore it is called 'magnetic mirror effect'. This effect can be described by use of an electrons magnetic moment μ_M, which can be expressed as [26]:

$$\mu_M = \frac{m_e v_\perp^2}{2B} \ . \tag{2.12}$$

As usual, m_e is the mass of the electron. Under the condition that only a magnetic field acts on the electrons, both the kinetic energy and the magnetic moment of the particle remain constant. With rising B the perpendicular velocity $v_\perp$ must equally rise for the magnetic moment to be constant. For the kinetic energy $E = \frac{m_e}{2}(v_\perp^2 + v_{||}^2)$ to remain constant, consequently $v_{||}$ must drop.

In a PiC simulation the Boris pusher, which will be explained in detail later, solves the motion of the electrons by direct application of the Lorentz force and, therefore, includes the mirror effect.

2.5 Magnetic cusp

The opposing cylindrical ring magnets in a HEMPT create so-called magnetic cusps [27] of the magnetic fields. Therefore, this type of thruster is also generalized as 'cusped field thruster'. Halfway between the magnets, their axial field components cancel out each other and the field has only a radial component. The highest radial component within the discharge chamber is just on its interior surface. At the same z-distance at $r = 0$ both components are zero (zero field point). This field configuration improves the magnetic confinement of the electrons. Between the cusps, the field is mostly axial, and the electrons, following the magnetic field lines, can reach the interior surface only near the cusps. The magnetic mirror effect reduces the percentage of electrons that actually reach the cusp. This mirror ratio R_{mirror} is described as [28] :

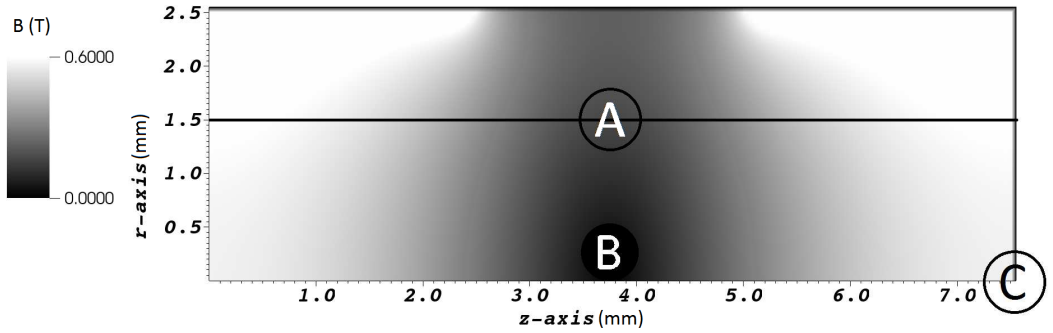

Figure 2.3: Magnetic flux density example. A: point at discharge chamber surface, cusp position, B: point with zero magnetic flux, C: point of high magnetic flux (within discharge chamber).

$$R_{mirror} = \frac{B_{max}}{B_{min}} \ . \tag{2.13}$$

In the case of an electrons starting point which lies in an area of lower flux density (otherwise, the electrons could not be 'reflected'), the flux densities at this point and the endpoint of its guideline (e.g. a wall) are labeled B_{min} and B_{max}, respectively. Then R_{mirror} is the probability of an electron being reflected along this track. Whether an individual particle will be reflected or not can be seen by the following criteria [29]:

$$\frac{v_\perp}{v} > \frac{1}{\sqrt{R_{mirror}}} \ . \tag{2.14}$$

The initial velocity vector is again separated into $v_\perp$ and $v_{||}$, while v is the absolute value of this vector. Fig. 2.3 shows an example of a magnetic field configuration within a section of a HEMPTs discharge chamber. For particles starting at point `B`, due to its magnetic flux density of 0 T, they all would be reflected before reaching the point `A` at the discharge chambers surface who is at 0.2 T. Particles starting at point `C`, at a flux density of 0.6 T, would not be reflected before reaching the surface point. Design changes for improvement might increase the flux density at point `A` and/or reduce it at point `C`. The shape of the field lines also reduces the movement of the electrons in z- direction with regards to crossing from one side of the cusp to the other. It can be shown, that near the zero field point (`A`) the electrons gyration radii become so large that the model of the guide line becomes invalid and crossing the cusp can occur [30]. Diffusion, which will be discussed later, causes additional crossing as well as additional losses towards the wall. Obviously, zero crossing of the electrons is undesirable, since it would result in zero net current flow to the anode, and, thus, zero power consumption of the thruster. On the other hand,

high crossing would result in many high energy electrons reaching the anode before dissipating their energy into the plasma.

2.6 Plasma frequencies

The HEMPTs discharge chamber is in principle a direct current discharge with both the electron source and the anode potential constant in time. Therefore, the plasma has no driven oscillations. Nevertheless, random fluctuations can cause oscillations inside the plasma. For example, a volume of electrons displaced by a distance x outward an equal volume of ions generates an electric field that pulls the electrons back to their rest position.

The resulting motion is a harmonic oscillation where the electrons displacement x and their speed v_e are time dependent. They can be described by a perturbation approach, for the electron density n_e,

$$n_e = n_{e1} + n_{e0} \ , \tag{2.15}$$

with $n_{e1} << n_{e0}$ and hence $n_{e0} \cong n_e$. Here n_{e0} is the background density which is assumed to be isotropic, and n_{e1} is the density perturbation. The same approach will be taken for the velocity v_e and the electric field E. We assume the case of cold electrons, e.g. v_{e0} is zero. Also, there shall be no other sources for electric fields, e.g. E_0 is zero as well. With the harmonic approach, these three variables are of the form:

$$\approx exp(i(kx - \omega t)) \ . \tag{2.16}$$

Where as usual k is the the wavenumber, ω the angular frequency and i the imaginary unit.

The electrons momentum equation is:

$$m_e n_e \left[\frac{\partial v_e}{\partial t} + v_e \nabla v_e \right] = -e n_e E \ .$$

Due to $E_0 = 0$ and $v_{e0} = 0$ we have $E = E_1$ and $v_e = v_{e1}$. Also the term $v_{e1} \nabla v_{e1}$ is negligible since $v_{e1}^2 << v_{e1}$. Dividing by n_e gives:

$$m_e \left[\frac{\partial v_{e1}}{\partial t} \right] = -e E_1 \ . \tag{2.17}$$

The electrons continuity equation is [31]:

$$\frac{\partial(n_{e0}+n_{e1})}{\partial t}+\nabla((n_{e0}+n_{e1})v_{e1})=0\ .$$

From the bracket $n_{e0}v_{e1}+n_{e1}v_{e1}$ the right term is negligible compared to the left one, and with $\partial n_{e0}/\partial t=0$, we have:

$$\frac{\partial n_{e1}}{\partial t}+n_{e0}\nabla v_{e1}=0\ . \tag{2.18}$$

The previously mentioned electric field is defined by Gauss's law:

$$\nabla E_1=-\frac{e}{\epsilon_0}n_{e1}\ . \tag{2.19}$$

With approach (2.16) in the Fourier space the equations (2.17), (2.18) and (2.19) are

$$-im_e\omega v_{e1}=-eE_1\ , \tag{2.20}$$

$$-i\omega n_{e1}=-n_{e0}ikv_{e1} \tag{2.21}$$

and

$$ikE_1\epsilon_0=-en_{e1}\ . \tag{2.22}$$

This set of linearized differential equations can be brought into matrix form, where its determinant can be used to obtain the solution [32]:

$$\omega_{pe}=\omega=\sqrt{\frac{n_e e^2}{\epsilon_0 m_e}}\ . \tag{2.23}$$

This case describes a standing wave which is independent of its wavelength. Therefore, this oscillation has an infinite phase velocity while its group velocity is zero. The electron density is the only variable that determines this electron plasma frequency ω_{pe}. Due to that, for practical applications it can be approximated as:

$$\frac{\omega_p e}{2\pi}=f_p\approx 8980\sqrt{n_e}\mathtt{Hz}\ .$$

This is arguably the fastest plasma oscillation due to the low mass of the electrons. Therefore, a plasma simulation which treats electrons as particles must resolve this oscillation. In that case the time steps must be smaller than the period of this oscillation.

Perturbations of the ion distribution are on a much larger timescale than it is the case for electrons due to the higher mass of the ions. For ion perturbations, the other species (here the electrons), cannot be considered at rest and, consequently, cannot assumed to be a static background. The electrons have a Boltzmann distribution.

As defined before, for a species of single positive charged ions (density n_i), due to charge neutralization (equal amount of positive and negative charges in a volume) each charged particles density n is approximately $n_i = n_e = n$. The deviation through these ion waves is so small that these conditions can be assumed to be valid.

The electric potential of the wave originates in different pressure perturbations for the ions and electrons. These perturbations are part of a polytropic process which is

$$\nabla p = \gamma k_B T \nabla n \tag{2.24}$$

γ is the adiabatic index, which is γ_i and γ_e for the ions and electrons, respectively.
With the pressure p_i and p_e the ion and electron momentum equations are:

$$m_i n \left[\frac{\partial v_i}{\partial t} + v_i \nabla v_i \right] = -enE - \nabla p_i$$

and

$$m_e n \left[\frac{\partial v_e}{\partial t} + v_e \nabla v_e \right] = -enE - \nabla p_e \ .$$

The perturbation approach is also taken for the charged particles density ($n = n_1 + n_0$) and the ion velocity ($v_i = v_{i1} + v_{i0}$). Again the terms $v_i \nabla v_i$ and $v_e \nabla v_e$ can be neglected since $v_{i0} \cong 0$, $v_{e0} \cong 0$ and $v_{i1}^2 << v_{i1}$, $v_{e1}^2 << v_{e1}$.

By defining the fields by the electric potential, $E = \nabla \Phi$, and substituting pressure with density according to (2.24) we obtain:

$$m_i n \left[\frac{\partial v_i}{\partial t} \right] = -en \nabla \Phi - \gamma_i k_B T_i \nabla n \tag{2.25}$$

and

$$m_e n \left[\frac{\partial v_i}{\partial t} \right] = -en\nabla\Phi - \gamma_e k_B T_e \nabla n \ . \tag{2.26}$$

For these equations, which describe the motion of ions and electrons, we can also assume the harmonic perturbation approach; e.g. we can Fourier transform and linearize equation 2.25:

$$-im_i\omega n_0 v_i = -in_0 ke\Phi_1 - i\gamma_i k_B T_i k n_1 \ . \tag{2.27}$$

For the electrons, whose mass m_e is negligible compared to the ion mass, we can neglect the left term of equation 2.26 (containing m_e). The remaining two terms can be written as:

$$-e\nabla\Phi = \gamma_e k_B T_e \frac{\nabla n}{n} \ .$$

The electrons behave isothermally, therefore it is $\gamma_e = 1$. This equation can be solved for n by integration. As expected, the electrons are Boltzmann distributed:

$$n = n_0 exp\left(\frac{e\Phi}{k_B T_e}\right) \ .$$

We can use the assumption of $e\Phi << k_B T_e$ for Taylor expansion to achieve the second order term in dependence on the first order term:

$$n_1 = n_0 \frac{e\Phi}{k_B T_e} \ . \tag{2.28}$$

Both ions and electrons fullfill the continuity equation:

$$\frac{\partial n}{\partial t} + \nabla n v = 0 \ .$$

Again using harmonic perturbation approach and using the expression of n_1 we obtained, one can find the ion velocity [33]:

$$v_i = \frac{\omega}{k} \frac{e\Phi}{k_B T_e} \tag{2.29}$$

Substituting the expressions for n_1 (2.28) and v_i (2.29) in the linearized ion equation of motion (2.27), it becomes:

$$m_i \omega n_0 \frac{\omega}{k} \frac{e\Phi}{k_B T_e} = n_0 k e\Phi + \gamma_i k_B T_i k n_0 \frac{e\Phi}{k_B T_e} \ .$$

We can solve for the angular frequency in dependence of k, which gives the dispersion relation:

$$\omega(k)^2 = k^2 \left(\frac{k_B T_e + \gamma_i k_B T_i}{m_i} \right) \ .$$

γ_i is 3, since the wave-motion of the ions is one-dimensional (one-directional), hence, its number of degree of freedom f_d is 1 and $\gamma = f_d + 2/f_d$.

The waves are dispersion-less, expressed as $\omega(k) = k \cdot v$, the resulting phase velocity is:

$$v^2 = \frac{k_B T_e + 3 k_B T_i}{m_i} \ .$$

We recognize that the motion of the ion waves is not only dependent on the ion temperature but also on the electron temperature. If the electrons are much hotter than the ions, which is often the case in collisionless plasmas, the right term of the numerator, containing the ion temperature, can be neglected. These waves are called ion acoustic waves due to their relation to pressure gradients. There are numerous other types of ion waves depending on their relation to the magnetic field. For the plasma devices investigated in this work, the effect of the magnetic field on the ions is negligible. Therefore, these types of ion waves will not be discussed.

2.7 Plasma frequencies - azimutal oscillations

In a cylindrical discharge chamber, the ion distribution can have axial, radial and azimuthal oscillations. These oscillations cause fluctuations in charge density; and electric fields in all three spatial directions are generated. The azimuthal fields are the cause of the so-called Bohm diffusion, which will be discussed in chapter 2.9.

2.8 Classical diffusion

As discussed in chapter 2.3, if only the magnetic part of the Lorentz force is acting upon the electrons, they are bound due to their gyration motion to

the magnetic field lines. Collisions with neutral atoms cause a force on the electrons which result in a change of their velocity vector that can be regarded as instantaneous. If no magnetic field is present, due to these collisions a given assembly of electrons spreads out in a diffusive process with the diffusion coefficient D:

$$D = \frac{\lambda^2}{\tau} \ .$$

λ is the mean free path and τ the average time between collisions, which is the inverse of the collision frequency f:

$$\tau = \frac{1}{f} \ .$$

In a magnetized plasma, the electrons usually undergo many gyrations before a collision ($f << \omega_g$).
Each collision changes (at least rotates) the electrons velocity vector. Consequently, the electrons guide center is offset by about one gyroradius. Hence the mean free path is approximately equivalent to the gyroradius, and the diffusion coefficient becomes:

$$D_\perp = \frac{r_g^2}{\tau} = r_g^2 f \ . \tag{2.30}$$

This coefficient describes the mobility of the electrons perpendicular to the magnetic field lines. Without collisions ($f = 0$), this perpendicular mobility and, hence, the diffusion coefficient would be zero.
Since $r_g \cong 1/B$, we have the relation to the magnetic flux density as $D_\perp \cong 1/B^2$.

2.9 Bohm diffusion

Experiments with plasma devices like Hall thrusters showed a diffusion larger than the classical model would predict [34]. Also, diffusion does not follow the relation $\cong 1/B^2$, but rather $\cong 1/B$. A description for this anomalous diffusion needed to be found. If the collision frequency $2\pi f$ is higher than the gyration frequency ω_g, the electrons can be seen as freely moving between the collisions with the velocity

$$v = \frac{\lambda}{\tau} \ .$$

The definition for the unmagnetized case can be applied and their velocity is the thermal velocity v_{th}, giving

$$D_\perp = v_{th}^2 \tau = \frac{v_{th}^2}{f} \ . \tag{2.31}$$

The diffusion is at its maximum if the collision frequency is equal to the gyration frequency [35]. With the definitions of $\omega_g = eB/m_e$ and $v_{th} = \sqrt{k_B T_e / m_e}$ this results in:

$$D_\perp = \frac{k_B T_e}{eB} \ . \tag{2.32}$$

This coefficient has the relation to $\cong 1/B$ as found in the experiments. Empirically a fraction 1/16 of this value has been found. The actual value is dependent on the plasma properties and can deviate by about a factor of 3. It should be noted, that while this coefficient reflects the diffusive behavior, it does not describe its origins. The cause of the diffusive behavior is mainly found to be in the ion oscillations. E.g. in a typical cylindrical plasma thruster the azimuthal component of the electric fields caused by these oscillations is always perpendicular to the magnetic field, which has only axial and radial components (assuming perfect cylinder symmetry of the permanent magnets). Therefore an $\boldsymbol{E} \times \boldsymbol{B}$ drift exist for the electrons which by definition causes the electrons to move perpendicular to $\boldsymbol{B}$. While it is actually a drift and not a diffusion, when an appropriate fraction (1/16 or similar) is used the coefficient can describe the additional electron mobility perpendicular to the magnetic field.

2.10 Ionisation prozesses

To generate and sustain a plasma discharge, neutral atoms must be ionized. In steady state, the 'production' of ions balances their losses. These losses are typically losses to the discharge chamber wall or for in-space application to outer space. In a plasma discharge typically at least three types of electron-neutral collisions occur: elastic, excitation and ionization. In the elastic case, the electron does not lose kinetic energy and only its direction of motion is changed. In the excitation case, one of the electrons of a neutral atom enters a (sometimes metastable) state of higher energy and the impacting electron loses energy equal to the excitation threshold. In the ionization case, one electron leaves the atom which consequently becomes an ion. The impacting electron loses energy equal to the ionization threshold, which is e.g. for xenon 12.1 eV. The exact manner how these processes are calculated in the PiC simulation will be described in chapter 3.

3 Methods for simulation of a HEMP thruster

3.1 Simulating a permanent magnetic field

A basic property of HEMP thrusters is the magnetic field generated by permanent magnets. The moving charges in the plasma are generating a magnetic field as well. For example, the micro-HEMPT primarily investigated in this work has an electron current of I = 4.5 mA towards the anode (at 400 V anode voltage, 0.27 sccm neutral gas flux). Under the strongly simplified assumption that electrons of uniform density move axially from the thrusters exit towards the anode, they generate an azimuthal field inside the discharge chamber of

$$B = \frac{\mu_0}{2\pi} \cdot \frac{I}{r} = \frac{\mu_0}{2\pi} \cdot \frac{J\pi r^2}{r} = \frac{J\mu_0}{2} \cdot r \quad . \tag{3.1}$$

J is the (here homogeneous) electron flux density, μ_0 is the magnetic permeability of vacuum. The magnetic flux density increases linearly with the radius r. Therefore, its maximum strength is at the discharge chambers radius, $r =$ 1,5 mm where it is B $= 6 \cdot 10^{-7}$ T. Since the current value of the ion beam leaving the thruster is similar to the electron anode current, the magnetic field generated by the ions must be of similar strength as well. The field generated by the permanent magnets is in the order of 0.1 T. This draws the conclusion, that the field created by the plasma currents is negligible. Since the permanent magnets field does not change over time it only needs to be calculated once ahead of the plasma simulation and can be used as a constant input parameter. The source of the magnetic field is the magnetization $M(r)$ which is a material constant of the magnets. It is applied to the regions of the simulation domain which represent the magnets via $B(r) = \mu_0 M(r)$. The divergence of the field exterior to the magnets is defined according to the Gauss law of magnetism: $\nabla B(r) = 0$. First, the magnetic vector potential $A(r)$ is calculated. The local magnetic flux density $B(r)$ can then be derived from it due to $B(r) = \nabla \times A(r)$ (Fig. 3.1). The simulation uses the finite element method. The simulation domain is typically significantly larger than that of the PiC simulation since the domain boundary conditions strongly interfere with the solution. An adaptive mesh can be used where the elements become larger with increasing distance from the magnets. Due to the triangular shape and varying size of the elements, the result needs to be interpolated to the uniform grid of the PiC simulation.

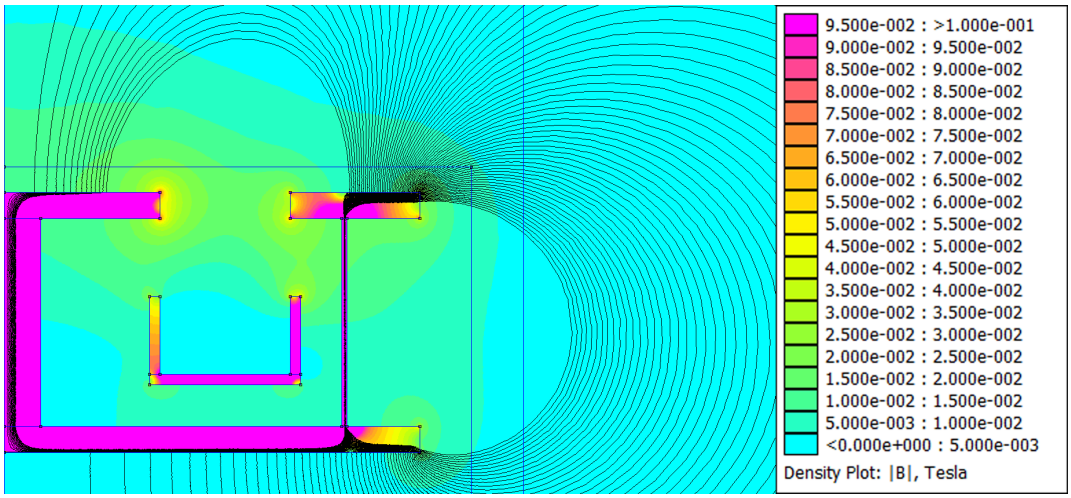

Figure 3.1: An example for simulated magnetic flux density (SPT-100-like Hall thruster with permanent magnets).

3.2 Description of the thrusters neutral gas flow by particle model

While in a static (closed) discharge tube plasma and neutral gas are in equilibrium for a plasma thruster the latter constantly needs to be replenished. Consequently, for a computer model of a plasma thruster it is essential to simulate the neutral gas flow and distribution. The neutral gas is injected through one or more inlets into the thrusters discharge chamber. In case of the HEMP thrusters these are located close to or at the anode. The gas atoms collide with each other at a rate

$$f_{nn} = v_{rel} \cdot n_n \cdot \sigma_{nn} \ .$$

Where v_{rel} is the particles velocity relative to each other before the collision, n_n is the particles density, and $\sigma_{nn} = \pi d^2$ is the effective area within the atoms collision do occur; called the collision cross-section. In this case, where the colliding atoms are of the same kind, d is twice the van der Waals radius of the atom species [36]. The average distance a particle moves without a collision (the particle velocities being Maxwell distributed) is called the mean free path λ_{mfp} [37]:

$$\lambda_{mfp} = \frac{v_{rel}}{\sqrt{2} f_{nn}} = \frac{1}{\sqrt{2} n_n \sigma_{nn}} \ .$$

In case that the expected gas density (typical values $1 \cdot 10^{19}$ - $1 \cdot 10^{22}$ particles per cubic meter) is such that the particles mean free path is significantly lower

than the discharge chamber dimensions, the neutral gas is collision-dominated. Under this condition a fluid approach can be taken for the neutral gas simulation. In this approach the neutral gas is treated as a continuum described by the Euler equation [38],

$$\frac{\partial v_n}{\partial t} = v \cdot \nabla v + \frac{1}{n_n} \nabla p_n \ ,$$

with v_n and p_n being velocity and pressure, at time t. It can be expanded to the Navier-Stokes equation by introducing the viscosity (resistance to gradual deformation by shear stress or tensile stress). A simulation grid is applied again and since these partial differential equations only need to be solved for the grid cells and not for every single particle, the calculation is less time-consuming.

However, with increasing distance to the thrusters exit the density constantly decreases and one quickly leaves the regime where the gas is collision-dominated. Therefore, in the region near the thrusters exit the fluid approach becomes invalid and the particles need to be traced individually. In order to have a valid model for the entire area of the simulation a particle model is applied. Nevertheless, the collisions between the particles cannot always be neglected, considering the maximum density near the anode. For this reason a Monte Carlo code [39] is used. With the addition of collisions of particles at the thruster walls this method gives an accurate description of the particles movement.

Simulating each single atom obviously exceeds any computational capacity. Therefore, like in the PiC simulation which is used for the plasma particles, the neutrals are summarized to super-particles. E.g. thousand neutral atoms are combined to one super-particle with thousand times the mass and collisions cross-section area [40].
Consequently, the particle density is decreased as the cross section is increased and, therefore, the mean free path is retained. Since the mass increase is applied equally to all particles the relative impulse exchange and therefore the collision behavior is also not altered. In consequence, the system that consists of super-particles behaves similarly to a real system consisting of atoms. Obviously, this method needs to be taken with care so that the super-particle density does not become too coarse.

Like in a PiC simulation, a computational grid is applied for the simulation domain. Only particles within the same grid cell are checked for collisions. For this method to be valid, the step size of the time-resolution must be chosen in a manner that a particle cannot cross more than one cell per time step (For a Maxwell distribution, a tiny fraction can have extreme velocities. Therefore it

is deemed acceptable for a low percentage of particles to violate this condition).

This method vastly saves computational time while keeping the error low, under the condition that there are many particles per cell [41]. For the boundary conditions diffuse reflections on the thrusters wall showed the best agreement with the experimental results.

3.3 The Particle-in-Cell simulation method

3.3.1 Overview

The behavior of the charged particles in a plasma device is calculated by splitting the simulation time into many time steps of duration Δt. Then the total simulated time is $T = N_T \Delta t$ with N_T being the number of time steps. The particles positions and velocities have to be advanced at each time step (Fig. 3.2). On the macroscopic scale the interactions of large numbers of particles by electric and magnetic fields ($\boldsymbol{E}$ and $\boldsymbol{B}$) are calculated. Movements caused by microscopic fields like Coulomb collisions are calculated by another part of the PiC routine, which in general uses a Monte Carlo code. The force on a single particle with the charge q_p and velocity $\boldsymbol{v_p}$ caused by the fields at its position x_p, $\boldsymbol{E_p}$ and $\boldsymbol{B_p}$, is the Lorentz force:

$$\boldsymbol{F_p} = q_p(\boldsymbol{E_p} + \boldsymbol{v_p} \times \boldsymbol{B_p}) \ . \tag{3.2}$$

Integration of the equation of motion provides the new particles velocities and positions. For their final positions and velocities at the next time step additional effects need to be taken into account. The basis of each PiC simulation in Cartesian space is a rectangular or cubic domain in 2D or 3D, respectively. Within this domain the particles can move. To simulate a plasma device like a thruster it is necessary to account for particle sinks and sources including the plasma generation. For example, a wall of the device can be simulated as a sink for electrons and ions and a source for neutrals (to emulate neutralization of the ions). The plasma generation is accounted for by considering the ionizing events inside the volume occupied by the plasma particles. These are electron-neutral ionizing collisions. For a realistic plasma behavior, the model should at least take into account the elastic, excitation and ionizing electron-neutral collisions.

The fields are calculated on the grid that spans the simulation domain. The field sources on the grid are determined by assigning the charges of the particles and the electric currents (due to the movement of charged particles) to the grid points.

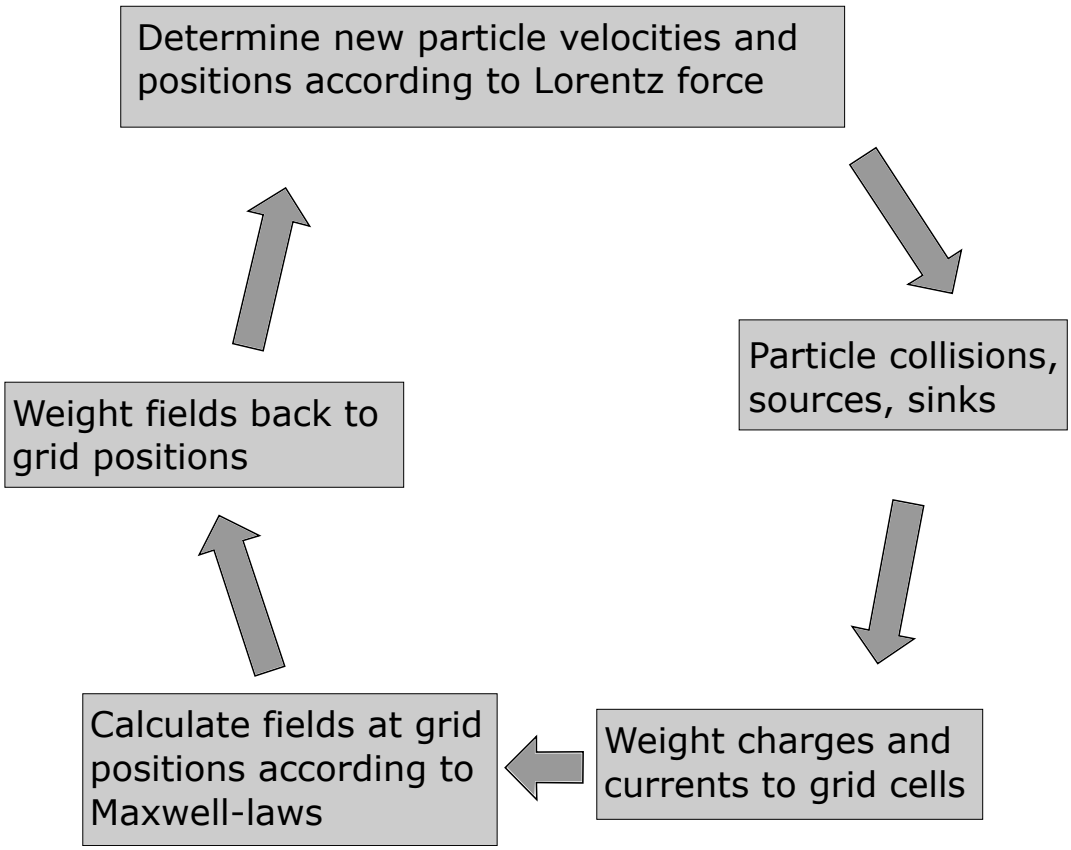

Figure 3.2: The particle-in-cell cycle.

It has already been shown that the magnetic field generated by the current is negligible for the thrusters investigated here (chapter 3.1). Therefore, only the positions of the charges need to be taken into account.

The calculation of the fields is done using the Maxwell formulas:

$$\nabla \cdot \boldsymbol{E} = \frac{\rho}{\epsilon_0} \tag{3.3}$$

$$-\frac{\partial \boldsymbol{B}}{\partial t} = \nabla \times \boldsymbol{E} \tag{3.4}$$

$$\nabla \cdot \boldsymbol{B} = 0 \tag{3.5}$$

$$\nabla \times \boldsymbol{B} = \mu_0 \left(J + \epsilon_0 \frac{\partial \boldsymbol{E}}{\partial t} \right) \tag{3.6}$$

Since the magnetic field which is induced by the plasma current density J is negligible, and the permanent magnets field is static (hence $\frac{\partial \boldsymbol{B}}{\partial t} = 0$), in principle only $\nabla \cdot \boldsymbol{E} = \rho/\epsilon_0$ remains ($\nabla \cdot \boldsymbol{B} = 0$ is used in the static magnetic field simulation performed in advance of the plasma simulation, see chapter 3.1). The weighting of the particle charges at the grid points provides a spatial charge distribution $\rho(r)$ over the grid. The field is obtained by calculating the potential using the Poisson equation and, then, deriving the potential to aquire the field. For the calculation of the potential boundary conditions must be taken into account. For example the domain boundaries or areas of fixed potential, which stand in for metallic parts of the plasma device.

Finally, the field values at the grid points need to be weighted back to each particle position using the same weighting function. Then the particle pusher (chapter 3.3.2) can be applied again which is the beginning of the new cycle.

3.3.2 Particle pusher

The part of the code which is responsible for the particle movement is usually called the particle pusher. In most cases, the available memory and computation time is by far exceeded if a calculation would be performed for each physical particle of a plasma device. Therefore, an integral part of the PiC concept is the use of so-called super-particles [35]. These have a mass and charge in orders of magnitude higher than the physical particles. Hence, their overall number can be accordingly lower. As given by the formula which describes the Lorentz force (eq. 3.2), when the charge/mass ratio is kept constant the acceleration of the particle and, thus, its trajectories remains unchanged. The most straightforward approach to calculate the velocity of the particle v_p and position x_p at each step Δt is by

$$v(t + \Delta t)_p = v(t)_p + \Delta v_p \ ,$$

and the position with

$$x(t + \Delta t)_p = x(t)_p + v(t)_p \Delta t \ .$$

The velocity change Δv_p, which occurs within one time step Δt, is caused by the Lorentz force F_p acting on the particle ($\Delta v_p/\Delta t = F_p/m_p$). Such a direct calculation, however, has the largest inherent numerical errors. Therefore, the more common approach is the so-called leap-frog method. Here the velocities are calculated halfway between the time steps as shown in Fig. 3.3 and the acceleration is defined as:

$$a(t)_p = \frac{\Delta v(t)_p}{\Delta t} = \frac{v(t + \frac{1}{2}\Delta t)_p - v(t - \frac{1}{2}\Delta t)_p}{\Delta t} \ .$$

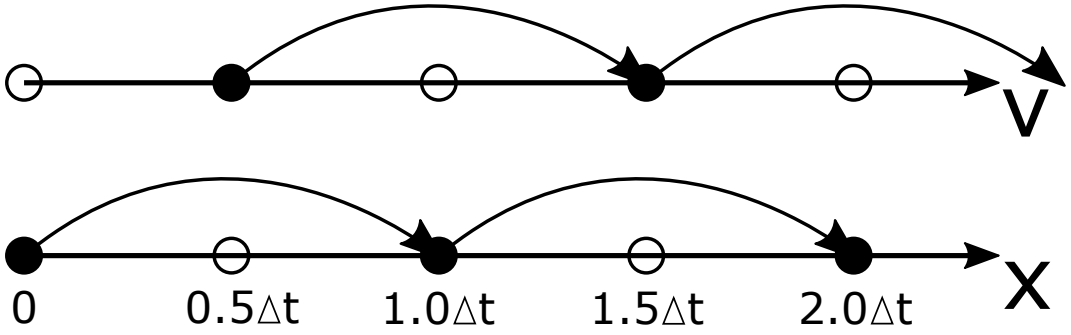

Figure 3.3: Leapfrog schema for advancing particles positions and velocities.

The positions are calculated at the time steps. The velocity is defined as:

$$v(t+\frac{1}{2}\Delta t)_p = \frac{\Delta x(t)_p}{\Delta t} = \frac{x(t+\Delta t)_p - x(t)_p}{\Delta t} \ .$$

The new velocities and positions are, thus, directly calculated as:

$$v(t+\frac{1}{2}\Delta t)_p = v(t-\frac{1}{2}\Delta t)_p + a(t)_p \Delta t$$

and

$$x(t+\Delta t)_p = x(t)_p + v(t+\frac{1}{2}\Delta t)_p \Delta t \ . \tag{3.7}$$

The short-scale interactions of charged particles (collisions) are treated by the Monte Carlo code. The Lorentz force (eq. 3.2) is applied in the context of the large-scale electric and magnetic fields. For its application in the pusher the fields E_p and B_p at the position x_p of the particle are acquired by weighting from the fields $E_{i,j}$ and $B_{i,j}$ at the four nearest grid points (in the case of a 2D grid). A weighting function described in chapter 3.3.3 is used. However, direct application of this force to the previously described advancement of particles leads to significant systematic numerical errors (Fig. 3.4). Therefore, the common method is the Boris pusher [42]. It takes into consideration that the influence of a magnetic field will always cause gyration motion, while an electric field causes linear acceleration. Therefore, the motion is separated into the first half of a linear acceleration (due to $\boldsymbol{E}$), followed by a rotation (due to $\boldsymbol{B}$), and then the second half of the linear acceleration.

The intermediate values for these steps are labeled t_1 and t_2, their actual value is of no concern (t_1 and t_2 actually have the same value, the rotation is treated as instantaneous). According to the leap frog schema, the first intermediate step for determining the new velocity starts at $(t - \frac{1}{2}\Delta t)$:

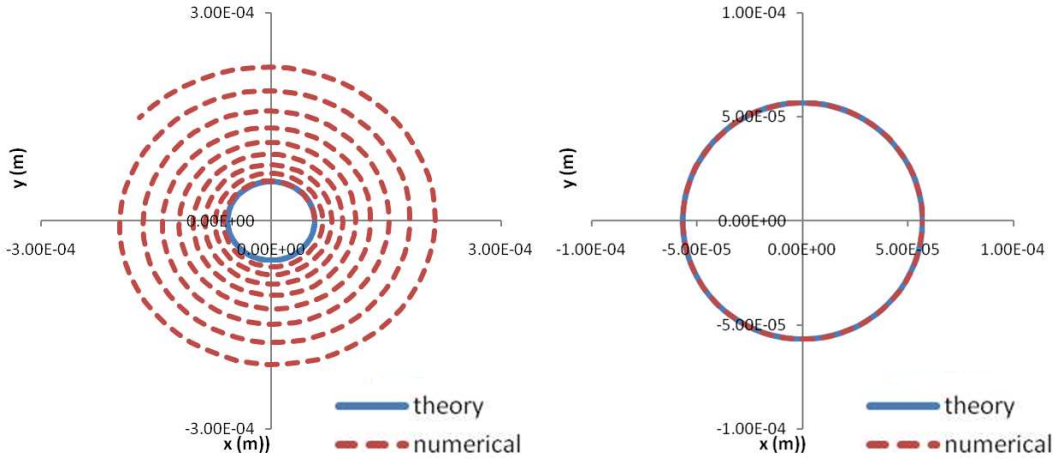

Figure 3.4: Numerical particle movement with direct application of leapfrog schema (left), and leapfrog with Boris pusher (right). *Source: [43].*

$$v(t_1)_p^0 = v(t - \frac{1}{2}\Delta t)_p^0 + \frac{q}{m}E(t)_p^0\frac{1}{2}\Delta t \ ,$$

$$v(t_1)_p^1 = v(t - \frac{1}{2}\Delta t)_p^1 + \frac{q}{m}E(t)_p^1\frac{1}{2}\Delta t \ ,$$

where the upper indices 0 and 1 stand for the two spatial directions of a 2D case. Next step is the rotation:

$$v(t_2)_p^0 = cos(\omega_g\Delta t)v(t_1)_p^0 + sin(\omega_g\Delta t)v(t_1)_p^1 \ ,$$

$$v(t_2)_p^1 = -sin(\omega_g\Delta t)v(t_1)_p^0 + cos(\omega_g\Delta t)v(t_1)_p^1 \ ,$$

where ω_g is the gyration frequency, which can be directly calculated from the particles properties and the magnetic flux density. The velocity at $(t + \frac{1}{2}\Delta t)$ is reached by the second half of the linear acceleration:

$$v(t + \frac{1}{2}\Delta t)_p^0 = v(t_2)_p^0 + \frac{q}{m}E(t)_p^0\frac{1}{2}\Delta t \ ,$$

$$v(t + \frac{1}{2}\Delta t)_p^1 = v(t_2)_p^1 + \frac{q}{m}E(t)_p^1\frac{1}{2}\Delta t \ .$$

The next position $x(t+\Delta t)_p^0$, $x(t+\Delta t)_p^1$ is calculated as in equation (3.7). For neutral particles, the Lorentz force does not apply. Velocity changes occur only

due to collisions with walls as described in chapter 3.3.5. The calculation of their movement also follows the leap frog schema. Additional velocity changes due to collisions on a microscopic scale are also calculated by a Monte Carlo code, as described in chapter 3.3.6.

3.3.3 Grid weighting

As mentioned before, the movement due to the Boris pusher is driven by the relatively large scale electric and magnetic fields. Since the magnetic field is a static input parameter only the electric field needs to be calculated at each time step. The minimum scale on which this field is calculated is the grid cell size. This size again is determined by resolving the Debye length and, hence, usually equal to one or half of this characteristic plasma length. The grid is used for calculation on the macroscopic level (collective behavior) where individual particles are not accounted for. Therefore, the grid structure is appropriate to calculate this collective behavior. For the electric field to be calculated, the electric charge of the particles needs to be assigned to the grid points as shown in Fig. 3.5. This method saves calculation time since on average there are several particles per grid cell, and, thus per grid point. Also it is simpler to calculate fields for a uniform grid than for randomly distributed particles. Furthermore, since this calculation is on macroscopic scale the position of each individual particle is not of interest. The simplest method is the assignment of the complete charge of each particle to each's nearest grid point (NGP). In a 2D case (e.g. a 2D cylindrical simulation domain) the grid points are defined as $x_{i,j}$ with the indices i and j standing for the two spatial directions. The corresponding positions given in real units can be derived by $i\Delta x$ and $j\Delta y$. The sum of the charges q_p that are assigned to the corresponding grid point is applied with the same indices:

$$q_{i,j} = \sum_{p=1}^{N_p} (q_p W(x_p, x_{i,j})) \ .$$

This sum is over all particles of the system, N_p. Here the weighting function $W(x_p, x_{i,j})$ is just a simple if-condition, that determines which grid point is the closest to the particle with the position x_p

$$\begin{aligned} W(x_p, x_{i,j}) &= 1 \ if \ x_{i,j} - x_p < 0.5\Delta x \\ &= 0 \ else \end{aligned} \quad .$$

Then, the charge density at each grid point can be directly calculated as:

$$\rho_{i,j} = \frac{q_{i,j}}{\Delta V}$$

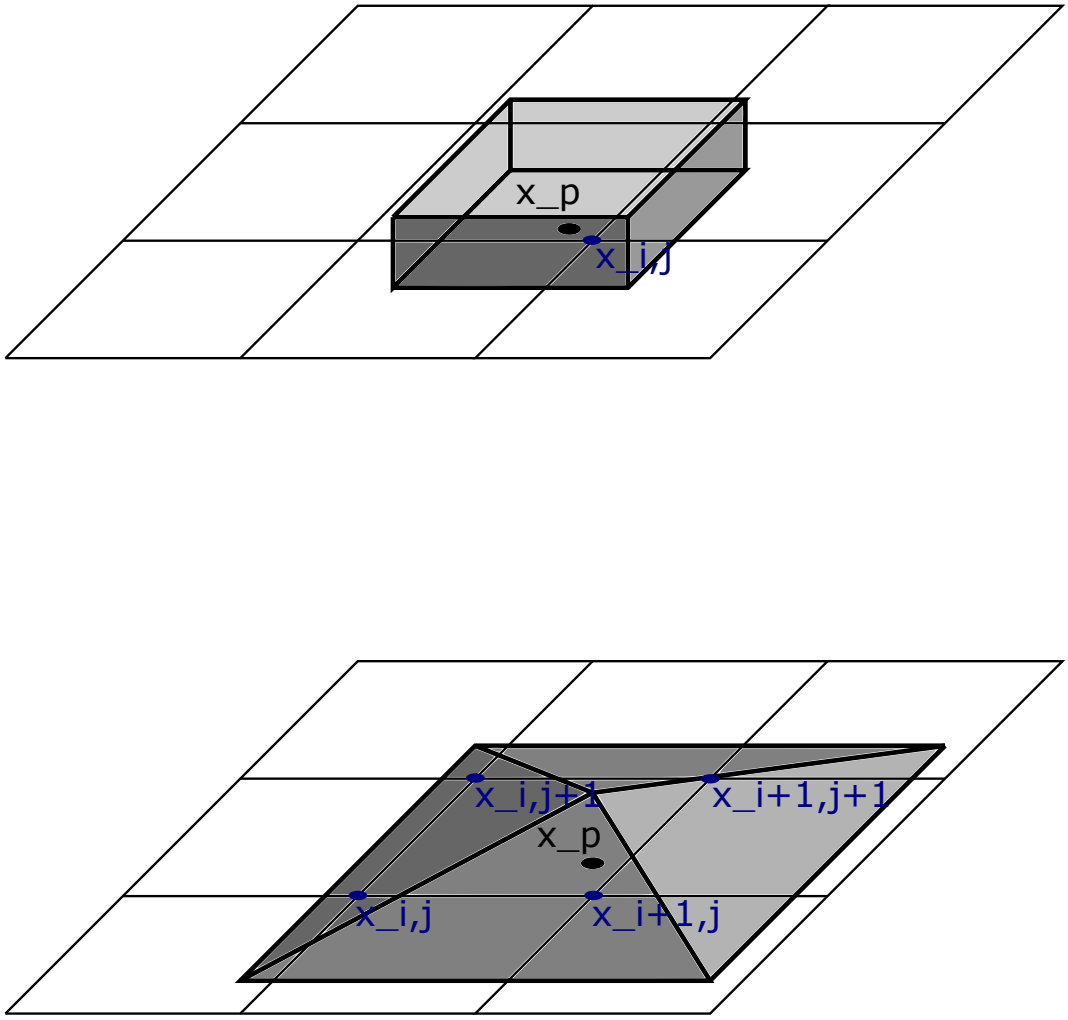

Figure 3.5: Particle-in-cell weighting schemas: Nearest grid point (NGP) and cloud in cell (CIC); upper and lower picture respectively.

with the cell area $\Delta V = \Delta x \Delta y$ (or volume $\Delta V = \Delta x \Delta y \Delta z$ in 3D case). With this weighting function the particles appear to the grid as rectangular shapes of half-length $0.5\Delta x$ whose densities rise and fall to zero again like a step-wise function. While simplest in the calculation for each particle, this method creates a large amount of undesired numeric noise that must be compensated by more particles per cell. Therefore, the advantage in calculation speed usually does not pay off compared to more sophisticated weighting methods. The most commonly used method is the so-called cloud in cell method [44]. Here, the weighing decreases linearly over one grid cell length in both spatial directions (2D case).

$$W(x_p, x_{i,j}) = \left(1 - \frac{\left|x^0_{i,j} - x^0_p\right|}{\Delta x}\right)\left(1 - \frac{\left|x^1_{i,j} - x^1_p\right|}{\Delta x}\right) \; if \;\; |x_{i,j} - x_p| < \Delta x$$
$$= 0 \qquad\qquad else$$

The upper indices 0 and 1 indicate the two components of the vector $x_{i,j}$, which points to a grid point position. In both spatial directions the charge is distributed depending on the distance to the two nearest grid points. In consequence, the charge is spread over the four nearest grid points, such that charge conservation $\sum_{i,j=1}^{N_x,N_x} W(x_p, x_{i,j}) = 1$ [45] and isotropy in space $W(x_p, x_{i,j}) = W(-x_p, x_{i,j})$ is achieved. The charge conservation is obviously necessary to avoid non-physical effects, while the latter is needed to avoid self-forces [46]. On the grid, the effective area of the particles is also of a rectangular shape, yet of side length $2\Delta x$. They behave more like diffuse clouds in regards of the weighting. If such a cloud moves through the grid its charge is assigned much more smoothly than with the NGP method. Consequently, there is much less noise in the electric fields on the grid and acceptable results can be achieved with much less particles. Since the four nearest grid points, to whose a particle is always assigned too, always span up a cell this is the namesake of the Particle-in-Cell method.

3.3.4 Solving on the grid

Within a two-dimensional domain the charge densities $\rho_{i,j}$ at the grid points $x_{i,j}$ are used to determine the electric potential $\Phi_{i,j}$. i and j are the position indices on a two-dimensional grid. For simplicity, first, a one-dimensional case is shown in Fig. 3.6, then instead of $\rho_{i,j}$ we have just ρ_i. As for any charge density distribution the problem can be solved by the Poisson equation:

$$-\frac{\partial \Phi(x)}{\partial x^2} = \frac{1}{\epsilon_0}\rho(x) \; .$$

The needed second order derivation can be approximated by a three-point finite difference schema [47]:

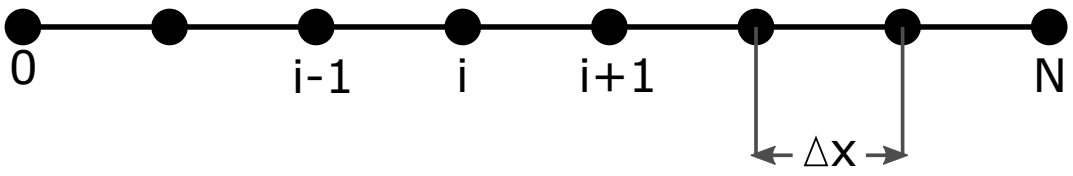

Figure 3.6: Indices on a 1D grid.

$$\frac{\partial \Phi}{\partial x^2} = \frac{\Phi_{i-1} - 2\Phi_i + \Phi_{i+1}}{\Delta x^2} \ . \tag{3.8}$$

Boundary conditions, e.g. the potential at both ends of the one dimensional grid being set to zero, can be directly applied: $\Phi_0 = 0$, $\Phi_N = 0$. By substituting $\rho_i' = -\frac{\Delta x^2}{\epsilon_0}\rho_i$ over all indices it provides an assembly of Poisson equations:

$$\begin{aligned}
\Phi_0 - 2\Phi_1 + \Phi_2 &= \rho_1' \\
&\dots \\
\Phi_{i-1} - 2\Phi_i + \Phi_{i+1} &= \rho_i' \\
&\dots \\
\Phi_{N-2} - 2\Phi_{N-1} + \Phi_N &= \rho_{N-1}' \ ,
\end{aligned}$$

with N being the number of grid points. With the mentioned boundary conditions there are as many equations as unknown quantities (the Φ's). Therefore, the problem is solvable [48] and it can be brought into matrix form,

$$\begin{pmatrix} -2 & 1 & 0 & 0 & 0 \\ & \dots & & & \\ & 1 & -2 & 1 & \\ & & & \dots & \\ 0 & 0 & 0 & 1 & -2 \end{pmatrix} \begin{pmatrix} \Phi_1 \\ \dots \\ \Phi_i \\ \dots \\ \Phi_{N-1} \end{pmatrix} = \begin{pmatrix} \rho_1' - \Phi_0 \\ \dots \\ \rho_i' \\ \dots \\ \rho_{N-1}' - \Phi_N \end{pmatrix}$$

and in short:

$$\boldsymbol{A\Phi} = \boldsymbol{\rho'} \ . \tag{3.9}$$

The form of the matrix $\boldsymbol{A}$ is independent of the current time step and it can be decomposed into an upper $\boldsymbol{U}$ and a lower $\boldsymbol{L}$ triangular matrix:

$$\boldsymbol{A} = \boldsymbol{LU} \ . \tag{3.10}$$

This procedure needs only to be done once ahead of the simulation run. Then, it can be solved recursively for a given $\boldsymbol{\rho'}$ at any time step [49]. This method saves significant computational time. Once the transformation from a differential equation to a matrix equation is performed, it is in a form that can be solved by several libraries which are available [50]. The most common c-code Library is super-LU, which is also used here. The electric field at each grid point is calculated according to Gauss's law:

$$E(x) = -\frac{\partial \Phi(x)}{\partial x} \ ,$$

which is in form of the finite difference schema:

$$E_i = \frac{\Phi_{i-1} - \Phi_{i+1}}{2\Delta x} \ . \tag{3.11}$$

In case of a 2D grid with square shaped cells ($\Delta x = \Delta y$), which is used in the following simulations, the discretization of the second derivative of Φ is needed for two dimensions:

$$\Delta\Phi = \frac{2\partial\Phi}{\partial x^2} + \frac{2\partial\Phi}{\partial y^2} = \frac{\Phi_{i,j-1} + \Phi_{i-1,j} - 4\Phi_{i,j} + \Phi_{i+1,j} + \Phi_{i,j+1}}{\Delta x^2} \ ,$$

with i, j again being the indices related to the two spatial directions. The Poisson equation is now accordingly:

$$-\frac{\Phi_{i,j-1} + \Phi_{i-1,j} - 4\Phi_{i,j} + \Phi_{i+1,j} + \Phi_{i,j+1}}{\Delta x^2} = \frac{1}{\epsilon_0}\rho_{i,j} \ . \tag{3.12}$$

The procedure is the same as for 1D: setting up the linear equation system, bringing it into matrix form and obtaining the solution is done in the same schema. However, in the 2D case boundary conditions can be more complicated since entire areas of cells can be set to a fixed potential, e.g. to represent the anode or grounded metallic parts. Nevertheless, since all points at the outer rim have a fixed potential, there will always be at least as many equations as unknown quantities. Hence, the problem remains solvable. While in the 1D case the electric field was a scalar, in the 2D case it is, of course, a two-component vector and is again obtained by the central difference schema:

$$E_{i,j} = \frac{\Phi_{i-1,j} - \Phi_{i+1,j}}{2\Delta x} e_x + \frac{\Phi_{i,j-1} - \Phi_{i,j+1}}{2\Delta y} e_y \ . \tag{3.13}$$

The $\boldsymbol{E}$-fields are weighted back to the particle positions according to chapter 3.3.3 and feed into the Boris pusher for the next cycle. If dielectric materials are used a dielectric permittivity value $\epsilon_{i,j}$ must be assigned to each cell. This value must then be implemented in the discretization of the Poisson equation. Dielectric materials are not grounded due to their almost zero conductivity, and, therefore surface charge accumulation must be taken into consideration. This is done by counting the absorbed charged particles and assign an according charge density $\rho_{i,j}$ to each of the cells that represent the surface of the dielectric part.

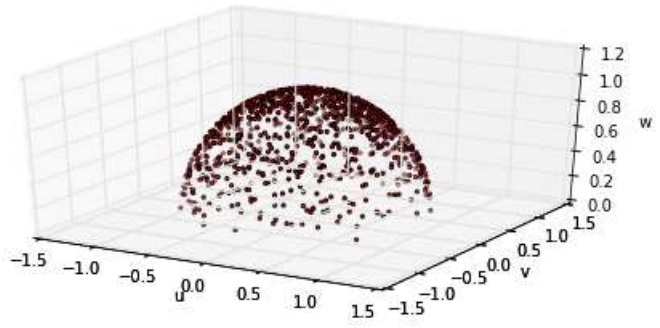

Figure 3.7: Diffusive reflected particles positions in Cartesian coordinates u,v,w. Used for neutral particle reflection and secondary electron emission. *Source: [43].*

3.3.5 Particle sinks and sources

For each PiC cycle it needs to be checked whether particles need to be removed or if and where particles should be added. Unless the domain is periodic in any direction, particles which left the grid have to be deleted from the domain immediately. Some parts of a plasma device can be seen as absorbing for certain particle species, e.g. metallic parts for electrons. The cells that represent the area occupied by such a part need to be defined as absorbing for this species.

Secondary emission is accounted for the electrons impacting on the surfaces of the thruster channel (emission due to impacting ions is considered negligible due to their low energy). A simplified model is applied where 50 % of the electrons are injected back with 90 % of the kinetic energy of the incident electron [51]. The directions of the secondary electrons velocity vectors are randomly to form a uniform distribution over the solid angle, excluding directions that would lead back into the surface (Fig. 3.7).

In general, each ion 'absorbed' at a surface is 'replaced' by a neutral atom imitating the neutralization process. If the absorbing surface is dielectric the accumulated charge of the absorbed electrons and ions needs to be feed into the according $\rho_{i,j}$ of the electric potential solver (chapter 3.3.4).

For neutral particles a solid surface can be seen as reflective. E. g. if a neutral particle has crossed a surface with a normal vector e_w, its v_w component is inverted while its v_u, v_v components remain. For rough surfaces, it can be more realistic if diffuse reflection is applied [52]. There v_u and v_v are set to random values, resulting in a uniform distribution of velocity vectors that form a hemisphere above the surface (Fig. 3.7).

Two of the most common particle sources in plasma thrusters are the neutral

gas inlet and the neutralizer (electron source). Their particle fluxes are usually given by the experimental setup. These flow values (e.g. I) can be calculated to physical particles per second and, then, for the simulation in super-particles per second (with the physical- to super-particles ration N_{SP}), and finally as super-particles per time step $NMPPS$ [53]:

$$NMPPS = \frac{I\Delta t}{eN_{SP}} \quad .$$

The $NMPPS$-value can be directly applied in the code. It is also possible to have the code written such that the flow values from the experiments are used and the calculation to $NMPPS$ is done by the code. For the particle positions the simplest form is a uniform random distribution over a pre-defined area, e.g. with the boundaries X_{min}, X_{max}, Y_{min}, Y_{max} :

$$x = RAND(X_{max} - X_{min}) + X_{min} \quad ,$$

$$y = RAND(Y_{max} - Y_{min}) + Y_{min} \quad ,$$

with $RAND$ being a random number in the range $[0, 1]$. Also, for spatial depending particle densities sampling functions can be obtained. For the initial velocity, a Maxwellian distribution often yields sufficient results. Here, usually the Box-Muller method [54] is applied since inverse sampling is needed, which is not possible with the direct application of the Maxwell function:

$$v = \sqrt{-2 \cdot log(RAND)} \quad .$$

To speed up the discharge ignition, often an initial load of ions and electrons is set in the area where significant plasma density is expected. The Maxwellian distributions are set according to the expected average ion and electron energies.

3.3.6 Particle collisions

As mentioned in the chapters before besides the Lorentz force based on the macroscopic field and the sinks and sources, the additional effect on the particles positions and velocities are the collisions. If all particles in the simulation would be checked for collisions with each other, N particles would result in almost N^2 checks.
One can see that for high particle numbers this would quickly reach an undesirable amount of calculation. Fortunately, since the default requirements for PiC simulations include that particles do not cross more than one cell per time step, it is sufficient to check for collisions only within each cell once a time step [55]. The direct simulation Monte Carlo (DSMC) method then checks for

each cell all species within this cell for possible collisions, e.g. electron-neutral collisions. If a collision does occur, particle attribute changes are performed, depending on the type of collision.

In PiC, a common application of DSMC are elastic Coulomb collisions between the electrons. This type of collision is applied by rotating the velocity vectors of both colliding particles, whereby energy and momentum are preserved.

The Fokker-Planck equation [56] can be approximated by describing the elastic scatter angle ψ with a Gaussian function, where an azimuthal angle ζ can be set randomly in the range $[0, 2\pi]$. This effect can be sampled by a Monte Carlo code, too. A rotation matrix $A(\psi, \zeta)$ can be used to calculate the new velocity direction vectors.

This procedure still takes a significant amount of computation, since all particle trajectories within each cell must be checked. If one of the species is orders of magnitude heavier and denser, it is much simpler to implement Monte Carlo collisions (MCC). For each cell, the check loops around only for e.g. all the electrons within it and treats the heavier species, e. g. neutral particles, as a target 'cloud' [57]. For the latter, a particle density n_n is calculated based on the number of particles in each cell.

For electron-neutral collisions an energy dependent cross section σ_{ne} is used. This can be found for all sorts of neutral species and all kinds of collisions from tables based on experimental data [58]. The collision probability P is then [59]

$$P = 1 - exp(-n_n v \sigma_{ne} \Delta t) \ .$$

Here Δt is the time span between the checks for collisions and v the incident velocity. The shortest timespan that should be set is the pusher time span of the electrons movement. Depending on the average collision frequency longer time spans can be chosen. The decision whether a collision actually occurs is then made by use of a random number T; element of $[0; 1]$. The collision is only executed if $T < P$.

3.4 Setting up realistic and stable starting conditions

Since individual particles are traced, a PiC simulation is a self-consistent system if the input is given by boundary conditions and sources. The boundary conditions for the electrostatic calculation are a set of potentials that usually represent metallic parts of the device that are grounded or have fixed potential to operate the discharge. For the particles, the boundary conditions are

generally absorbing surfaces, defined as sinks (e.g. for charged particles), reflective surfaces (e.g. for neutrals), or surface charge accumulation (e.g. for charged particles at dielectric surface). The most common sources are set for electrons and neutrals, the former representing the neutralizer and the latter the gas inlet. These regions are pre-defined volumes in which new particles are generated with a certain velocity distribution, usually Maxwell distribution. Since it cannot be calculated for inverse sampling, the Box Muller method [54] is used which yields Maxwell distributed velocities for the particles. For the positioning of the new particles an inverted Monte Carlo sampling method is used [60]. Here, the spatial distribution function is inverted and uniform random numbers are used for the sampling process. If an experiment has to be reproduced by the computer model the source strengths are usually given as currents and mass flows. For the simulation, these values must be calculated for the macro particles per time step which are then injected by the source.

Usually, the steady state properties of a plasma device are investigated and hence this state must be reached. Steady state means that the overall number of ions and electrons does not change anymore with time (if there are fluctuations that are caused by a periodic energy source, these can be ignored). Given proper starting conditions, the plasma ignites from a neutral gas, and steady state will be reached.

In a real device, the plasma ignition is often accelerated or only possible by a burst of intensified neutral gas mass flow for a short duration. This short time, however, is usually in the timescale of the PiC simulations too long to be calculated in a feasible manner.

Therefore, one usually starts using neutral gas distribution pre-calculated for the mass flow used if the thruster is already running.

The most realistic initial condition would be a very low percentage of charged particles in a neutral gas (e.g. concentration of positive ions under normal fair weather is 250 to 1500 ions per cm^3 [61]), representing the condition in which this gas naturally occurs.

However, by this assumption most of the calculation would be spent with a very low number of charged particles, while this number increases over a very long time (on the timescale of the PiC-simulation) until steady state is reached.

Therefore, it is common to start with a reasonable assumption for the plasma density in steady state, so that it is merely the distribution of the particles that changes. In best case, even the spatial allocation of the plasma can be approximated with the initialization, either by assumptions or if it is known due to experiments.

By that way, a significant amount of the simulation time can be cut without affecting the final result. Alternatively, relatively strong additional electron sources can be added. But they must be terminated timely before steady state and, thus, before the final result is reached.

The plasma density is often rather non-uniform, and it has to be ensured that the resulting Debye length λ_D does not become lower than the grid cell size ΔX. Otherwise numerical instabilities can arise. Obviously, the initial plasma density n_e must be selected such that this condition,

$$\Delta X < \lambda_D \ , \tag{3.14}$$

is not violated. Otherwise, the simulation would become unstable immediately following its initialization. This can be directly achieved since the initial n_e is a value set by the user and usually there is no need for this value to be set higher than the maximum of the final plasma distribution.

The bigger challenge is to ensure that the maximum density n_e never exceeds a value which causes λ_D (being inverse proportional to n_e) to become smaller than ΔX. Otherwise, the simulation also becomes numerical unstable and might never reach steady state. This is particularly the case if the maximum plasma density is not known by experiments. As a simple example, if a one-dimensional domain of size L_x is set, the grid cell size ΔX can be adjusted by selecting a value for the number of grid cells N_x:

$$\Delta X = \frac{L_x}{N_x} \ . \tag{3.15}$$

This obviously works accordingly for the second and third dimension as well.

Being overcautious, a small ΔX can be set which might result in the grid being higher resolved than necessary. Then the resulting high cell number causes additional computation time. On the other hand, starting with a ΔX which is too large to resolve the final maximum plasma density makes it necessary to start the simulation all over again with a higher grid resolution, also consuming additional time.

The electron plasma frequency ω_{Pe} must be resolved, since these are the fastest fluctuations of the plasma:

$$dt < \frac{1}{\omega_{Pe}} \ . \tag{3.16}$$

If a magnetic field is applied, the electron cyclotron motion with the gyration frequency ω_g must also be resolved, with several steps per gyration:

$$dt < \frac{1}{0.2\omega_g} \ . \tag{3.17}$$

Also, it must be ensured that a super-particle cannot cross more than one cell within the duration of one time step. The fastest particles are again the electrons with their maximum possible velocity $v_{e,max}$ being close to the velocity gained by the potential drop of the anode potential V_d:

$$v_{e,max} = \sqrt{\frac{2eV_d}{m_e}} \ . \tag{3.18}$$

Then, the time step criteria is:

$$dt < \frac{\Delta X}{v_{e,max}} \ . \tag{3.19}$$

Due to this restriction for the velocity, for each time step it is sufficient to calculate the Coulomb collisions only between the electrons within each cell. The neutral particles movement is calculated on a larger timescale with longer time steps, but the same kind of restriction for their velocity is applied. Consequently, their collisions also need only to be calculated between the neutrals within each cell.

Depending on the parameters of the simulation, the length of the time step is either determined by electron plasma frequency, gyration frequency or maximum velocity, whichever is the smallest.

Another basic criterion is that the number of particles within a Debye's sphere, N_D, must be:

$$N_D >> 1 \ . \tag{3.20}$$

For real particles, this is commonly the case since this is one of the plasma criteria (chapter 2.2). With the use of super-particles, however, it has to be checked if this criterion is still fulfilled.

3.5 PiC simulation in cylindrical coordinates

PiC simulations in all three dimensions are computationally expensive. Therefore, it is preferred to simplify the problem into a two-dimensional case. Assuming as a basic example a cubic domain, the number of cells increases with the third power of the number of cells per length. In 2D, it increases only with the second power, so an amount of cells equal to their number per length is saved. Considering that each cell should have several macro particles, it becomes evident that the computational time is significantly reduced.

Many plasma devices are cylindrical and this is especially the case for plasma thrusters. A cylindrical coordinate system consists of axial, radial, and tangential components called z, r, and φ, respectively. Under the condition of cylindrical symmetry of the plasma device, φ can be set to an arbitrary value, and the problem is then solved in a two-dimensional domain which lies in the r-z-plane.

However, special care needs to be taken when working with a non-Cartesian coordinate system. The particles that appear in the r-z-plane are spread out over all possible φ's from 0 till 2π. By segmentation of the r-distance for example into the selected cell length dr one can define hollow cylinders whose volume increase proportionally to r:

$$V_{cylseg} = L(\pi(ndr)^2 - \pi((n-1)dr)^2) = L\pi dr^2 2(n+1/2)\ . \tag{3.21}$$

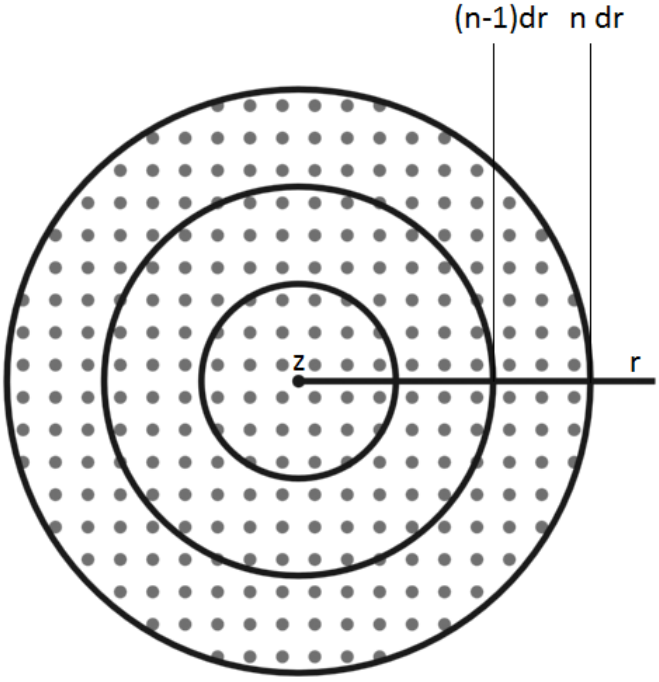

Figure 3.8: *Density of particles in a cylinder volume on r-z-plane.*

L is the length of the domain and n is a running natural number, the maximum is the number of grid cells in r-direction. In the case of a uniform particle density, the number of particles occupying each hollow cylinder consequently also increases proportionally to r (Fig. 3.8). As a result, the density of particles per area in the r-z-plane increases proportionally to r. When calculating the density for analyzing the PiC simulation results, it has to be taken into

account that this increase does not represent an actual increase in particles per volume. This will also be considered in the following chapter. It is also important for the weighting of the particle charges on the grid since the particle density directly results in charge density. For the potential calculation on the grid, the cylinder symmetry is taken into account in the Poisson equation and its discretization, which is given in ref [62] as:

$$\frac{1}{\epsilon_0}\rho = \frac{1}{2dr^2}\Phi_{i,j-1} - \frac{1}{2}\left(\frac{1}{dr^2} - \frac{1}{2rdr}\right)\Phi_{i-1,j} + \frac{1}{4}\left(\frac{4}{dr^2} + \frac{1}{rdr}\right)\Phi_{i,j}$$

$$-\frac{1}{2}\left(\frac{1}{dr^2} - \frac{1}{2rdr}\right)\Phi_{i+1,j} - \frac{1}{2dr^2}\Phi_{i,j+1} \tag{3.22}$$

The effect of cylinder coordinates becomes obvious when particles are inserted in the r-z-plane with initial velocities in radial and axial direction, v_r and v_z, but not in azimuthal direction (v_φ). Mostly, they seem to move like in a plane in the Cartesian system (e.g. an x-y-plane). But there is one exception: Once a particle has reached the z-axis, it appears to be reflected. The particles r-distance obviously decreases, reaches zero at the z-axis and increases again. At the time of crossing its azimuthal value instantaneously changes by the factor of π. The azimuthal values are not visible in the r-z-plane, only the decrease and increase of the r-value is visible, which then appears as a reflection. In fact, the particle moves in a straight line through Cartesian space. When a particle also has an initial azimuthal velocity, it can pass the z-axis at a certain radial distance which in the r-z-plane can be regarded as a smoothed version of the apparent reflection.
Even if they are initialized with $v_\varphi = 0$ (and arbitrary v_r and v_z) particles can get a v_φ component through collisions with other particles, due to the three dimensional nature of the Monte Carlo codes calculation.
A magnetic field with an r- or z-component, or both, also causes a motion into azimuthal direction due to Lorentz force.
Due to these effects, in a PiC cycle the integration of motion must take the azimuthal velocity into account, even though after each time step the azimuthal position is treated as arbitrary again.

3.6 Analyzing the resulting dataset

The result of a PiC simulation is merely an assembly of particles, their phase space and their final electric potential. Since there are typically millions of super-particles in a single simulation, plotting them does not give a useful picture. Proper analysis and interpretation of the data needs to be done.

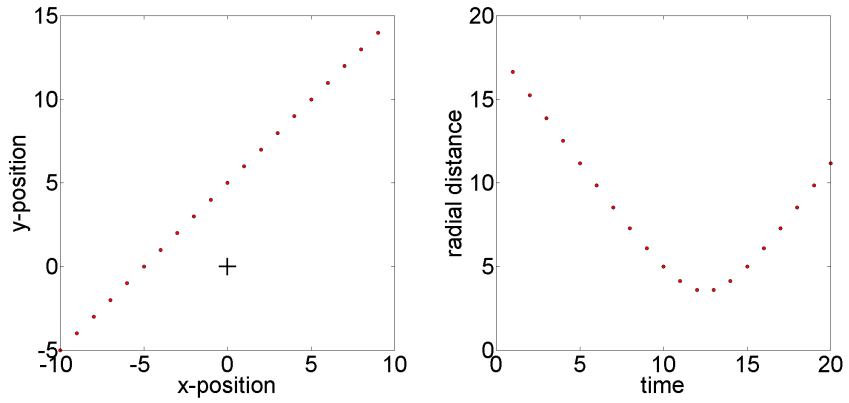

(a) (b)

Figure 3.9: a) Trace of a particle passing the z-axis (black cross) in Cartesian coordinates. b) Radial distance of the particle (distance to z-axis) over time (arbitrary units).

The electric potential, however, is directly available from the PiC-cylce. It is calculated in each time step for the grid points labeled with the indices i,j. Therefore, the potential can be stored at any selected time step. For plotting, the positions only have to be calculated to physical units using the grid cell size: $i \cdot dr$, $j \cdot dr$.
A basic property that can be calculated from a particle assembly is their density. A typical approach is to calculate average values per cell. Therefore, the volume that each cell represents in 3 dimensional space, V_{cell}, is calculated as described in the previous chapter, to account for the cylindrical geometry. For each cell, the number of containing particles is counted and with the indices i,j labeled accordingly as $N_{p,i,j}$, with p indicating the particle species. The particle density can then directly be calculated as,

$$n_{p,i,j} = \frac{N_{p,i,j} N_{sp}}{V_{cell,i,j}} \ , \tag{3.23}$$

where it had to be multiplied with N_{sp} in order to get the value for the physical particles.
The same principle can be applied for the collision rate,

$$n_{coll,i,j} = \frac{N_{coll,i,j} N_{sp}}{V_{cell,i,j} dt} \ . \tag{3.24}$$

Here it has to be divided by the time step length dt to obtain the density of collisions per second.

Also, the average kinetic energy per cell can be calculated for each particle species. First, for each particle of a species in a selected cell its kinetic energy is calculated from its velocity components and its mass: $E_{kin_p} = (m_p/2)(v_z^2 + v_r^2 + v_\varphi^2)$. The azimuthal velocity must be given in m/s, like for the other two components, not in degrees/s. The mean kinetic energy can be calculated for each cell:

$$E_{kinmean,p,i,j} = \sum \frac{E_{kin_p}}{N_{p,i,j}} \ . \tag{3.25}$$

Here, $N_{p,i,j}$ is again the number of particles of a certain species in a cell.

It is also useful to count for each species the overall number of particles at each time step, or at the end of periods of pre-defined length (e.g. every 1000 time steps). This method creates a history during the run which helps to check whether steady state has been reached. Also, periodic oscillations might be found by that way unless the step size of the history is too large or the numerical noise is too strong.

Knowledge of the fluxes to the absorbing surfaces is often of interest. For example, for the anode it is defined that the electrons are removed from the simulation if their postion z_e, r_e has reached the condition: $z_e < 0$, $r_e < R_A$, with R_A being the radius of a cylindrical anode. If the number of electrons removed under this condition at each time step is counted as $N_{e,A}$, the electric current can be calculated as:

$$I_e, A = \frac{Q}{t} = \frac{eN_{e,A,real}}{t} = \frac{eN_{e,A}N_{sp}}{dt} \ . \tag{3.26}$$

4 A self-similarity scaling scheme containing characteristic quantities

4.1 Case of unbound plasma

When a purely kinematic approach is made for a plasma simulation, the movement of electrons and ions being on different timescales provides a challenge regarding calculation time. Due to their lower mass, the electrons are at least three orders of magnitude faster than the ions. While the motion of the ions can be calculated in larger time steps, it is unavoidable to resolve the movement of the electrons on their timescale. This leads to a very high number of time steps before the system reached steady state since the evolution time of the system is determined by the ions (If neutrals are assumed as a static background, otherwise neutral gas has the slowest evolution). Due to that fact, the desired computational time is often exceeded.
One method to bring the computational time into a reasonable regime was developed by Taccogna at al. [63]. This method will be described in detail in this chapter. The basic concept consists of reducing the system size with the aim of faster computation, while the physics of the simulated plasma discharge are retained.

The starting point of this method is to scale the system size L_S^* down with a factor ζ which affects all lengths L_x^*, L_y^*, L_z^* (in a three-dimensional system). It has to be determined which parameters are affected by this and how they scale. The parameter L_S, (without an asterisk), stands for the new system size of the downscaled system. All unscaled parameters are marked by an asterisk. As a premise, it is determined that the velocity of the particle v will not be altered by the scaling. This assumption will be validated later (chapter 4.3, eq. 4.48).
Before investigating the case of a specific thruster, the scaling law should be validated for the most basic case, which is an infinite, uniform plasma volume. We imagine a cube inside this plasma, whereas the boundaries of the cube are purely mathematical (Fig. 4.1). The particles can pass freely through them [64]. In a uniform plasma volume the velocity distribution is isotropic.
The side length L_S of the cube is completely arbitrary and serves only as a

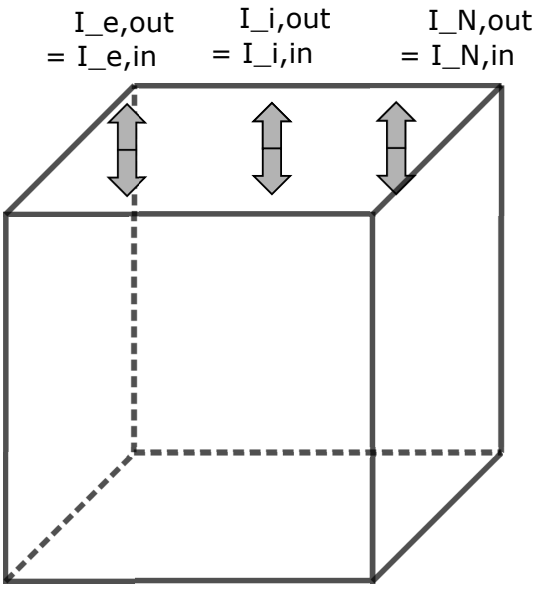

Figure 4.1: *In- and outflows of a mathematical cube inside an infinite plasma.*

reference to the scaling factor ζ. It is representative of the system size, while it should be kept in mind that a system can be more arbitrary shaped. The volume V of the cube is obviously L_S^3.

When the system is downscaled, the particle trajectories need to be scaled down by the same factor for the system to show the same properties. The trajectories of the charged particles are influenced by the Lorentz force due to electric and magnetic fields on a macroscopic scale and collisions on a microscopic scale. The latter are short-scale electric interactions, e.g. Coulomb collisions between electrons. For neutral particles, the trajectories are only influenced by collisions. Since the particle velocities remain the same the particle collisions are obviously unaffected by the scaling as long as the system size is not scaled into the microscopic regime. The plasma properties are strongly determined by the ionization process. In impact ionization driven thrusters like of the Hall and HEMPT type, collisions for other than electron-neutral type are negligible compared to those, as shown in [63]. The electron-neutral collisions are distinguished between elastic, excitation and ionization collisions. The collision cross-sections σ depend on the involved species (electrons, neutrals) and the kinetic energy of the colliding particles. Since v is defined as constant for this scaling schema, this energy does not change and, therefore, σ_{en} does remain the same in the scaled system. Each collision changes the electron trajectory, while the much heavier atoms remain relatively unimpeded. For the trajectory scaling in equal proportion with the system size, the ratio between the mean free path of the collisions, λ_{en}, and the system size L_S must remain constant [65]. This ratio is also called the Knudsen number Kn [66]:

$$Kn = \frac{\lambda_{en}}{L_S} \ . \tag{4.1}$$

λ_{en} is inversely proportional to the neutral gas density n_n:

$$\lambda_{en} = \frac{1}{\sigma_{en} n_n} \ . \tag{4.2}$$

The Knudsen number is the same when λ_{en} scales as the system size:

$$Kn = \frac{1}{\sigma_{en} n_n} \frac{1}{L_S} = \frac{\zeta}{\sigma_{en} n_n^*} \frac{1}{\zeta L_S^*} \ . \tag{4.3}$$

Therefore, the neutral gas density must scale as:

$$n_n = \frac{n_n^*}{\zeta} \ . \tag{4.4}$$

As shown by this relation, the neutral gas density must increase by the inverse of the scaling factor when the system is scaled down.
If the properties of the plasma discharge should remain unchanged, the ratio of charged particle density n_c to neutral particle density must be constant:

$$\frac{n_c}{n_n} = \frac{n_c^*}{n_n^*} = const. \ . \tag{4.5}$$

From this relation it follows that n_c must change with $1/\zeta$ as well:

$$n_c = \frac{n_c^*}{\zeta} \ . \tag{4.6}$$

Due to the quasi-neutrality of the plasma we can approximate the electron and ion densities, n_e and n_i, to be equal (assumption of only single charged ions), then we have:

$$n_e = n_i = \frac{1}{2} n_c \ . \tag{4.7}$$

Consequently:

$$n_e = \frac{n_e^*}{\zeta} \tag{4.8}$$

and

$$n_i = \frac{n_i^*}{\zeta} \ . \tag{4.9}$$

Hence, it can be generalized:

$$n = \frac{n^*}{\zeta} \ . \tag{4.10}$$

In a uniform plasma there are no macroscopic electric fields present. Therefore, only the magnetic part of the Lorenz force is effective. As discussed earlier, the velocity component of a particle parallel to a magnetic field line is not directly affected by the field strength. The velocity component of a particle that is perpendicular to the local field forms a gyration motion with the radius.

$$r^* = \frac{m_e v}{eB^*} \ . \tag{4.11}$$

Therefore for this radius to be scaled down along with the system size L_S, B must be scaled up with the scaling factor

$$B = \frac{B^*}{\zeta} \ . \tag{4.12}$$

Then, the particles trajectory is scaled down with the system size.
For an infinite plasma, which is investigated here, there are no wall losses. Therefore, the only losses of charged particles can be through recombination of electrons and ions (Of course in the actual thruster there will be wall losses, and recombination will be negligible relative to the wall losses. This will be considered in the next chapter).
For the plasma to remain in steady state, the losses need to be counteracted by an ionization process.
As an energy source for this process a spatial uniform energy input is assumed, since for infinite plasma in large scales everything should be uniform. It could be for example, a standing wave microwave field, yet the kind of source is arbitrary for this consideration.
The ionization process acts as a volume source that generates an equal amount of electrons and ions per time.
The density of ionization events per time is described by the differential form of the general continuity equation:

$$\frac{\partial n_e}{\partial t} + \nabla \cdot J = Q_{ionize} \ . \tag{4.13}$$

In an infinite, uniform plasma the net particle flux J is zero. The density n_e is the number of electrons dN_e per volume element dV. Q_{ionize} is the generation of N_e per volume per time. Therefore, it scales proportionally with the number of electrons multiplied by the collision frequency f_{en} at which an individual electron undergoes ionizing collisions with neutral atoms. If n_e and n_n are spatially uniform, the overall number of electrons generated within the cube can be derived by multiplying with its volume V:

$$S_{ionize} = VQ_{ionize} = V\frac{dN_e}{dV}f_{en} = Vn_e f_{en} = \zeta^3 V^* \frac{n_e^*}{\zeta}\frac{f_{en}^*}{\zeta} \propto \zeta \ . \tag{4.14}$$

Here, the scaling of the electron collision frequency f_{en} was used. It derives from the electron mean velocity being divided by their mean free path and the initial condition $v = v^*$

$$f_{en} = \frac{v}{\lambda_{en}} \propto \frac{1}{\zeta} \ . \tag{4.15}$$

λ_{en} is expressly the mean free path of ionizing collisions. As the other collisions it scales with $\propto \zeta$.
dn_e/dt would then be the change in electron density if there were no losses. Losses and ionization being equal in the steady state means for the recombination rate:

$$S_{recomb} \propto \zeta \tag{4.16}$$

The particles transit time T_{tr} is a reference for the time T until the system reaches steady state (usually T about a multiple times T_{tr}) and, therefore, they scale equally. Due to the premise of v being constant the transit time scales as $T_{tr} = L_S/v = \zeta L_S^*/v \cong \zeta$. L_S is the side length of a cube in particular or the system size in general.
The time step size dt needs to resolve the fastest plasma dynamic which is the electron plasma oscillation [67]. As shown, for the system to be self-similar, the plasma density must increase with the scaling: $n_e = n_e^*/\zeta$. The electron plasma oscillation frequency ω_{pe} has a dependence with n_e as [68]:

$$\omega_{pe} = \sqrt{\frac{n_e e^2}{m_e \epsilon_0}} \propto \sqrt{n_e} \ . \tag{4.17}$$

Therefore, number of time steps necessary to resolve one transit, N_{steps} (and consequently their reduction), is related to the scaling as:

$$N_{steps} = \frac{T_{tr}}{dt} \propto T_{tr}\omega_{pe} \propto \sqrt{\zeta} \ . \tag{4.18}$$

Since in general a few of this transit times are necessary to reach steady state, this translates directly to an equivalent reduction of time steps until steady state is reached.
Table 4.1 gives the summary of scaling equations.

Table 4.1: The scaling quantities of infinite plasma

Quantities	scaling
Velocity	$v = v^*$
Magnetic field	$B = \zeta^{-1} B^*$
Particle density	$n = \zeta^{-1} n^*$
Ionization	$S_{ionize} = \zeta S^*_{ionize}$
Recombination	$S_{recomb} = \zeta S^*_{recomb}$

4.2 Wall losses

In order to work properly for a plasma device like a thruster, the scaling law obviously needs to remain valid if plasma-wall interactions appear. As a basic example, now the cube investigated in the previous chapter shall enclose a finite plasma volume. As for most common plasma device materials like metal or ceramics, the walls can be assumed impenetrable for neutral noble gas atoms (diffusion through the walls is insignificant on the timescale of the plasma dynamics). In an enclosed plasma device where the plasma conditions have reached steady state the neutral gas density remains constant for a given volume. A prominent example are commercial glow discharge tubes which keep their low pressure constant for years, only altered by leakage and chemical reactions over long periods of time. The ionization causes no loss of neutral gas to the overall system, since this is compensated by ions being neutralized when they reach the walls. In any case, the neutral gas scaling condition (eq. 4.4) must remain the same, since it is only determined by keeping the constant ratio of system size and electron-neutral collisions mean free path.
In order to scale the charged particle trajectories properly, the scaling condition for the magnetic field (eq. 4.12) must be applied if such a field is present.
For the infinite plasma described in the previous chapter losses for charged particles were only possible by recombination. But in an enclosed device there are also wall losses. For the density and temperature range of the plasma investigated here, the losses due to recombination are negligible compared to the wall losses. The walls can be treated as being totally absorbing for charged particles (for simplicity ignoring secondary electron and ion emission). Hence, the wall losses can be described as an outflow. This outflow is defined by a volume V_{cross} with particles of particle density n_c that crosses the walls surface A with a mean velocity of v within a time t. The volume V_{cross} results from

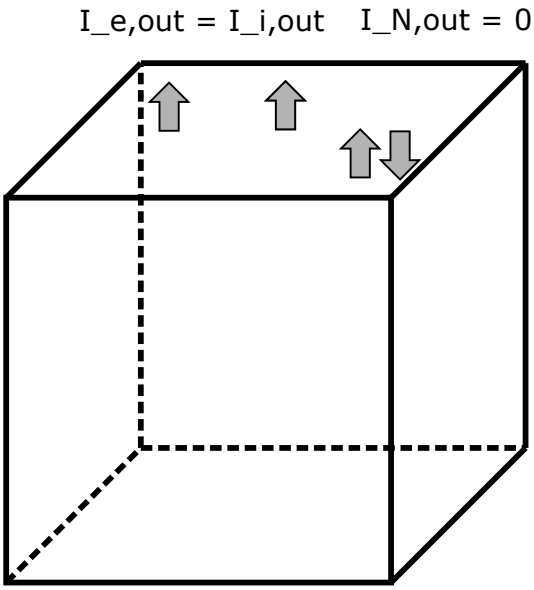

Figure 4.2: *In- and outflows of a cube enclosing a plasma.*

the surface A and the distance c traveled by the particles perpendicular to this surface: $c = vt$. The surface area scales with ζ^2, and as mentioned earlier, if the plasma properties are to remain the same the charged particles density must scale as $n_c^* = n_c/\zeta$. Therefore, this outflow loss described in particles per time (N_c/t), scales as:

$$I_{C,out} = \frac{N_c}{t} = \frac{n_c V_{cross}}{t} = \frac{n_c A v t}{t} = n_c A v = \frac{n_c^*}{\zeta}\zeta^2 A^* v \propto \zeta \ . \tag{4.19}$$

To compensate these losses and, thereby, keep the balance at the density n_c, the ionization source strength must also scale with ζ,

$$S_{ionize} \propto \zeta \ , \tag{4.20}$$

which is the same scaling condition discussed in chapter 4.1, eq. 4.14.
Due to quasi-neutrality the densities of electrons and ions are equal and, therefore, from the scaling of the charged particles density n_c concludes again:

$$n_e = n_e^*/\zeta \tag{4.21}$$

and

$$n_i = n_i^*/\zeta \ . \tag{4.22}$$

The conclusion is that all particle densities scale in the same manner:

$$n = n^*/\zeta \ . \tag{4.23}$$

Due to the wall losses now the continuity equation includes a net flux J_e, while in steady state dn_e/dt becomes zero:

$$\nabla \cdot J_e = Q_{ionize} \ . \tag{4.24}$$

Here Q_{ionize} is now the local source strength like in the previous chapter determined by the electron density and collision frequency. The electron current $I_{e,out}$ of a volume V can be calculated by bringing the continuity equation into integral form:

$$I_{e,out} = eS_{ionize}$$

$$= e\int_0^L\int_0^L\int_0^L \nabla J_e dV = e\int_0^L\int_0^L\int_0^L Q_{ionize} dV = e\int_0^L\int_0^L\int_0^L n_e f_{en} dV$$

The integration is performed over a volume that is fully enclosed by a surface, in this case a cube. For simplicity in this model n_e is assumed to be spatially constant:

$$I_{e,out} = en_e f_{en}\int_0^L\int_0^L\int_0^L dV = e\frac{n_e^*}{\zeta}\frac{f_{en}^*}{\zeta}\int_0^{\zeta L^*}\int_0^{\zeta L^*}\int_0^{\zeta L^*} dV^*$$

$$I_{e,out} = e\frac{n_e^*}{\zeta}\frac{f_{en}^*}{\zeta}\zeta L^*\zeta L^*\zeta L^*$$

Therefore, the relation is:

$$I_{e,out} \propto \zeta \tag{4.25}$$

Since the ionization produces an equal amount of electrons and ions, the ion current towards the walls $I_{i,out}$ is also:

$$I_{i,out} \propto \zeta \ . \tag{4.26}$$

Furthermore, since the wall losses of charged particles are by each half electrons and ions, we have for the current of charged particles towards the walls $I_{C,out}$:

$$I_{e,out} = I_{i,out} = \frac{1}{2} I_{C,out} \propto \zeta \ . \tag{4.27}$$

Finally, we come to the same scaling dependence as calculated directly from the density, thus, validating the scaling law for the conditions of wall losses.

Table 4.2: The scaling quantities of a bounded plasma.

Quantities	scaling
Velocity	$v = v^*$
Magnetic field	$B = \zeta^{-1} B^*$
Particle density	$n = \zeta^{-1} n^*$
Ionization	$S_{ionize} = \zeta S^*_{ionize}$
Wall current	$I_{C,out} = \zeta I^*_{C,out}$

As summarized in table 4.2, the relation for the velocity, magnetic field, particle density, and ionization remain the same as for the unbound plasma. The recombination becomes negligible while a scaling definition for the wall current has been added.

4.3 Schematic thruster model

Obviously, a thruster is not entirely a closed device; it has an outlet that ejects the ions which generate the thrust.
The geometric shape of the thruster model is a cylinder of length L_{cyl} with a radius R and accordingly a cross section A_c. At one end (cross section area) is the electron outflow $I_{e,A}$ while the opposing side is the electron inflow $I_{e,source}$ (Fig. 4.3).
Electrons originating from a neutralizer entering through the open end are defined as the inflow. The closed end is the electron outflow. Usually, at the closed end is the anode which attracts the electrons with its positive potential. The same potential accelerates the ions in the opposing direction.
For simplicity (until further notice), it shall be assumed that a spatial and temporal constant axial magnetic field permits electron losses to the cylinder walls. The diffusion of electrons perpendicular to magnetic field lines will be described later.
A simple approximation for the wall losses can be implemented, since, as will be shown, $I_{e,A}$ scales in the same manner as the wall losses $I_{C,out}$ from the enclosed plasma device discussed in the previous chapter.
The magnetic field definition of this model also serves as the simplest approximation of the HEMP thruster since its magnetic field topology is dominated by the axial B-component (which is perpendicular to the anode).

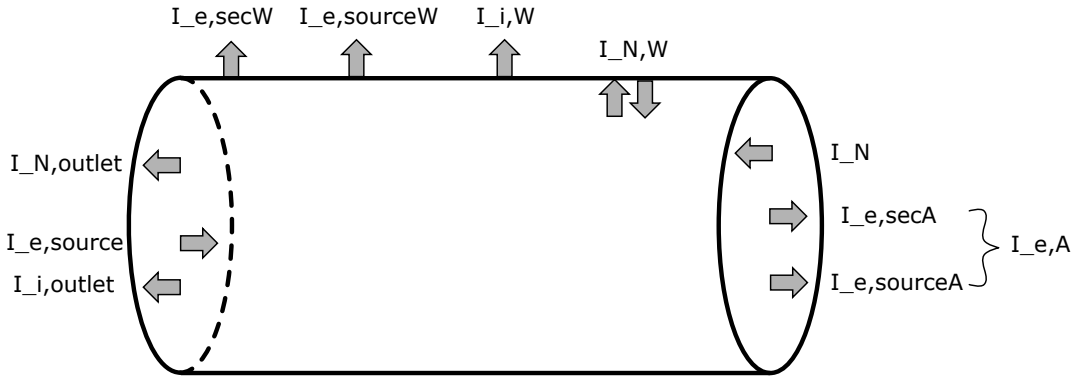

Figure 4.3: *In- and outflows of a cylindrical plasma thruster.*

The electrons travel on helixes along the magnetic field lines (chapter 2.3) from the inflow surface to the outflow surface.
The sizes of the radii of the helixes need to sustain their ratio to the dimensions of the cylinder. Therefore, again the scaling condition for the magnetic field as described in chapter 4.1, eq. 4.12 must be applied.
To scale the density of the ionization rate in the same manner as in the enclosed plasma device, both the density of the source electrons $n_{e,source}$ and the density of the background neutrals n_n need to be scaled with $1/\zeta$, as described in the previous chapter.
In an enclosed device like a discharge tube the neutral gas particle density can be directly set via the overall amount of neutral gas. In a thruster, however, it can only be indirectly applied by reaching a balance between particle inflow I_n and outflow $I_{n,out}$. Since there are no losses to the cylinder walls (neutrals cannot penetrate the ceramic and are reflected), the source strength resulting in the correct neutral density n_n can be calculated by the volume dV occupied by neutrals which are inserted at the base during a certain time dt. The cylinders base A_c is the channels cross section and the volume is this area multiplied with the distance dz they have traveled with mean axial velocity v_n:

$$\frac{dm}{dt} = MI_n = M\frac{dN_n}{dt} = Mn_nA_cv_n$$

$$= M\frac{n_n^*}{\zeta}\zeta^2 A_c^* v_n^* \propto \zeta \ . \tag{4.28}$$

Like for all other velocities it is $v_n = v_n^*$. M is the atom mass of the neutral species.
Without wall losses, the scaling for the electron source to keep the correct density can be calculated by the same formula, regarding these electrons traveling with the mean velocity $v_{e,z}$ in the opposite direction as the neutrals:

$$I_{e,sourceA} = I_{e,source}$$

$$= e\frac{dN_{e,source}}{dt} = en_{e,source}A_c v_{e,z} = e\frac{n^*_{e,source}}{\zeta}\zeta^2 A^*_c v^*_{e,z} \propto \zeta \ . \tag{4.29}$$

Now introducing wall losses (see previous chapter) for the charged particles into the model its scaling can be estimated by assuming that the source electrons migrate with an arbitrary velocity $v_{e,Sw}$ towards the cylinder walls. Their surface is $A_w = 2\pi RL_{cyl}$ and the current can be calculated with the density $n_{e,source}$ and the volume that electrons have occupied after traveling perpendicular to that area over a distance dr. Selecting an infinitesimal short timespan for dt the dependence of the surface and density from the radial distance can be neglected:

$$I_{e,sourceW} = \frac{dN_{e,sourceW}}{dt} = \frac{en_{e,source}v_{e,Sw}dt2\pi RL_{cyl}}{dt}$$

$$= en_{e,source}v_{e,Sw}2\pi RL_{cyl} = e\frac{n^*_{e,source}}{\zeta}v_{e,Sw}dt2\pi\zeta R^*\zeta L^*_{cyl} \propto \zeta \ . \tag{4.30}$$

So, as previously assumed, the current to the walls follows the same scaling as the other currents. The only difference is that the losses have partially shifted from the thrusters outlet towards the walls.
Therefore, the scaling of the source electron losses remains unchanged by the introduction of wall losses.
Consequently, the scaling of the source electron density stays as $n_{e,source} \propto 1/\zeta$.
The ionizations source strength can be calculated directly, as described in the second chapter, based on the source electron density and the ionizing collision frequency of a singular source electron:

$$\nabla \cdot J_e = n_{e,source}f_{en} \ . \tag{4.31}$$

Like in the previous chapter it can be solved by integration, but this time in cylinder coordinates. The result is the overall current strength of electrons generated by ionization:

$$S_{ionize} = \int_0^R \int_0^{2\pi} \int_0^L \nabla \cdot J_e r dr d\varphi dz = \int_0^R \int_0^{2\pi} \int_0^L n_{e,source} f_{en} r dr d\varphi dz$$

$$= \int_0^{\zeta R^*} \int_0^{2\pi} \int_0^{\zeta L^*} \frac{n^*_{e,source}}{\zeta} \frac{f^*_{en}}{\zeta} r dr d\varphi dz$$

$$= \zeta^2 R^{*2} 2\pi \zeta L^* \frac{n^*_{e,source}}{\zeta} \frac{f^*_{en}}{\zeta} \propto \zeta \ . \tag{4.32}$$

As expected, this procedure yields the same scaling as in the previous two chapters.
This calculation assumed spatial constant densities, and consequently should only be considered valid under these conditions. Yet, as shown in the first chapter, the proper scaling for neutral gas and magnetic field yields the same particle trajectories relative to the system size. Therefore, it can be assumed that the relative density distribution remains the same.
This can be also shown by discretization of the cylindrical volume into elements of a three-dimensional Cartesian grid labeled with indices i,j,k, see Fig. 4.4. Then, the ionization source strength of each element can be directly calculated as:

$$S_{ionize,i,j,k} = \int_{x_{i-1/2,j,k}}^{x_{i+1/2,j,k}} \int_{y_{i,j-1/2,k}}^{y_{i,j+1/2,k}} \int_{z_{i,j,k-1/2}}^{z_{i,j,k+1/2}} n_{e,source,i,j,k} f_{en,i,j,k} dV \tag{4.33}$$

The local collision frequency $f_{en,i,j,k}$ is dependent on the local neutral gas density $n_{N,i,j,k}$, and the local ionization source strength obviously still scales as

$$S_{ionize,i,j,k} \propto \zeta \ , \tag{4.34}$$

preserving the self-similarity of the system.
Deviations due to change in the relation of Debye length (and consequently plasma sheath) to the system size will be investigated later (chapter 5.4).
With the common scaling of the electron source density $n_{e,source}$, the neutral gas density n_n and the ionization rate S_{ionize}, it can be concluded that the secondary electron density $n_{e,sec}$ scales with $\propto 1/\zeta$ as well.
The overall electron density is the sum of source and secondary electron density:

$$n_e = n_{e,source} + n_{e,sec} \ . \tag{4.35}$$

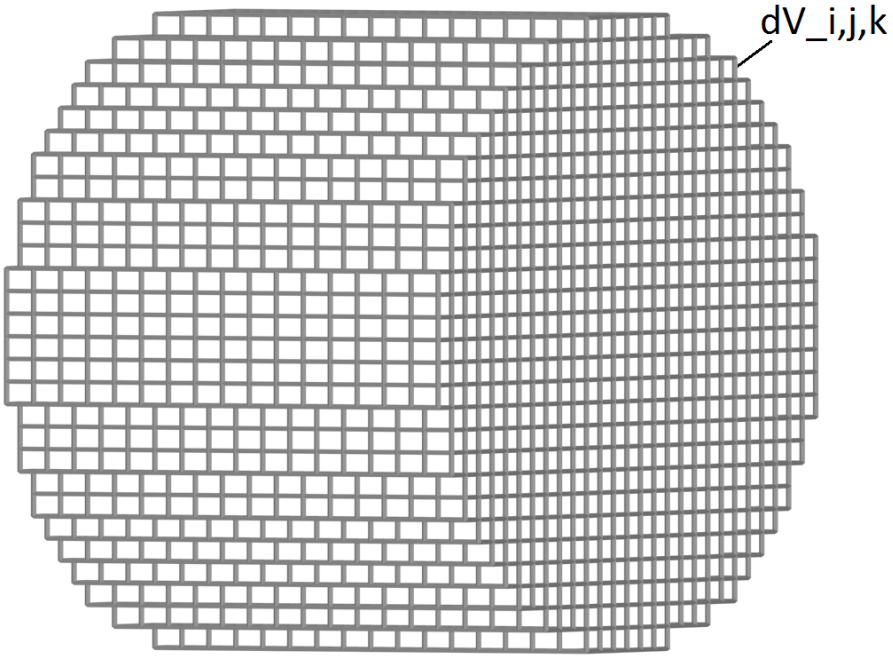

Figure 4.4: *A cylindrical volume approximated by cubic blocks.*

Since both scale with $1/\zeta$, obviously:

$$n_e \propto \frac{1}{\zeta} \, . \tag{4.36}$$

Since the ionization is an avalanching effect, it can be further distinguished between tertiary, quaternary, and so forth, electrons (a cascade of ionization events). Obviously, this does not change the result of the scaling.
Due to quasi-neutrality the ion density must be:

$$n_i \propto \frac{1}{\zeta} \, . \tag{4.37}$$

It can now be summarized that all particle densities scale as:

$$n \propto \frac{1}{\zeta} \, . \tag{4.38}$$

From the scaling of secondary electron density follows that its flow towards the cylinder walls and anode scales as the source electrons wall losses:

$$I_{e,secW} \propto \zeta, \quad I_{e,secA} \propto \zeta \ . \tag{4.39}$$

The anode current is the sum of the source electrons and the secondary electrons flow towards the anode and, therefore, follows the scaling of these two currents:

$$I_{e,A} = I_{e,sourceA} + I_{e,secA} \propto \zeta \ . \tag{4.40}$$

Due to the scaling of n_i, like all other wall loses, the ion current towards the cylinder walls scales as:

$$I_{i,W} \propto \zeta \ . \tag{4.41}$$

The entire ion current I_i results from the ionization which, as has been shown, too scale with $\propto \zeta$. It can be assumed that due to its positive potential the ion current reaching the anode is negligible. The ion-current that passes through the outlet is then the entire current subtracted by the wall losses:

$$I_{i,outlet} = I_i - I_{i,W} \ . \tag{4.42}$$

Therefore, this current must scale with $\propto \zeta$ as well. This is the ion-current which generates the thrust.
It can now be summarized that all currents scale as:

$$I \propto \zeta \ . \tag{4.43}$$

The ions leave the thrusters outlet with a velocity:

$$v_{i,outlet} = \sqrt{\frac{2eU_d}{m_i}} \ . \tag{4.44}$$

U_d is the potential difference accelerating the ions and m_i is the mass of the ion, which is (almost exactly) the same as the mass of the atom of the neutral gas species. In order to remain specific impulse unchanged during scaling, $v_{i,outlet}$ must be constant. This concurs with the condition that all velocities being unchanged by the scaling. Since e and m_i are constants, this results in:

$$U_d = U_d^* \ . \tag{4.45}$$

Due to $E = U_d/L$, the axial electric field scales with:

$$E = \frac{E^*}{\zeta} \ . \tag{4.46}$$

However, this scaling occurs obviously self-consistently due to U_d being constant.
Consequently, the maximum velocity that electrons can gain through the potential drop at the thrusters exit (approximately U_d) also stays constant:

$$v_{e,in} = \sqrt{\frac{2eU_d}{m_e}} \ . \tag{4.47}$$

Since $v_{i,outlet}$ and $v_{e,in}$ are the main drivers for the charged particles velocities and the neutrals motion scale self-similar only due to collisions, this validates the assumption for all particles:

$$v = v^* \ . \tag{4.48}$$

Due to the scaling of the outlet ion current the thrust scales as:

$$F = \frac{dm}{dt} v_{i,outlet} = \frac{M}{e} I_{i,outlet} v_{i,outlet} = \frac{M}{e} \zeta I^*_{i,outlet} v_{i,outlet} \propto \zeta \ . \tag{4.49}$$

The thrust efficiency,

$$Mu = \frac{F}{2 I_d U_d} = \frac{\zeta F^*}{2 \zeta I^*_d U_d} = const \ , \tag{4.50}$$

remains constant as expected by this scaling scheme. The results, summarized in table 4.3, are in accordance with Ref. [63].

Table 4.3: The scaling quantities of a thruster discharge channel.

Quantities	scaling
Velocity	$v = v^*$
Magnetic field	$B = \zeta^{-1} B^*$
Particle density	$n = \zeta^{-1} n^*$
Ionization	$S_{ionize} = \zeta S^*_{ionize}$
Current	$I = \zeta I^*$
Mass flow rate	$dm/dt = \zeta (dm/dt)^*$
Electric potential	$U = U^*$
Electric field	$E = \zeta^{-1} E^*$
Thrust	$F = \zeta F^*$
Efficiency	$Mu = Mu^*$

5 Self-similarity scaling analyses and practical application

5.1 Analytical estimation of the change by diffusion and wall-losses

The first investigations of scaling laws for bounded plasmas were undertaken for discharge tubes. This chapter will take a closer look on these laws by analytical considerations and means of numerical simulation. As a very simple approximation for a discharge tube a cylinder is assumed, where one end is the cathode and the opposing end is the anode with given potentials. An axial magnetic field with a homogeneous flux density of 0.6 T is applied, as described in the theoretical considerations in chapter 4.3. It serves as the most basic approximation of the field inside a HEMP thruster.

The diffusion of electrons perpendicular to the magnetic field is a major factor for the plasma properties and, consequently, for the changes of these properties when the system is scaled.

For an axial magnetic field, the diffusion directions are radial and azimuthal. Due to the cylinder symmetry, there is no density gradient in the azimuthal direction and, hence, no net flow due to diffusion into this direction. There is only diffusive flow in a radial direction. This flow must be positive since the bulk of the plasma is at smaller radii while at the radial position of the wall the plasma density approaches zero. Positive radial flow means directed towards the cylindrical wall.

Until now, for the scaling considerations the flux density was defined by use of an arbitrary velocity v (which, as defined previously, is not changed by scaling) for a given density n:

$$J = n \cdot v \ . \tag{5.1}$$

Due to the scaling of the density this flux density J scales as:

$$J = \frac{n^*}{\zeta} v \cong \frac{1}{\zeta} \ . \tag{5.2}$$

Considering the walls surface area, which is the cylinder surface $A = 2\pi RL$, with R and L being the radii and length of the cylinder, respectively, the overall currents to the wall I scale as:

$$I = JA = nvA = \frac{n^*}{\zeta} vA\zeta^2 \cong \zeta \ . \tag{5.3}$$

This is the result found for all currents regarding the scaling laws.

The normal diffusion due to the electron collisions with neutral atoms is dependent on the neutral gas density and the magnetic flux strength. With each collision the center of gyration of an electron and, thus, its average position is shifted by about one gyration radius. Increased neutral gas density increases the collision frequency and, therefore, the diffusion increases. If on the other hand the magnetic flux is increased, the size of the gyration radius is reduced, and therefore the step size by which the average electron position is shifted, is reduced, too. Consequently, the diffusion decreases. The magnetic flux strength, however, contributes with its inverse square to the diffusion coefficient D, who therefore scales as:

$$D = \frac{n}{B^2} = \frac{n^*}{\zeta} \frac{\zeta^2}{B^{2*}} = \zeta D^* \cong \zeta \ . \tag{5.4}$$

The particle flux density can be calculated by the diffusion coefficient and the density gradient dn/dr. For simplicity a linear decay from a maximum value n_{max} at $r = 0$ to $n = 0$ at $r = R$ is assumed. If the spatial distribution of the plasma density remains unaffected by the scaling, the conclusions for diffusion coefficient and flux density remain valid. Under this condition, the gradient term in the flux density can be linearized:

$$J = D\frac{dn}{dr} = D\frac{n_{max}}{R} = \zeta D^* \frac{n^*_{max}}{\zeta} \frac{1}{\zeta R^*} \cong \frac{1}{\zeta} \ . \tag{5.5}$$

This confirms the previous assumption for scaling of the wall flux density.

On the other hand, the anomalous diffusion, also called Bohm diffusion, is, as discussed in chapter 2.9, independent from the neutral gas density and inversely proportional to the magnetic flux strength. This results in the flux density through anomalous diffusion:

$$J_{Bohm} = D_{Bohm}\frac{dn}{dr} = \frac{1}{B}\frac{1}{16}\frac{K_bT}{e}\frac{dn}{dr} = \frac{\zeta}{B^*}\frac{1}{16}\frac{K_bT}{e}\frac{n^*_{max}}{\zeta}\frac{1}{\zeta R^*} \cong \frac{1}{\zeta} \ , \tag{5.6}$$

yielding the same scaling dependence as the 'normal' flux density. This indicates that the scaling law is valid both for normal and anomalous diffusion.

The actual scaling of a thruster shall be called physical downscaling opposed to the numerical downscaling which is applied to the simulated model in order to save computational time. The applied scaling laws are the same. The HEMP thruster uses permanent magnets to generate the magnetic field. Their internal magnetic flux density does not change with the size of the magnet, since its source, the magnetization, is a material constant. Since the entire thrusters geometries are scaled, the ratio between the cross section area of the ring magnets and the cross section area of the cylindrical discharge chamber remains the same. Consequently, in a real device the magnetic flux density remains unchanged by scaling. The version of physical downscaling which takes into account that in practice the magnetic field of the permanent magnets cannot be increased accordingly, will be called practical downscaling.

Under this condition ($B = B^*$), the coefficient for normal diffusion scales as:

$$D = \frac{n}{B^2} = \frac{n^*}{\zeta}\frac{1}{B^{*2}} \cong \frac{1}{\zeta} \ . \tag{5.7}$$

While the Bohm diffusion coefficient:

$$D_{Bohm} = \frac{1}{B}\frac{1}{16}\frac{K_bT}{e} = \frac{1}{B^*}\frac{1}{16}\frac{K_bT}{e} = const \ , \tag{5.8}$$

remains constant.

The particle fluxes consequently become:

$$J = D\frac{dn}{dr} = \frac{1}{\zeta}D^*\frac{1}{\zeta^2}\frac{dn^*}{dr^*} \cong \frac{1}{\zeta^3} \tag{5.9}$$

and

$$J_{Bohm} = D_{Bohm}\frac{dn}{dr} = D^*_{Bohm}\frac{1}{\zeta^2}\frac{dn^*}{dr^*} \cong \frac{1}{\zeta^2} \ . \tag{5.10}$$

As one would expect, the particle fluxes to the walls are larger for a magnetic confinement which is less strong than demanded by the scaling law, compared to a confinement that follows all of the scaling criteria.

The relative decrease in plasma density might not be as severe as this radial migration indicates, because a significant amount of electrons might traverse in

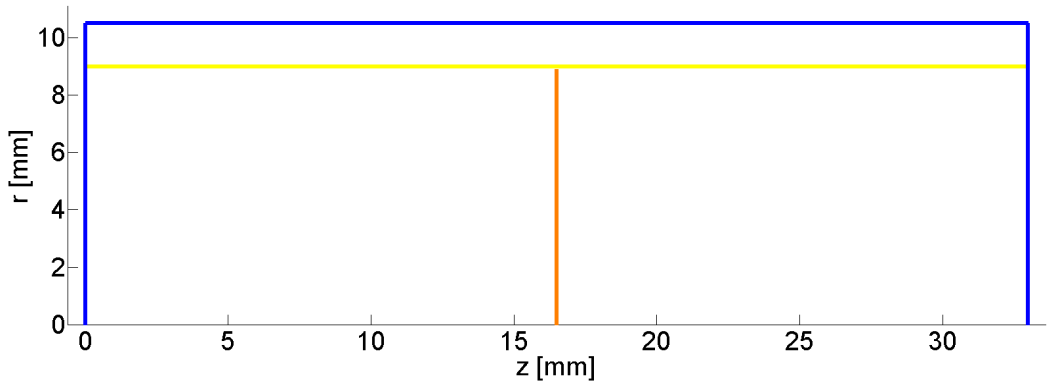

Figure 5.1: Unscaled simulation domain: ground potential (blue), dielectric surface (yellow), electron source (orange).

the axial direction the entire distance from cathode to anode instead impacting the cylindrical walls. The ratio between this wall losses and the current to the anode will be investigated by numerical simulations described in the next chapter.

5.2 Test of the self-similarity scaling schema

To investigate the wall losses due to diffusion and its relation to the scaling laws, a numerical model of PiC type has been set up. The basis for this model is a cylinder of 5.5 mm length, which is the distance between two magnetic cusps of a typical micro-HEMPT. The domains are to be used in further simulations, and the region they represent spans from $z = 5.5$ mm to $z = 11$ mm in the downscaled version of the HEMP thruster.
While the magnetic field in this model does not consist of a cusped structure, this choice in length allows comparison with models that include a single cusp. The diameter of the discharge chamber of 1.5 mm is also taken from typical mirco-HEMPT dimensions. A thin-coated dielectric of 0.25 mm is assumed. Including the dielectric, the simulation domain is of size $z = 5.5$ mm and $r = 1.75$ mm. Representing the unscaled system, a six times larger geometry is applied (Fig. 5.1). The resulting discharge chamber diameter of 9 mm is a typical value for a DM3a-type HEMPT. The dielectric thickness of 1.5 mm is also common for this type (other thicknesses, like 1 mm, were also used.)

The simulation is of type 2D in cylinder symmetry. Therefore, the simulation domain is in the r-z-plane. Each simulation domain consists of 175×550 cells. The grid resolution has no particular importance for the simulations presented here, since electron density will be such low that the Debye length does not need to be considered.

The domain boundary that lies along $r = 0$ is the symmetry axis. The remaining three boundaries are grounded; accordingly their potential is defined as zero. At the dielectric surface, that is along $r = 1.5$ mm for the smaller domain and $r = 6$ mm for the larger domain, surface charge accumulation is accounted for.

As a value for the magnetic flux density, the average of 0.6 T from the micro-HEMPT is taken. This value is implemented as a purely axial field over the entire domain. For a real device, such a field could be approximated by use of a single magnetic ring whose length significantly exceeds the discharge chamber. The unscaled model consists of two versions, one where the magnetic flux density is reduced accordingly to the scaling law (physical scaling) to 0.1 T and one where it remains at 0.6 T as it is the case for practical scaling. While untypical, the value of 0.1 Tesla could also be achieved by using magnets with low magnetization. It would appear more straightforward to take the values from the unscaled system and calculate the quantities for the downscaled one. However, since the main focus is on the comparison of the occurring differences due to scaling it does not matter which system is the starting point. Moreover, the unscaled system as the starting point would yield flux densities of 3.6 T for the downscaled system which is impossible to archieve by permanent magnets. With this approach, the self-similarity of the scaling law can be checked by comparing the unscaled system with 0.1 T to the downscaled system with 0.6 T. Additionally, the effects for real devices (practical scaling) can be investigated by comparing the 0.6 T unscaled system to the 0.6 T downscaled system.

It was originally intended to place an electron source at the very right end (maximum z-value) of the simulation domain. The electrons would be given a negative z-velocity so that they travel to the very left end which represents the anode. Then the electron wall losses along their way would be compared to this 'anode current'. It became apparent that the collisions cause many of the electrons to return and impinge at the right end instead at the wall. This made it unfeasible to compare the wall losses to the 'anode current' which is the main goal of this simulation. Therefore, the electron source is set halfway of the z-distance and its z-velocity is Maxwellian distributed in both directions. Its source-strength (new electrons per time, per volume) is uniformly distributed from $r = 0$ mm to $r = 1.5$ mm. The domain can now be treated as two mirror-symmetric parts. Due to the mirror-symmetry it is sufficient to investigate the left half. Its right boundary is the mirror-line which now represents the electron source. The electrons reversing their travel direction do not matter anymore in this setup since the same amount leaving through the mirror-line enter through it from the other half.

While the electron positions are assigned for two dimensions of the cylindrical coordinate system, z and r, their velocity vectors are calculated for all three

dimensions, axial, radial and azimuthal (v_z, v_r and v_φ). This is necessary for proper calculations of the gyration motion in the magnetic field where the Lorentz force can have an azimuthal component (chapter 3.5). Also, the code treats collisions as three-dimensional by assigning each electron not only an axial and radial but also an azimuthal velocity component after a collision event.

The axial velocity of the injected electrons is Gaussian distributed, equivalent to 10 eV mean kinetic energy. Additionally, they have a fixed initial tangential velocity equivalent to 10 eV as well. The initial tangential velocity serves for initiating the gyration motion. The sign of the axial velocity is set in a manner that the resulting initial Lorentz force is oriented in negative radial direction. This permits electrons that are injected near 1.5 mm to impact immediately on the wall. Otherwise, there would be a significant systematic error in the measurement, hindering its intend to determine the current towards the walls caused by radial diffusion.

The super-to-real particle ratio for the electrons is set to unity so that each particle yields the lowest possible electric field. The overall source strength is also very low being for each mirror-half 50 nA for the downscaled system and according to the scaling law 300 nA for the unscaled system. The resulting very low space charges combined with the grounded domain boundaries results in negligible electric fields. Under this condition the diffusion can be investigated, only considering the effects of collisions and magnetic fields without any other interference. For simplicity of the investigation, no Bohm diffusion is implemented in this model and only classical diffusion due to collisions with neutral particles occur.
In the downscaled discharge chamber the neutral gas simulation which will be described later yielded for the selected region an average density of $4 \cdot 10^{20}$ neutrals per cubic meter. A uniform density of this quantity is initialized for this model up to the radius of the discharge chamber inner wall (1.5 mm). For the unscaled version the area filled with neutral gas is accordingly six times larger in both dimensions and the density six times lower according to the scaling laws, which is here $6.67 \cdot 10^{19}$ neutrals per cubic meter. The neutral gas is initialized by inserting neutral particles and then the particles are kept static. Their mean density per simulation grid cell is used for the Monte Carlo code to calculate the probability of electron-neutral collisions. Depletion of the neutral gas due to ionization is negligible due to the very low electron currents (and is not accounted for).

The shortest distance an electron can travel on a straight line from one end of the simulated cylinder to the opposing end is its length, 5.5 mm. As a result of the electrons initial velocity vector and the applied magnetic field, its trajectory is a helix which increases the traveled distance by factor a 1.41 to

7.8 mm.

The initial mean kinetic energy resulting from its two velocity components is 14.1 eV ($v = \sqrt{v_z^2 + v_\varphi^2}$).

At this energy, the cross section for elastic electron-neutral collisions is $9.4 \cdot 10^{-20}\mathrm{m}^2$. The mean free path is then 19 mm. For excitation collision the mean free path is 104 mm and for ionizing collisions 301 mm, based on the according collision cross sections diplayed in Fig.5.2

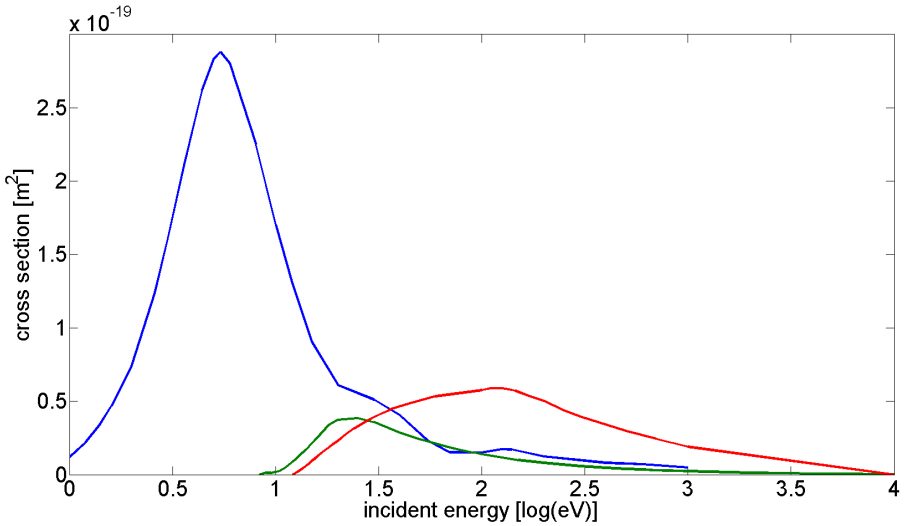

Figure 5.2: Electron-neutral collision cross sections, evaluated from experiments [69], [70], [71]. Blue: elastic, green: excitation, red: ionization.

Consequently, a significant amount of electrons can leave the system without having encountered even a single collision.

Due to this result it becomes evident that the magnetic cusps play an important role in the magnetic confinement of a HEMPT, since due to their magnetic mirror effect the electrons can oscillate several times between them. Therefore, they can travel the distance between them (about 5.5 mm) several times and the number of their collisions is accordingly increased. A further conclusion is that with a purely axial field and for this neutral gas density, it is not ensured that the system is collision-dominated. But this assumption is a requirement for a proper testing of the scaling law, since this law includes the Knudsen number (a dimensionless factor, see chapter 4.1). Hence, for this virtual experiment, the density is set an order of magnitude higher to $4 \cdot 10^{21}$ neutrals/m^3 and $6.67 \cdot 10^{20}$ neutrals/m^3 for the downscaled and unscaled system, respec-

tively.

Ionizing collisions are excluded from this model since the additionally generated electrons would add to the currents, while this analyses focuses on the flow of the source electrons. Since excitation collisions are also excluded the energy and, thus, mean velocity of the source electrons remain constant. As shown before, the elastic collisions anyhow have the largest cross section for the source electrons at the set energy. These are the test conditions, which should ensure that in a simplified and systematic way the diffusion due to collisions can be analyzed. A virtual measurement of the wall current is implemented by counting how many electrons per time are absorbed by the grid cells along the line $z = 0$ mm to 2.75 mm at $r = 1.5$ mm. These numbers are the geometric values for the one half of the downscaled version. For the unscaled version the geometric values are accordingly 6 times larger. For the anode current the 'measurement' is performed along the line $z = 0$ mm, $r = 0$ mm to $r = 1.5$ mm for the downscaled version. For the unscaled version these values are again accordingly 6 times larger.

5.3 Discussion of the self-similarity scaling schema test

The electron density of the unscaled system for a magnetic flux density of 0.1 T can be seen in Fig. 5.3 b). It is clearly visible that the electron density decreases near the dielectric wall due to increased losses. This is in contrast to the 0.6 T simulation in Fig. 5.3 a) where the decrease of electron density near the walls is much less. In principle, this observation confirms the calculations about how the diffusion changes in relation to the magnetic flux strength (chapter 5.1). Due to the diffusion the electrons are caused to migrate both in positive and negative radial direction. Electrons collected around $r = 0$ cause a significant peak in density for the version with stronger diffusion (0.1 T). The relative electron density distribution of the downscaled version (0.6 T) is very similar to its unscaled counterpart (0.1 T) as can be seen in Fig. 5.3 c). Here, the maximum of the colorbar is adjusted by a factor of 6 to account for the density change resulting from the scaling law.
The unscaled system with 0.1 T magnetic flux strength provides 282.7 nA anode current and 15.1 nA wall losses. The simulation was run over 100000 time steps and the result are from averaging over the last 30000 time steps. The sum of the resulting currents is 297.8 mA. This is very close to the input value of the source current and the small deviation can be contributed to fluctuations in the finite number of particles used. The source current was set extremely low to ensure that the electric fields generated by the electrons are negligible.

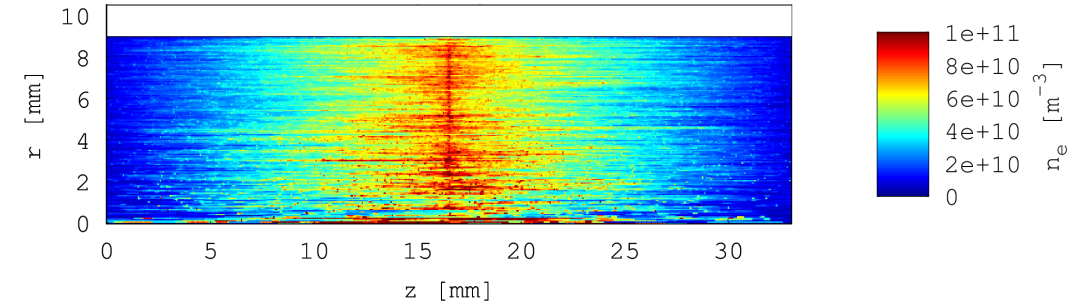

(a) unscaled 0.6 T

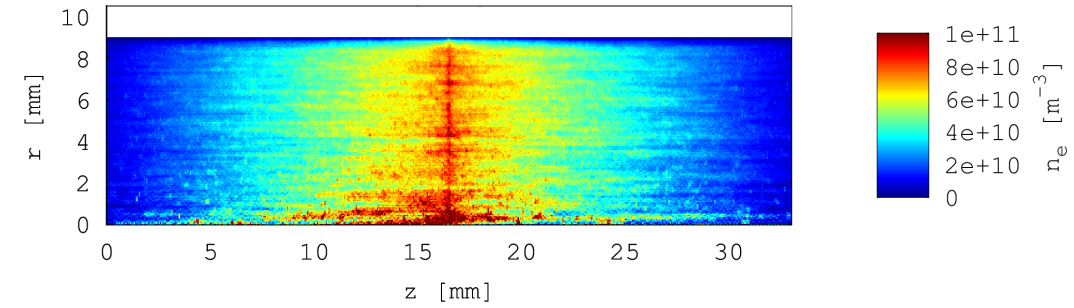

(b) unscaled 0.1 T

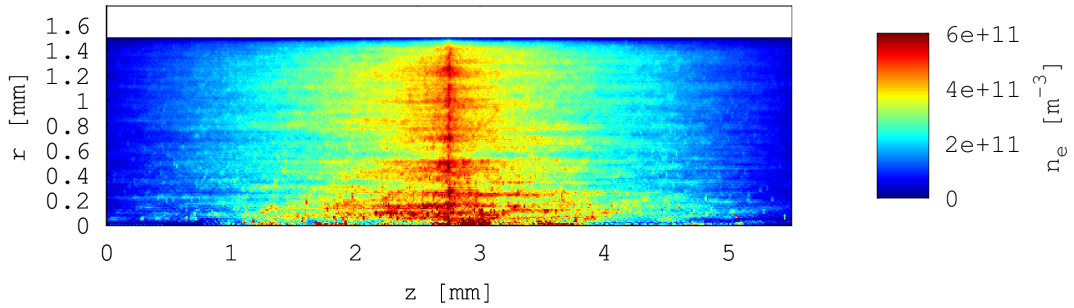

(c) downscaled 0.6 T

Figure 5.3: Electron density profile of plasma channels with electron source and axial magnetic field.

The wall loss ratio, which is defined as wall losses divided by source current, is 0.0534. The downscaled system for 0.6 T following the self-similarity scaling was also run over 100000 time steps. The results were also obtained from averaging over the last 30000 time steps. The anode current is 47.23 nA and the wall losses are 2.54 nA. Again, the sum provides a good match with the source current. The wall loss ratio is 0.0538 which is almost the same as for the unscaled system, proving that the self-similarity of the diffusion (towards the walls) is valid. The unscaled version with 0.6 T was run over the same time span. It delivers 298.3 nA anode current and 2.99 nA wall losses. Being 0.01, the wall loss ratio is about five times lower than for the other two versions. An overview of the wall losses for all three models is given in table 5.1. It can be concluded that increasing the system size while keeping the magnetic flux density constant the wall losses decrease vastly. Vice versa, reducing the system size while keeping the magnetic flux density constant the wall losses increase rapidly. This fact might be a major hurdle in the micro-HEMPT development because there are limits for increasing the field strength of permanent magnets. The simulations in the following chapters will further investigate the effects on more complete plasma (electrons and ions), cusped magnetic fields and, finally, the entire HEMP thruster.

Table 5.1: Overview wall losses.

	wall loss ratio
unscaled (0.6 T)	0.0100
unscaled (0.1 T)	0.0534
downscaled (0.1 T $\Rightarrow$ 0.6 T)	0.0538

5.4 Scaling of cylindrical segment with an axial magnetic field

In the following, the scaling laws described in the theoretical section (chapter 4.3) are investigated for its application in plasma discharges. Precisely, the following simulations will focus on the application of the self-similarity scaling law described by Taccogna et al. [13] with the idea to save computation time (computational scaling). In the previous simulations the charged particles were only the electrons with a density that each electron could be treated in a single particle model (although this was not done, rewriting the Particle-in-Cell code to reduce its capabilities albeit increasing its speed was not worth the effort for these few simulations). Now the simulations concern both charged species (electrons and ions), with a density where collective behavior is present. Combined with the conditions for plasma frequency, Debye length and Debye

sphere, all plasma conditions are fulfilled in this model.
The used unscaled system is actually the downscaled configuration (practical scaling) from the previous simulation. The reason is that the dimensions of the micro-HEMPT are equivalent to a downscaled DM3a HEMPT. Obviously, the micro-HEMPT is more sensitive to downscaling than DM3a HEMPT. In chapter 4.3, the downscaled tube was divided into a finite number of smaller volumes where to each the scaling law was applied, and the overall result was assumed to provide the same relative spatial distribution of particle densities. It has to be validated whether that assumption holds true. Analysis of the self-similarity scaling law does not account for deviations due to space charges. Since a downscaled system does not contain as many charged particles as the unscaled one, deviations in the electric potential distribution which can be caused couples back to the charged particle density distribution. This is especially evident for the Debye length and plasma sheath thickness. Since the Debye length scales only with the root of the scaling factor it becomes relatively larger towards the system size. If the plasma sheath is e.g. 10 Debye lengths thick it becomes relatively larger as well. Consequently, the size of the bulk plasma decreases which may influence all other plasma parameters. It has to be investigated for the applied scaling factor if these expected deviations become significant. The relative increase in the Debye length reduces the grid cells per domain which is one of the main advantages of the scaling law. Therefore, the issue of the space charge deviation cannot be avoided and it needs to be investigated, whether it is significant or not.

Like in the previous chapter the discharge tube dimensions are: length of discharge chamber of 5.5 mm, radius of 1.5 mm and a dielectric thickness of 0.25 mm. An electron source is placed at the right side of the domain ($z = 5.5$ mm) whose intensity is evenly distributed in the radial direction (Fig. 5.4). Combined with this side of the domain being grounded, the electron source acts as a cathode. On the left side of the domain ($z = 0$ mm) an anode voltage of 200 V is set which drives the plasma discharge. The upper side of the domain (along $r = 1.75$ mm) is grounded. Both the anode and cathode are absorbing for charged particles. The amount of positive and negative charges (electrons and ions) per time is calculated in currents for the virtual diagnostics. Along $r = 1.5$ mm the surface charge accumulation of the dielectric is considered. The currents towards this surface are also measured by in the diagnostic. In steady state, the fluxes of ions and electrons toward this wall should be equal, because no net currents are possible through the dielectric and in the final state the surface charge does not change with time.

In this simulation the most prominent electron-neutral collisions (elastic, excitation and ionization) are included. Also, electron-electron Coulomb collisions are calculated since their mean free path is in the same order of magnitude as

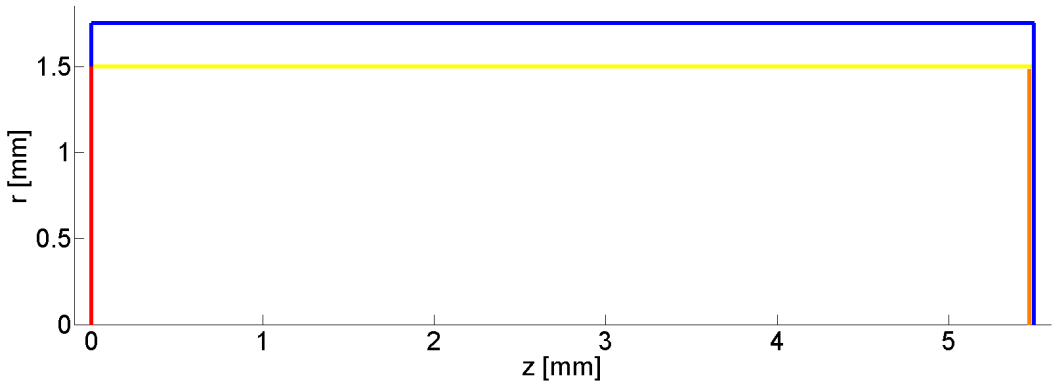

Figure 5.4: Unscaled simulation domain: ground potential (blue), anode potential (red), dielectric surface (yellow), electron source (orange).

the size of the system. In addition, ion-neutral charge exchange and momentum exchange are included [72], although this is more likely to be important for the simulation of a complete thruster (including near exit region).

To study the scaling law in the presence of magnetic flux, an axial B-field is applied. For the unscaled system, like in the previous chapter, the neutral gas density is $4 \cdot 11^{21}$ m^{-3} and the magnetic flux is 0.6 T, while the electron source current is 1 mA. The scaling factor for the downscaled system is 8. This factor is the same as for the micro-HEMPT models described in the following chapters. As required by the scaling law, these values are changed to $3.2 \cdot 10^{22}$ m^{-3} neutral gas density, 4.8 T, and 0.125 mA, respectively. In the unscaled domain the grid is set to a cell size of $1 \cdot 10^{-3}$ m, which is sufficient for a plasma density of $5 \cdot 10^{18}$ m^{-3}. The downscaling reduces the cell size to $1.25 \cdot 10^{-4}$ m, which results in a maximum sustainable plasma density of $3.2 \cdot 10^{20}$ m^{-3}. According to the scaling law the plasma density is only expected to rise by the scaling factor to $4 \cdot 10^{19}$ m^{-3}. The grid resolution could be reduced accordingly, but this is not done here since the computational requirements are relatively low compared to the model of a complete thruster.

5.5 Results with regards to the scaling law

The results obtained here serve as a validation for the analytical considerations of the scaling law in chapter 4.3. They ended with the idea that the scaled volume could be assumed as divided into many elements, yielding the same density profile if the scaling law counts for each individual element. Possible changes in electric potential were not accounted for in these analytical considerations.

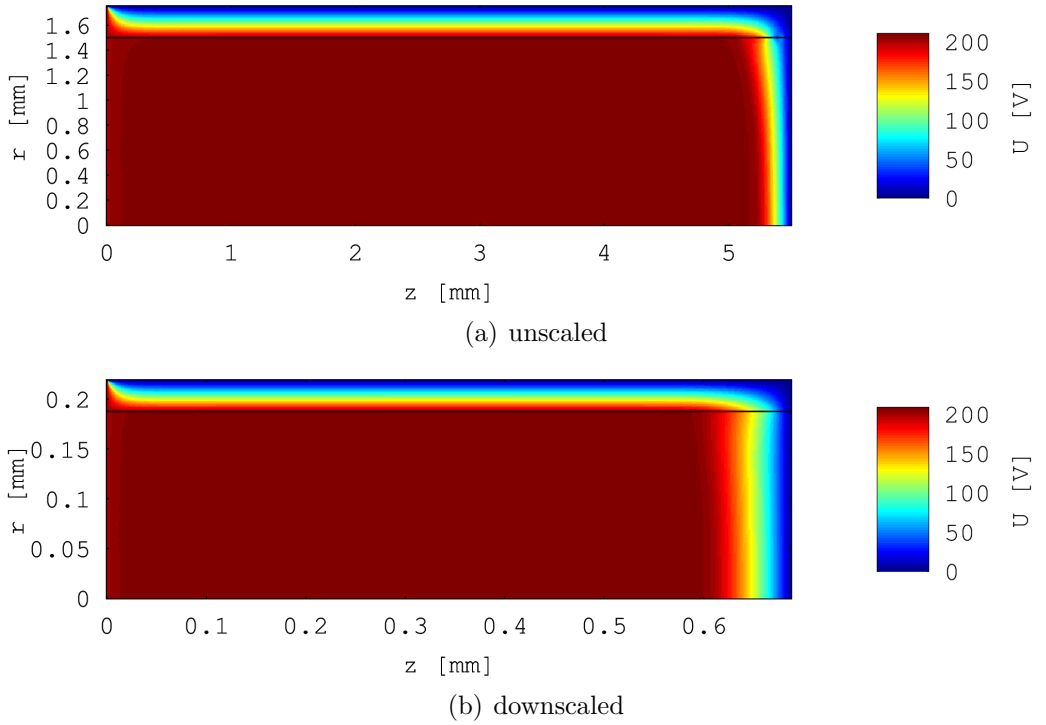

(a) unscaled

(b) downscaled

Figure 5.5: Potential profile of unscaled and downscaled system.

The electric potentials of the unscaled and scaled system are shown in Fig. 5.5 a), b). The plasma potential is mostly uniform at a few volts above the anode potential. For the most part, the dielectric surface is now on a potential similar to the anode as well (at the beginning of the simulation its potential was 0 V). The potential slope at the symmetry axis is shown for both domains in Fig. 5.6 with the z-distance normalized to the discharge tube length in order to enable a comparison. As expected, the plasma sheaths (at anode and cathode) are relatively larger in the downscaled system.

In Fig. 5.7 the ion densities of both systems are shown. The distribution is similar, albeit there is a difference in the radial positions of the density maxima. As expected, the smaller system is more wall-dominated. Consequently, the relative radial drift to the wall is stronger. Therefore, the density maximum is slightly shifted radially towards the wall.

The anode current of the unscaled system is 1.89 mA and for the downscaled system re-calculated to the unscaled one (multiplied by 8) it is 2.15 mA. The wall losses are 1.6 mA for the unscaled system and 1.45 mA (re-calculated) for the downscaled system. The deviations are only 13 % and 11 % for anode current and wall losses respectively for the scaling factor of 8.

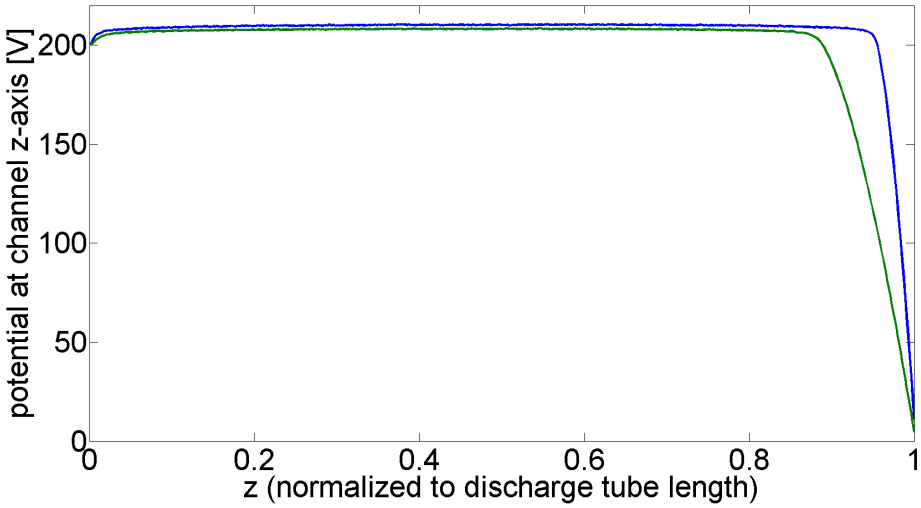

Figure 5.6: Potential along z-axis of unscaled (blue) and downscaled (green) system.

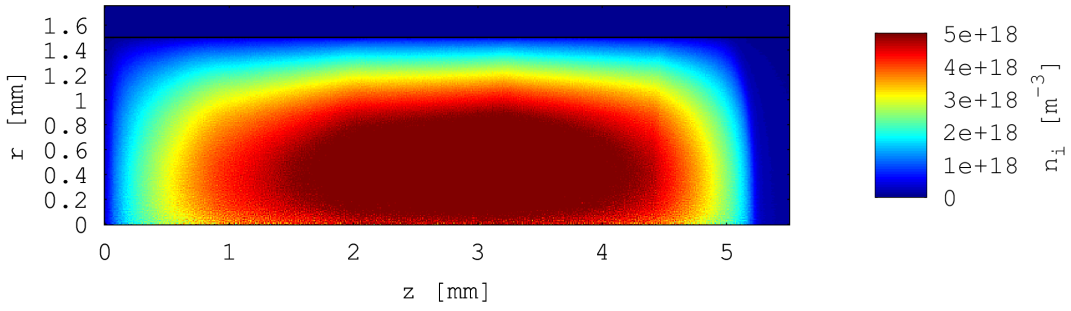

(a) unscaled

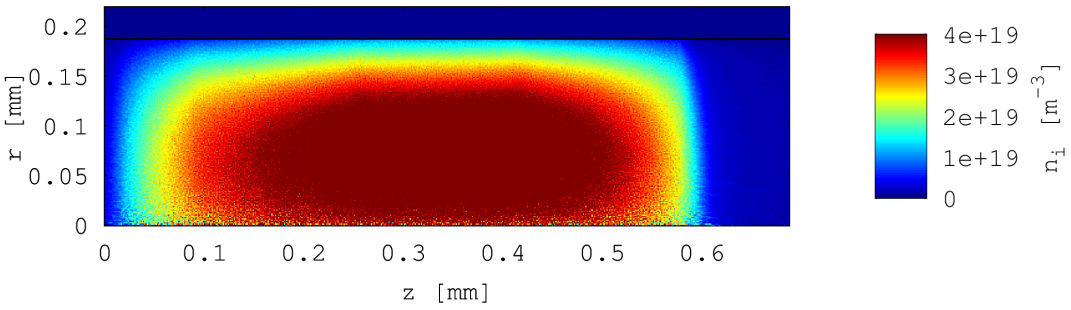

(b) downscaled

Figure 5.7: Ion density profile of unscaled and downscaled system.

6 Practical scaling of a HEMPT discharge channel section

6.1 Scaling of cylindrical segment with cusped magnetic field

The most typical feature of a HEMPT is its cusped magnetic field structure. The magnetic cusps have a significant influence on the plasma properties within the discharge channel. How the plasma parameters in the vicinity of such a cusp change from an unscaled to a downscaled system needs to be investigated. For this purpose, a section of the discharge channel for an unscaled (DM3a HEMPT-like) and for a downscaled HEMPT are simulated with simplified boundary conditions.

Like for the previous simulations, the domain sizes are 5.5 mm axial length, 1.75 mm radial length and 33 mm axial length, 10.5 mm radial length for the downscaled and unscaled system, respectively.

For the downscaled configuration, the same periodic arrangement of magnets as for the micro-HEMPT is used for the simulation. The axial length of the magnetic rings is 5 mm while for the distance rings this length is 0.5 mm. The radii of the magnetic rings and distance rings are taken from the micro-HEMPT arrangement which has 0.25 mm thickness of the dielectric (chapter 8.3). This results for the unscaled geometry to have a dielectric thickness of 1.5 mm, which is more typical for DM3a HEMPT thrusters. Otherwise, in the unscaled version, the resulting value of 6 mm would be unusually thick.

Since the final goal of these simulations is a comparison to a normal, unscaled HEMPT, 0.25 mm thickness for the downscaled version appears to be the better choice than 1 mm. This reduces the inner radii of these rings from 2.5 mm (1 mm thickness version) to 1.75 mm. Their outer radius is set to remain the same, which is 15 mm for the magnetic rings and 8 mm for the distance rings.

Instead of three, there are four magnets in this simulation setup (Fig. 6.1). With the generated magnetic topology, the cusp area between the second and third magnet is perfectly mirror-symmetric (the assumed mirror axis is halfway between these two magnets). With this setup, the analysis of the result will be

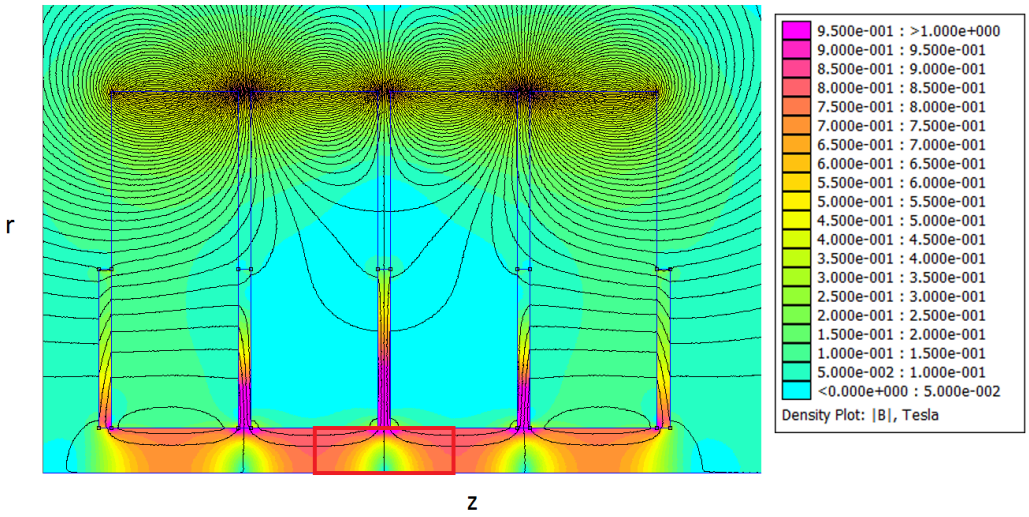

Figure 6.1: Magnetic topology of the periodic ring magnet setup. Region used for plasma simulation marked red (equals HEMPT discharge channel section).

simplified by eliminating effects due to an asymmetric magnetic field. The entire setup of the rings ranges from $z = 0$ mm to $z = 22.5$ mm, and the selected region from 8.5 mm to 14 mm. In the plasma simulation, for convenience, the z-origin will be set to the beginning of this region (8.5 mm).

The magnetic field is calculated using the finite element software FEMM. Due to the cylinder symmetry of the problem a cylinder coordinate system is used and only on a r-z cut plane calculated while φ is arbitrary. This 2D simulation saves significant computation time towards a 3D approach without sacrificing any accuracy of the result. The magnetic field is calculated on a triangular mesh. It means that a finite element method is used. The simulation domain ranges from $z = -34.5$ mm to $z = 57$ mm, $r = 0$ mm to $r = 50$ mm. In the region $z = -9.5$ mm to $z = -32$ mm, $r = 0$ mm to $r = 25$ mm, the mesh is finer for more accurate simulation of the details of the magnets setup. The boundary conditions have to be defined such that the magnetic field lines are parallel to the domain boundaries. A magnetic field occupies infinite space, even if it becomes weaker with increasing distance from its source. Consequently, these boundary conditions create an unphysical deviation from the real case. Therefore, the simulation domain has to be significantly larger than the magnets setup whose field is to be simulated. Therefore, a large surrounding region of the magnetic parts is simulated, to keep the deviations small.

The calculation is performed as described in the theory section, chapter 3.1, by using the magnetization of samarium-cobalt, which is the material the magnetic

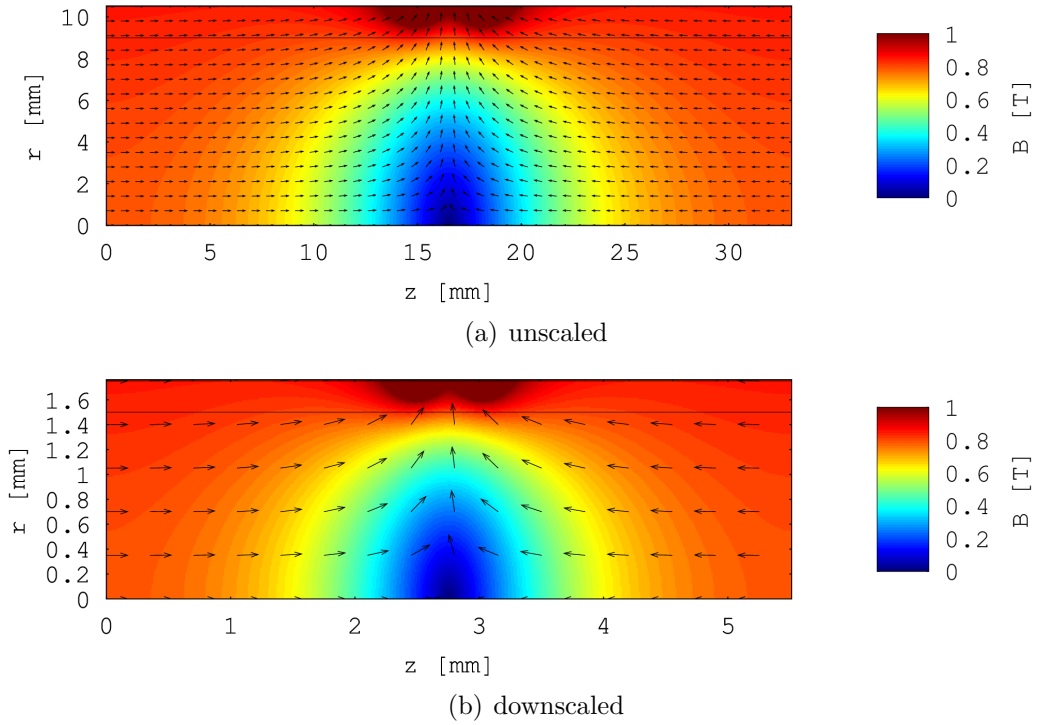

(a) unscaled

(b) downscaled

Figure 6.2: Magnetic flux density of a HEMPT discharge channel section.

rings are made of. The distance rings consist of the weak iron type 'Carbon steel forgings, annealed'. The materials magnetic permittivity is applied.

For the unscaled system, a six times larger geometry is set. As expected, the result yields the same maximum magnetic flux density as for the downscaled system (Fig. 6.2).

Like in the previous simulations, the domain represents the region of the downscaled HEMPT discharge chamber from $z = 5.5$ mm to $z = 11$ mm, measured from the anode, and six times larger values for the unscaled version.

Based on the neutral gas simulation, the neutral gas densities are set to $4 \cdot 10^{21}$ m^{-3} and $6.66 \cdot 10^{20}$ m^{-3} for the downscaled and unscaled system, respectively. No depletion of the neutral gas due to ionization is accounted for. Keeping the neutral gas as a static background removes one variable from the system. Thereby, it enables the investigation to be more focused on the changes in e.g. diffusion and ionization.

While not entirely realistic, a static neutral gas background is supposed to yield more defined results for the other parameters. This would be less the case under the condition of a neutral gas which varies spatially and temporally.

At the initialization of the simulation the neutral particles are injected into the domain with a Maxwell distributed velocity that concurs with a temperature of 473 K (200 C°). This is the assumed neutral gas temperature within the discharge channel. While having no meaning for the neutrals in this model (since they are defined as being immobile), this temperature gives the initial velocity of ions generated by ionization.

Both the magnetic flux and neutral gas density are implemented as static values in the plasma simulation. The domain boundaries are set to approximate the condition inside a section of the discharge channel. Since the near exit region is not a part of this model, it resembles more an enclosed plasma discharge tube.

The electrical boundary conditions are the same as in the discharge tube simulations with the left side of the domain acting as an anode, and the right side acting as the cathode (Fig. 6.3). The generated potential difference drives the plasma discharge. While a typical setup for this type of micro-HEMPT is 400 V anode potential here 200 V are applied. This change has been done for the purpose of roughly keeping the power to volume ratio for this segment, since it is less than half the length of the full discharge channel.

Also, like in the previous simulation, the number of absorbed electrons and ions at the anode and cathode are calculated to currents for the 'virtual' diagnostics. At the inner wall of the discharge chamber (along $r = 1.5$ in downscaled configuration) charge accumulation on the dielectric surface is accounted for. Again, the currents towards this surface are evaluated in the virtual diagnostic. For the volume that is occupied by the dielectric (1.5 mm $\leq r \leq$ 1.75 mm, 0 mm $\leq z \leq$ 5.5 mm; downscaled configuration) the electric permittivity of the dielectric material used in the micro-HEMPT (Al_2O_3) is applied, which is $\epsilon_r = 9$.

A simple secondary electron emission model is used at the dielectric wall surfaces, where half of the impacting electrons are re-ejected with 90 % of the incident energy.

For the right side of the domain to truly act as a cathode at this location an electron source must be realized. For this model, the source is placed not exactly at the boundary, but very close to it, from $z = 5.48$ mm to 5.49 mm. Thereby, it is ensured that the injected electrons are immediately dragged towards the anode through the potential drop without the need of a high artificial velocity in negative axial direction. The initial velocity used in this model is rather low with Maxwell-Boltzmann distributed electrons of 2 eV energy. The only purpose is to ensure that the electrons have an initial velocity in all three dimensions. In a discharge tube most of the source electrons originate from ions impacting the cathodes metall. Yet the right boundary of this domain

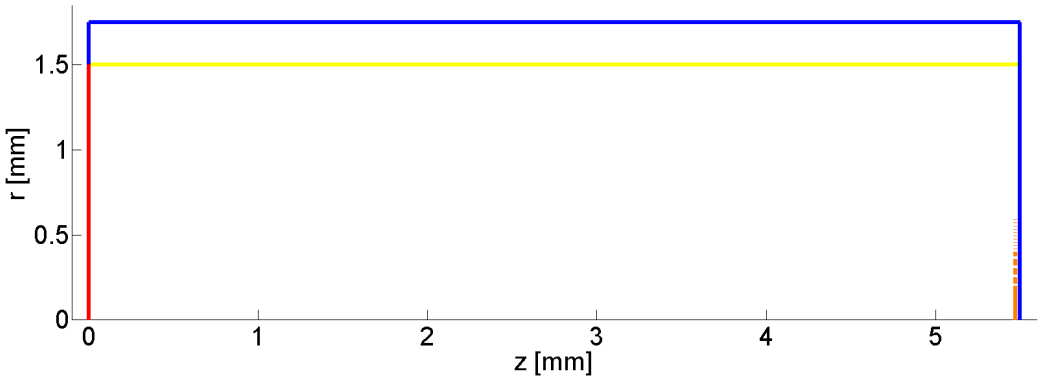

Figure 6.3: Scaled simulation domain: ground potential (blue), anode potential (red), dielectric surface (yellow), electron source (orange).

translates to an imaginary boundary near the HEMP thrusters exit.

The flux of electrons through this imaginary boundary can be calculated in the complete thruster simulation which will be described in the following chapter (7). As expected, the sign of the axial component of the mean flux is negative, so there is a net flux towards the anode. While their density maximum is at a medium radius, the velocity of the electrons has a strong maximum at $r = 0$, resulting in the flux maximum being at $r = 0$ as well. For the model, this result is simplified and approximated by giving the source strength an r-dependent Gaussian distribution with $\sigma = 0.2$ mm.

The thruster simulation does not distinguish between the source electrons, which have their origin outside the thruster and those generated by ionization. Also, since this simulation consists only of a segment of the discharge channel, it cannot regard electrons oscillating between the one cusp which is included in the domain and the exit cusp and/or the potential drop at the near exit region of the thruster. Hence there are limits on how proper the right side conditions of this model can be. If a flat potential as in the discharge channel is achieved, then most of the potential drop would occur close to the cathode and electrons would oscillate between the cusp and the vicinity of the cathode. Therefore, for most of the simulated volume conditions similar to the ones inside the discharge channel should be achievable.

The same types of collisions are included as in the discharge tube models (chapter 5.4) to ensure that the ionization process is accurately simulated.

6.2 Results: comparison of downscaled and unscaled cusp area

By the results, the differences between the two models can be analyzed. During the following descriptions, for each model the cusp will be regarded as a divider into two regions. With respect to the ion motion these areas will be denominated upstream of the cusp from $z = 0$ to the z-position of the cusp, and downstream of the cusp from the z-position of the cusp until the maximum z-value. The spatial profile of the electrons shows significant differences between the two cases investigated as can be seen in Fig. 6.4 a), b).

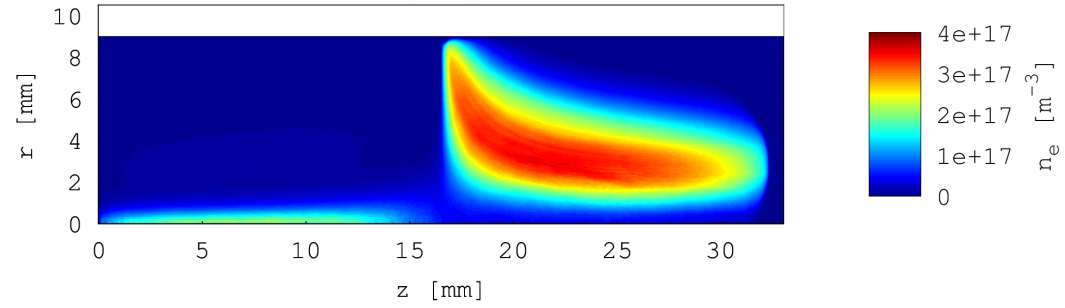

(a) unscaled

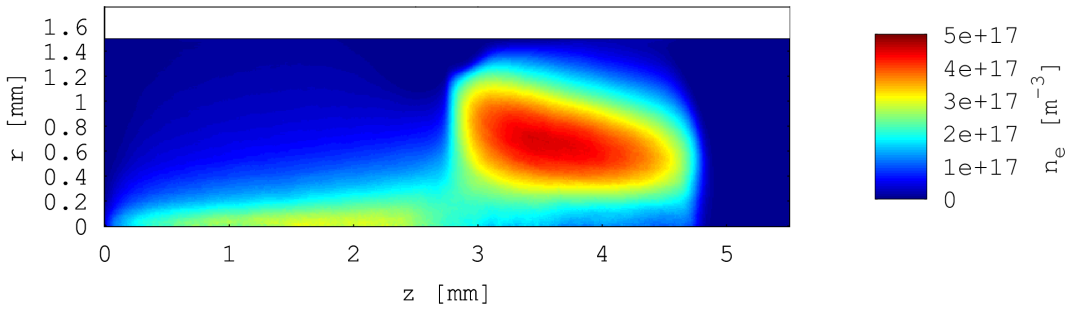

(b) downscaled

Figure 6.4: Electron density profile of a HEMPT discharge channel section.

Nevertheless, there is a likeness in both models: The electrons migrate to larger radii (the electron source has its peak density at $r = 0$). Due to their low collision frequency it is reasonable to assume that the electrons oscillate several times between the proximity of the discharge chamber inner wall at the cusp position and the proximity of their source at the right domain boundary. At the cusp z-position, in proximity to the wall, the magnetic mirror effect (chapter 2.4) reduces the likelihood of an electron reaching the wall (here, the magnetic flux increases towards the wall).

Near the right domain boundary occurs the main potential drop, as can be

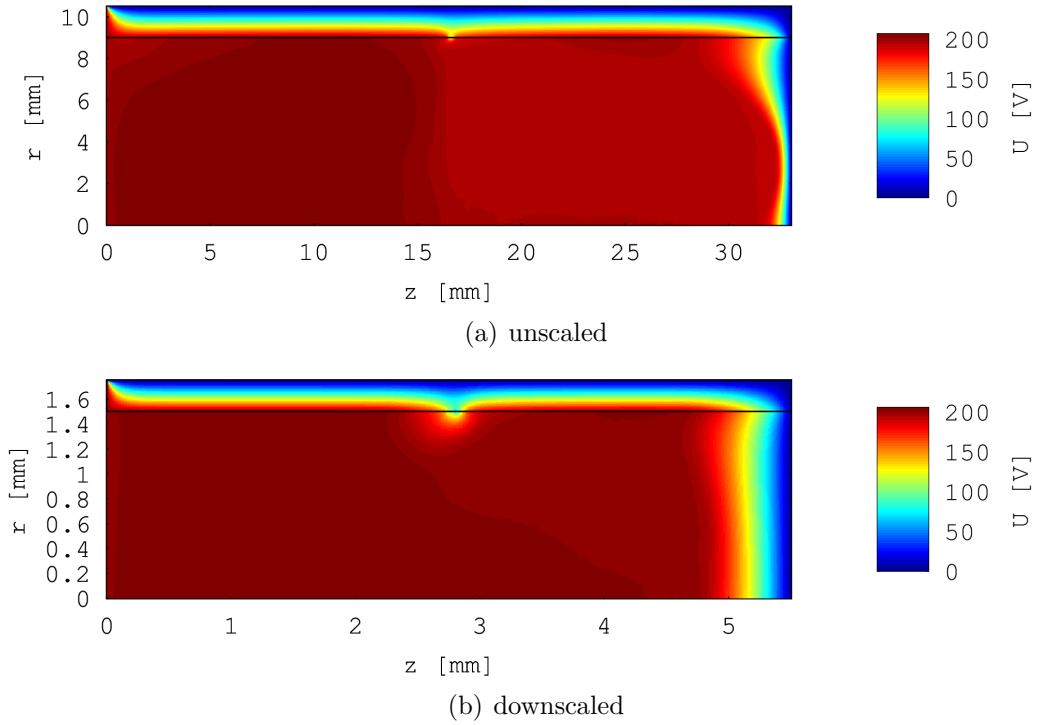

Figure 6.5: Potential profile of a HEMPT discharge channel section.

seen in the potential profile in Fig. 6.5 a), b). This drop prevents the electrons from reaching this boundary since they obtain their energy from this potential drop and, consequently, they cannot return with an energy that is sufficient to overcome it. Consequently, the electrons are reflected by the potential drop and oscillate between the cusp and this drop. This emulates as close as possible the oscillation the electrons undergo in a complete thruster. There they oscillate between this cusp and the near exit region of that thruster. As the electrons go back and forth along the magnetic field lines, due to normal and anomalous diffusion, they migrate perpendicular to these field lines. The field lines are mostly in axial direction except for the proximity of the z-position of the cusp. Due to the cylinder symmetry the mean radial motion of this migration can only be positive since the source is concentrated around $r = 0$ and the sink is the cylinder wall. Since the electrons increase their number due to ionization as they migrate in positive radial direction, their density maximum is shifted to higher radii. In the downscaled model the electron density has its maximum about halfway of the radial distance to the wall and the distribution is rather diffuse, whereas in the unscaled version the maximum is relatively close to the z-axis. In the latter the distribution is more influenced by the shape of the magnetic field lines. While in absolute values the magnetic flux is the same for both models, in the downscaled version it is weaker compared to the value expected according to the self-similarity scaling. Consequently, in

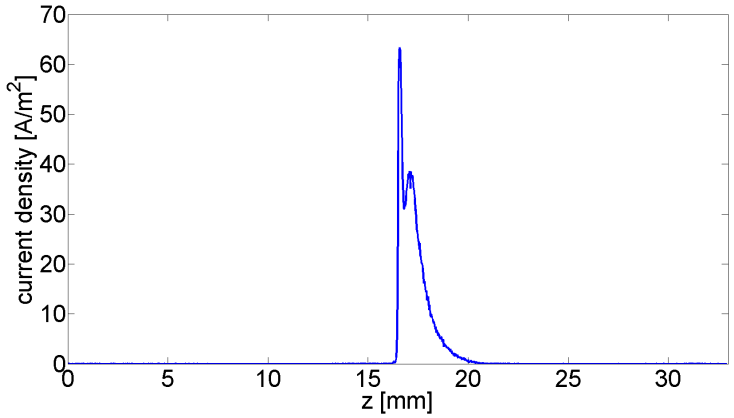

(a) unscaled

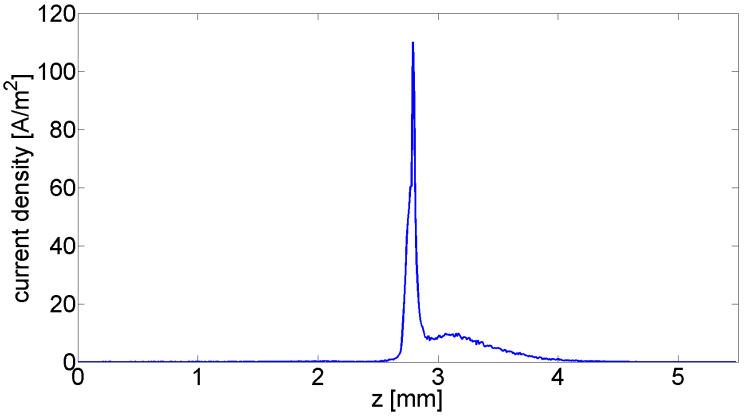

(b) downscaled

Figure 6.6: Density of ion current towards the wall of a HEMPT discharge channel section.

the downscaled version the electrons are less strong influenced by the magnetic field, while in the unscaled version they follow the magnetic field lines more strictly. This results in the observed differences of the electrons density profile

Eventually, a significant amount of electrons impacts at the discharge chamber wall. In the simulation models, their current density along the z-axis can be determined by counting the electrons per time being absorbed by each grid cell at this wall position. The results are shown in Fig. 6.6 a), b). In both cases, there is a strong peak at the cusp z-positions. In the downscaled version, however, there are already significant fluxes towards the wall before the cusp position (seen from the anode). This is apparently due to the relatively strong radial diffusion. It becomes apparent that the relatively weak magnetic field has consequences for the magnetic confinement. Electrons are lost to the wall downstream of the cusp which in the unscaled version would undergo more

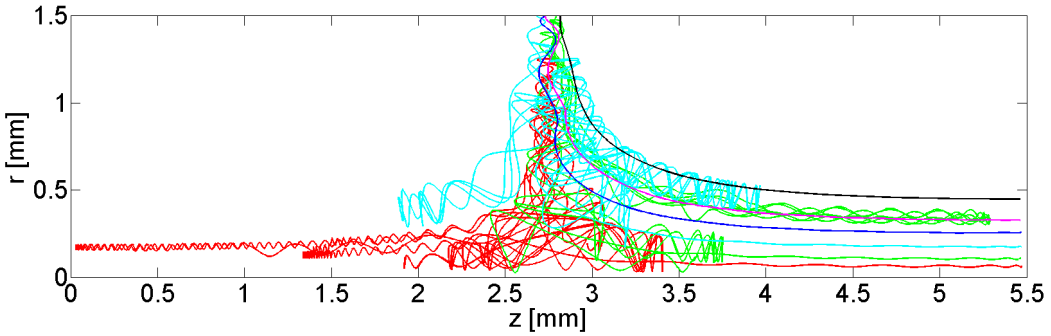

Figure 6.7: Traces of source electrons inside a HEMPT discharge channel section.

oscillations before lost to the wall only near the position of the cusp. Electrons can overcome the cusp due to a combination of the weak magnetic field at low radii at the cusps position and diffusion. Because this is possible mostly for electrons that start at low radii, as can be seen in Fig. 6.7, upstream of the cusp, they form a high-density region which is more focused towards lower radii. The peak density is lower than the one in the downstream region. These areas are more similar to each other in both models. However, in the downscaled version it still appears to be more diffuse than in the unscaled one.

In general, it can be concluded that the smaller system is more wall-dominated due to the relative strong radial diffusion.

The spatial ion distribution is very similar to that of the electrons, as one can recognize in Fig. 6.8 a, b. In principle, this is also expected due to the quasi-neutrality of the plasma. The ion distribution is clearly influenced by the magnetic field, despite that the ions are not significantly affected by the magnetic field within a device of this size. The explanation is that the electrons mediate the effect of the magnetic field to the ions. In an unmagnetized plasma, due to their higher mass, the ions are not significantly influenced by the electrons. While the electrons migrate perpendicular to the magnetic field lines, their mobility into that direction is rather low. This outweighs the low inertia of the ions. Therefore, the magnetic field topology is already sufficient to control the spatial distribution of the plasma as a whole, not just the electrons.

In both cases, the electric potential is almost uniform at a few volts above the anode potential. Apparently, the mobility in the axial direction of electrons near the z-axis is sufficient to mediate the anode potential throughout most of the plasma volume. The gap of a few volt towards the anode potential is the plasma potential. The dielectric wall of the discharge chamber charges up to the local floating potential, which is again a few volts below the local plasma potential. There is, however, a significant dip in the potential at the cusp po-

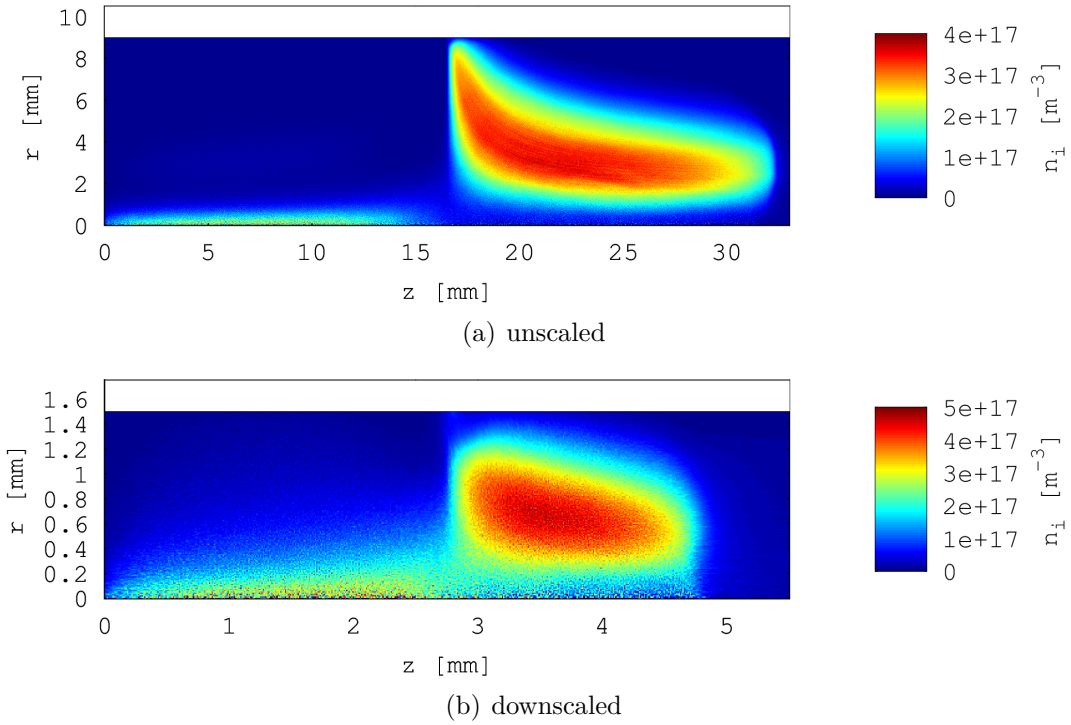

(a) unscaled

(b) downscaled

Figure 6.8: Ion density profile of a HEMPT discharge channel section.

sition in the downscaled version. In the unscaled version this dip is much less prominent and less deep. The deeper dip in the potential of the downscaled version indicates electrons of higher energy impacting the dielectric surface.

As mentioned before, in the downscaled version, downstream of the cusp, more electrons are at larger radii than it is the case for its unscaled counterpart, relatively seen. Also as previously mentioned, electrons at smaller radii can overcome the cusp easier than ones at higher radii. Consequently, the average capability of electrons to overcome the cusp is reduced for the downscaled version. This higher resistance towards axial mobility creates the larger axial potential drop.

The electron source (cathode), the wall losses and the anode current can be compared to each other. As mentioned for the setup, the source strength I_{source} is set to 0.25 mA for the downscaled version, and, according to the scaling law, to $I_{source} = 1.5$ mA for the unscaled version. The wall losses I_{wall} are 0.26 mA in the downscaled case and $I_{wall} = 3.30$ mA in the unscaled one. The anode current is $I_{anode} = 0.40$ mA for downscaled and $I_{anode} = 4.05$ mA for unscaled case. To compare the two models it is obviously best to work with ratios. The downscaled model has an anode to source current ratio of $I_{anode}/I_{source} = 1.6$, while for the unscaled it is 2.7. This higher ratio indicates a significantly higher

relative ionization efficiency for the unscaled version. The ratio of wall losses to anode current I_{wall}/I_{anode} is 0.65 in the downscaled case and 0.81 in the unscaled case. Counter-intuitively, the downscaled case has a slightly better wall loss ratio.

The magnetic mirror effect of the cusp plays a significant role in the magnetic confinement. This magnetic mirror effect is not depending on the absolute values but from the relative changes in the flux density. These changes remain the same since the magnetic field topology was not modified for the downscaled case. Therefore, the only significant change is the increased wall loss downstream of the cusp due to increased radial diffusion in the downscaled version. These wall losses, however, consist mainly of high-energy electrons, since they come directly from the potential drop and impact on the wall with little opportunity to experience ionizing collisions, as can also be seen in Fig. 6.7. They are mainly lost to the ionization process which explains the lower ionization efficiency for the downscaled version.

A significant difference between the scaling test in the previous chapter is that the source electrons are concentrated towards smaller radii. It can be concluded that this fact makes the HEMPT discharge chambers plasma less dependent on the lower magnetic confinement which occurs in the downscaled configuration. This concentration happens near the thrusters exit, whose conditions were approximated here. Therefore, a similar principle can be expected to be found for the thruster simulations in the following chapters.

7 Simulation of a downscaled HEMPT

7.1 Setup including the magnets assembly

The reference for all further computer models will be a simulation of a version for a downscaled HEMPT that is thoroughly tested [73]. It had a stable operation with a thrust of about 40 μN, which was one of the lowest values that could be achieved during the test campaign. The operational conditions were neutral gas flow of 0.27 sccm and a fixed anode potential of 400 V. The measured anode current was 4.5 mA. The thrusters discharge chamber has a length of 14 mm and a radius of 1.5 mm.

The simulation domain represents a cylindrical volume with a length of $Z = 19.12$ mm and a radius of $R = 5.12$ mm (Fig. 7.1). Like in the previous chapters, the simulation is two-dimensional in a r-z-plane of a cylindrical coordinate system. The additional length compared to the discharge chamber allows for the thrusters exit plume to be modeled. Deviations from the real plume are expected due to the proximity of the domain boundaries, which effect the near electrostatic field. Neumann boundaries were considered, but due to their mathematical definition they could not be applied to two boundaries that are perpendicular to each other. Applying a Neumann condition to only one of them would create an asymmetry. The effect of which is difficult to evaluate. Applying a Dirichlet condition to both boundaries keeps the disturbance as symmetric as possible. Therefore by use of Dirichlet condition, the boundary at $z = 19.12$ mm in the range 0 mm $\leq r \leq 5.12$ mm is set at ground potential, which is defined as 0 V. The same is the case for the boundary at $r = 5.12$ mm in the range 14 mm $\leq z \leq 19.12$ mm. The element that defines the thrusters discharge chamber is a tube made out of the dielectric material Al_2O_3 with an inner radius of 1.5 mm and a thickness of 1 mm. To incorporate this ceramic tube into the simulation, surface charge accumulation is accounted for at $r = 1.5$ mm along 0 mm $\leq z \leq 14$ mm and at $z = 14$ mm along 1.5 mm $\leq r \leq 2.5$ mm. Also, the dielectric permittivity of the material of $\epsilon_r = 9$ is set in the area 0 mm $\leq z \leq 14$ mm, 1.5 mm $\leq r \leq 2.5$ mm. At $r = 2.5$ mm is the inner radius of the permanent magnets setup. Its outer radius is beyond the simulation domains. This is not a concern since its magnetic field is simulated by a finite element method with a sufficient domain size. The region

which is included in the thruster simulation domain is 0 mm $\leq z \leq$ 14 mm, 2.5 mm $\leq r \leq$ 5.12 mm. Since these regions represent metallic parts who are grounded, there the potential is set to 0 V. The boundary $r = 0$ mm, 0 mm $\leq z \leq$ 19.12 mm is the symmetry axis of the simulation domain. Therefore, a Neumann boundary condition of no radial electric field is applied here, as it must be the case for the symmetry axis of a cylinder coordinate system. The only remaining boundary section that is not defined is at $z = 0$ mm, 0 mm $\leq r \leq$ 2.5 mm. For simplicity, the remaining boundary segment is set to anode potential, even though the anode ends at $r = 1.5$ mm. Previous simulations, both from Hall- and HEMP thrusters, have shown that near the anode the dielectric surface attains almost exactly the anode potential. This is subsequent due to the floating surface with regards to the local plasma potential, whereas the anode potential acts as the floating potential of this plasma. Hence, this boundary condition should not cause noticeable deviations. Additionally, once the steady state is reached, potentials behind the dielectric surface are electrostatically shielded by the surface charge.

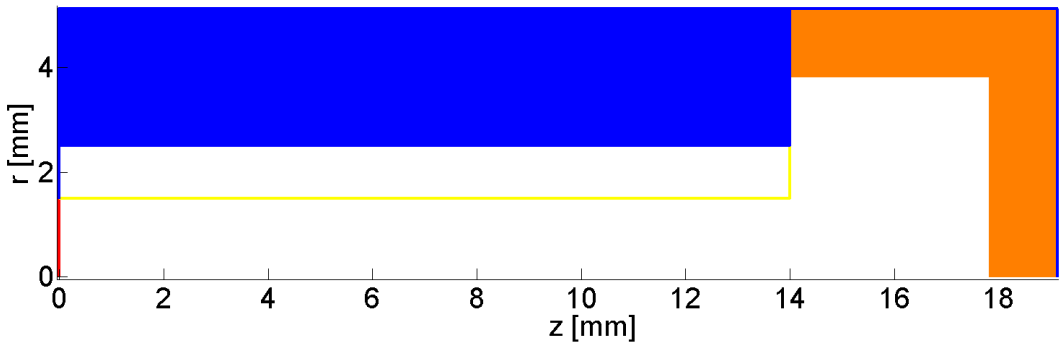

Figure 7.1: Micro-HEMPT simulation domain: ground potential (blue), anode potential (red), dielectric surface (yellow), electron source (orange).

The permanent magnets setup consists of three magnetic rings and five distance rings. All five distance rings focus and, therefore, strengthen the flux density at the magnetic cusps. The magnetic and distance rings thickness in the z-direction, the outer radius and the materials are all the same as in the previous chapter since they are based on the same micro-HEMPT model. As mentioned before, here the rings inner radius is 2.5 mm. A 0.25 mm thick dielectric and resulting inner radius of 1.75 mm will be used again in the follow-up simulation. The length of this setup is 18 mm. The anode surface is placed halfway at the first magnet, resulting in a length of the main part of the discharge chamber of 14 mm. The static magnetic field is calculated in the same manner as in the previous chapter. The simulation domain ranges from $z = -37.5$ mm to $z = 48.5$ mm and $r = 0$ mm to $r = 50.0$ mm. The resulting magnetic flux density has for the most part an axial direction with a maximum

of about 0.7 T (Fig. 7.2). Along the z-axis both the axial and the radial flux drops to zero around the z-position of the distance rings. This can be defined as being the z-positions of the magnetic cusps. Such a zero-field-point occurs another time outside the thrusters exit at around $z = 16$ mm. At this position the magnetic field forms an exit cusp. The maximum radial flux within the discharge channel is at its wall near the cusps z-positions.

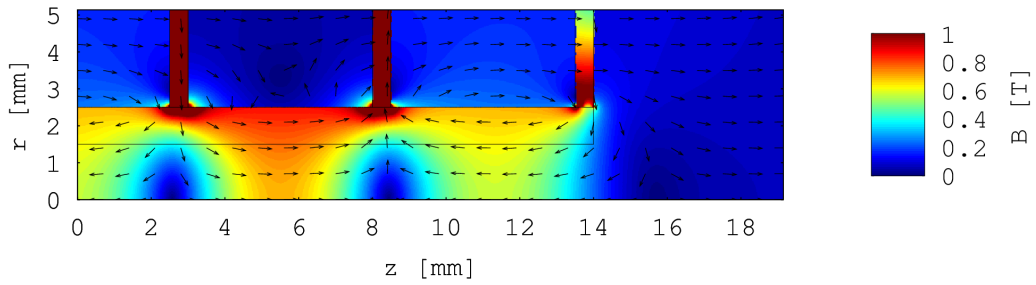

Figure 7.2: Micro-HEMPT magnetic flux density profile (for the design with 2.5 mm inner diameter of the ring magnets).

A design criteria of the micro-HEMPT is to keep the thrust generated by the neutral gas which is not ionized within the discharge chamber and leaves through the exit low. The reason for this goal is that neutral gas which leaves the thruster generates thrust, which interferes with the design goal of thrust and thrust noise being as low as possible.

Therefore a special neutral gas injector was designed which injects the neutral gas radially towards the discharge chamber walls. The end-cap of this injector serves as the anode surface. The neutral gas is thermalized upon wall impact and, thus, loses the momentum it gained from the pressure drop. This effect helps to reduce the axial momentum of the remaining neutral gas that leaves the thruster. This is confirmed by thrust measurements of the thruster running only with neutral gas without plasma ignition. In this case, the exhaust velocity calculated from the measurement is similar to the thermal velocity. This injector setup would be rather difficult to simulate since its surface boundaries are diagonals in the r-z plane, and the simulation grid could only approximate these by a stair-step pattern. Also due to the high density gradient, the overall particle count would be vast.

Since it is only of interest what the injector generates for the discharge chamber, a volume source for thermalized neutrals is implemented and the simulation domain begins at the z-position of the anode surface. In the radial direction, this source spreads over the gap between the anode and the discharge chambers inner radius. That is the radial distance from $r = 1.25$ mm to $r = 1.5$ mm. To avoiding an extremely high peak in density, the volume source is spread

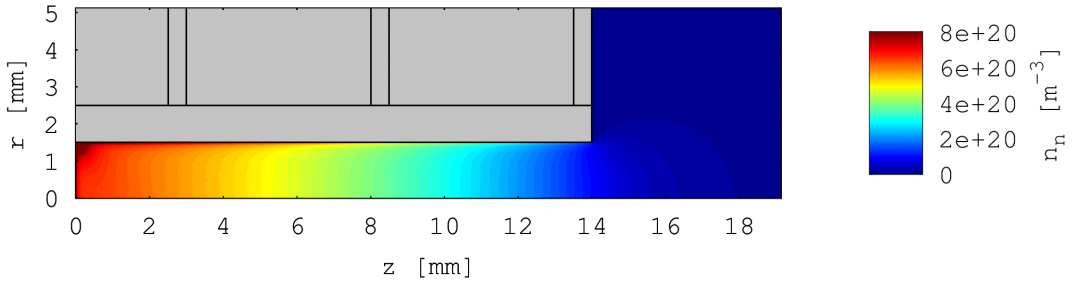

Figure 7.3: Micro-HEMPT neutral gas density profile for a 0.27 sccm source.

out from $z = 0$ mm to $z = 0.25$ mm. An additional correction is then made to keep the volume source one grid cell length apart from both the anode and the chamber surface (to avoid the unlikely event of a neutral particle being created directly on the surface). The final boundaries for the source are then $z = 0.02$ mm to $z = 0.25$ mm and $r = 1.27$ mm to $r = 1.5$ mm. The generated neutral particles have thermal velocity, but no drift velocity. Their velocities are Maxwell distributed with a temperature of 500 K which is the estimated wall temperature. Since in reality the neutrals already had wall contact due to the injector setup, they are initiated with this temperature. The neutrals collide with the anode and chamber wall and spread out over the entire chamber until they leave through the thrusters exit. The walls are set to be diffusively reflective which yields a gas exit velocity that is in good agreement with the neutral thrust measurement. Over the length of the discharge channel the density drops from about $6 \cdot 10^{20}$ m^{-3} to about $1 \cdot 10^{20}$ m^{-3}, when neglecting the still significant peak of the volume source (Fig. 7.3). As expected, along the length of the channel the thermal velocity is transferred to a directed velocity, which is about 300 m/s. The angular distribution at some distance from the thrusters exit is rather uniform from 0 degrees to 90 degrees, with 0 degrees being the azial direction and 90 degrees being the radial direction.

Both the results of the magnetic field calculation and the steady state of the neutral simulation are incorporated in the plasma model. Their values are spatially dependent, but static in time. For the magnetic field, this is justified by the field of permanent magnets obviously not varying in time. Only the magnetic field generated by the plasma currents is fluctuating. As shown in chapter 3.1, the flux density of these fields is in the order of magnitude of $1 \cdot 10^{-7}$ T. Therefore, its contribution to the overall field is negligible. From the anode current measured in the experiments it can be calculated that only 25 % of the neutral gas have been ionized leaving the thruster. This is the result of a neutral gas inflow of 0.27 sccm, and the anode current of 4.5 mA, translating to $1.1 \cdot 10^{17}$ neutrals per second and $2.5 \cdot 10^{16}$ electrons per second.

It is assumed that the ion beam current is similar to the anode current. The ion

beam current does not reflect the entire ionization rate. Ions that are not part of this beam impact on the discharge chamber wall, where they are 'recycled' as neutrals. Therefore, the anode current approximately reflects the number of neutral particles that are 'lost' due to ionization.

Since it is only about 25 %, the reduction in the neutral gas density is neglected with an error which is assumed to be acceptable. Due to the high particle count of the neutrals, using their density per cell in the Monte Carlo code instead individual particles reduces the calculation time. Moreover, this method reduces high memory usage which would make parallel processing less efficient.

In the experimental setup, the neutralizer was made of tungsten wires of three small lightning bulbs, providing several mA of electron current. Their position was about $r = 40$ mm, $z = 0$ mm measured from the thrusters exit. Strictly following the magnetic field lines the electrons would impact the thrusters housing at around $r = 20$ mm instead of reaching the thrusters exit. This is apparently not the case, since without the neutralizer electrons the thruster could not operate. The magnetic field near the neutralizer is rather weak, presumably leading to a rather diffusive behavior of the electrons, which would explain why they can reach the thruster. This would mean that the electrons are rather uniform distributed in the proximity of the thruster. It is only this proximity that is included in the simulation domain, that is 5.12 mm times 5.12 mm in r- and z-direction, again measured from the z-position of the thrusters exit. As an approximation uniform electron sources are applied near the outer rim of the simulation domain. They are somewhat spread out over an area instead of being exactly at the rims. These rims are 14 mm $\leq z \leq$ 19.12 mm at $r = 5.12$ mm, and 0 mm $\leq r \leq$ 5.12 mm at $z = 19.12$ mm. Here $z = 0$ is the anode position, e.g. the origin point of this simulation domain. The precise areas are 17.84 mm $\leq z \leq$ 19.12 mm, 0 mm $\leq r \leq 3,84$ mm and 14 mm $\leq z \leq$ 19.12 mm, 3.84 mm $\leq r \leq$ 5.12 mm.

The estimated maximum plasma density in steady state is $1 \cdot 10^{19}$ m^{-3}. The system is scaled down by factor 8 to save computational time. The maximum plasma density in the downscaled system is then subsequently $8 \cdot 10^{19}$ m^{-3}. The estimated average electron temperature is 10 eV and should remain the same according to the scaling laws (chapter 4.3). The minimum Debye length is $\lambda_{De} = 2.6 \cdot 10^{-6}$m in the downscaled system. In order to work with rough numbers for the grid cell size dr_0, the ratio to the Debye length, $dr = dr_0/\lambda_{DE}$ is set to 0.951692, giving $dr_0 = 2.5 \cdot 10^{-6}$m. Also for $dr < 1$, it is ensured that the Debye length is always larger than the grid size and, therefore, the Debye length is resolved by the simulation grid. The maximum plasma frequency results from the maximum electron density and is $\omega_P = 5 \cdot 10^{11}$ 1/s.

Its period time length is then $2 \cdot 10^{-12}$ s. To ensure that this oscillation is properly resolved, the time step size is set to be a fifth of this period, that is $dt_0 = 4 \cdot 10^{13}$ s. The mean magnetic field strength in the discharge chamber is about $B = 0.6$ T in the unscaled system. For the scaled system it is consequently about 4.8 T. The gyration frequency is, therefore, $1.34 \cdot 10^{11}$ 1/s, and its period $7.44 \cdot 10^{-12}$ s. This is significantly larger than the electron plasma oscillation, justifying this oscillation to be the determining factor for the time step size in this simulation setup. The maximum velocity of a particle without crossing more than one cell per time step is $v_{max} = dr_0/dt_0 = 6.25 \cdot 10^6$ m/s. This is equivalent to about 100 eV electrons. While the electrons could reach 400 eV due to the 400 V potential drop, previous simulations show that due to trapping in a ring current near the thrusters exit, only a few electrons reach more than 100 eV. Therefore, this time step size is assumed to be sufficient regarding the maximum electron speed in this thruster.

After several iterations the electron source strength was set to 17 mA (unscaled), in order to yield a simulated anode current (unscaled) which is close to the measured value. The electron source strength is scaled down by the scaling factor. Both the neutral gas density and magnetic flux strength is scaled up by the scaling factor, too (all as demanded by scaling laws). From now on, all input values and results will be given for the unscaled system. The calculations necessary are always linear according to the scaling law. These results need to be considered with care since some deviation in the behavior of the scaled system is possible due to the relative change in plasma sheath size to system size (chapter 5.4).

A deviation that is obvious in advance of a DM3a-like thruster and the micro-HEMPT simulation is the different relation of electron gyration radii and system size. The question arises whether in the micro-HEMPT the gyration radii becomes a significant portion of the system size and, therefore, directly leads to surface losses. As noted before the mean magnetic flux density inside the discharge channel is 0.6 T. For a 12.5 eV electron, which is the first ionization energy of xenon and also close to the estimated average energy of 10 eV, the gyration radius 0.02 mm. This is only about 1 % of the discharge channel radius. Therefore, it can be assumed that most of the wall collisions of the electrons are not a direct consequence of their gyration motion.

The gyration radius is also a factor in estimating whether the electrons can overcome the magnetic cusps. Near these cusps z-positions, near $r = 0$ mm, the flux approaches zero and, therefore, the gyration radii approach infinite, enabling some electrons that come close to this 'zero point' to overcome the cusp (Fig. 7.2). At the exit cusp outside the channel the flux is also low (e.g. 0.05 T at $z = 17$ mm, $r = 0$ mm) enabling electrons to overcome this cusp and

enter the discharge channel. While the cusps play a major role in the magnetic confinement, it is necessary that electrons can finally overcome the cusp. Otherwise, there would be no electron flow towards the anode and, consequently, the thruster would not operate.

Diffusion due to collisions of the electrons with neutral atoms and the anomalous diffusion also takes a major role in the electrons overcoming the cusps.

At $2{\cdot}10^{20}$ m^{-3}, which is about the mean neutral gas density inside the discharge channel, the ionization mean free path for an electron at 12.5 eV is 4.76 m. At 100 eV, which is about the energy for the maximum of the ionization cross section [58], the mean free path becomes 0.086 m, which is still several times larger than the discharge channel length (0.014 m). This shows the necessity of magnetic confinement.

Additional to the collisions in the previous simulations, this model also implements ones that generate double charged ions. The reactions are Xe + e => Xe^{2+} + e + e + e and Xe^{+} + e => Xe^{2+} + e + e (Xe, Xe^{+}, Xe^{2+}: neutral, ionized, double ionized xenon. e: electron).

As described before (chapter 2.9), the model includes anomalous diffusion caused by the azimuthal electric fields from 3D fluctuations. Because it being only a 2D model in the r-z-plane, these azimuthal fields are not included in this simulation. The applied diffusion coefficient of $D = 0.4k_BT_e/eB$ is derived from a 3D simulation of a similar thruster model. The description by a diffusion coefficient is only suited for the macroscopic description in a fluid model and cannot be applied directly to the treatment of individual particles. Therefore, the velocity of the particle vectors is rotated, which causes their center of gyration to shift. Changes parallel to the local magnetic field direction are neglected to ensure that the speed of the electrons along the magnetic field lines does not alter. A random generator selects electrons on which this procedure is applied, based on the diffusion coefficients. The larger the coefficient the more electrons are selected. The variable within the coefficient is the local magnetic flux density. This means that the electron have a diffusive behavior perpendicular to the magnetic field lines which is dependent on the flux density B.

The basic goal for the simulation of the plasma properties is to be in steady state, as it is the case for a continuously running thruster. Hence, the plasma ignition process is not of interest. Also the timescale of this process is probably beyond what can be done in a reasonable amount of computation time, as long as it needs to be calculated in time steps of the electron timescale. Fluid simulations working on much larger timescales can perform such feats.

For a relatively fast achievement of steady state, a significant amount of ions and electrons is inserted into the discharge channel and, beyond, till the right boundary of the domain. This forms a plasma column. The extension to the right is to speed up the formation of the near field plume region. The electric field from the positive potential of this region is essential for electrons originating from the source outside the thruster to overcome the exit cusp and enter the discharge channel. For this initial column, the particle density in the r-z-plane is set to be uniform, in order to have a higher plasma density at lower radii (chapter 3.5). This represents a closer approach towards the plasma distribution known from the DM3a thruster than starting with a uniform plasma distribution. Near the z-axis, the plasma quickly reaches a potential close to the anode potential (Fig. 7.4). This can directly be explained by the high mobility of the electrons along the z-axis due to the axial magnetic field. Over time this potential spreads out towards higher radii and, finally, the dielectric surface charges up to a similar value due to ions and electrons impacting on it. While this is not necessarily the real sequence of events during thruster ignition, it shows the importance of the electron mobility for the plasma behavior.

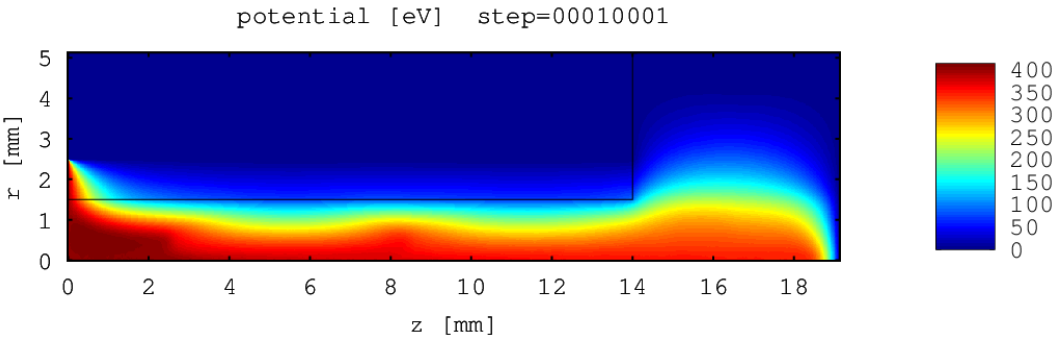

Figure 7.4: Potential profile after 10000 time steps

7.2 Resulting properties of a downscaled HEMPT

If the steady state is reached, the plasma potential inside the discharge channel appears almost uniform, as can be seen in Fig. 7.5 a). Only a spot on the anode potential, here from 380 V to 420 V, as shown in Fig. 7.5 b) makes variations in the potential clearly visible. From the anode until the first cusp (downstream regarding the ion direction) the anode is the floating potential of the plasma. The plasma potential being about 5 V higher than the floating potential appears reasonable for the estimated electron temperatures. Behind the first cusp inside the discharge channel the potential drops by about 10 V, behind the second about another 5 V. The dielectric surface can be thought of

as divided into many sections (in this case of the size of the grid cells) which are each floating with regards to the local plasma potential. Between the cusps this surface potential roughly follows the plasma potential drops. Near the cusps position, close to the dielectric surface, there is a dip in the potential of several 10 V. This is much more than the drops from a region in front of a cusp to behind. All these observations can be explained by the influence of the magnetic field on the electrons mobility. The to a large degree radial magnetic field near the cusp hinders the electrons movement in axial direction, while the ions can pass freely in this direction. This creates the potential drops that dominate the plasma volume. Also this radial field enables a much higher mobility of the electrons towards the surface (radial direction) than it is the case between the cusps. Furthermore, the shape of the field lines focuses the electrons towards a small surface area. These two effects cause the strong surface charge at the cusps positions that is negative relative to most of the plasma potential inside the discharge channel. While these surface charges are local, they affect the plasma potential non-locally due to the Poisson equation. This net charge reduces the plasma potential over a significant distance and is a deviation to the commonly uniform potential within the discharge channel. The second dip being smaller than the first one can be explained by a closer distance to the thrusters exit.

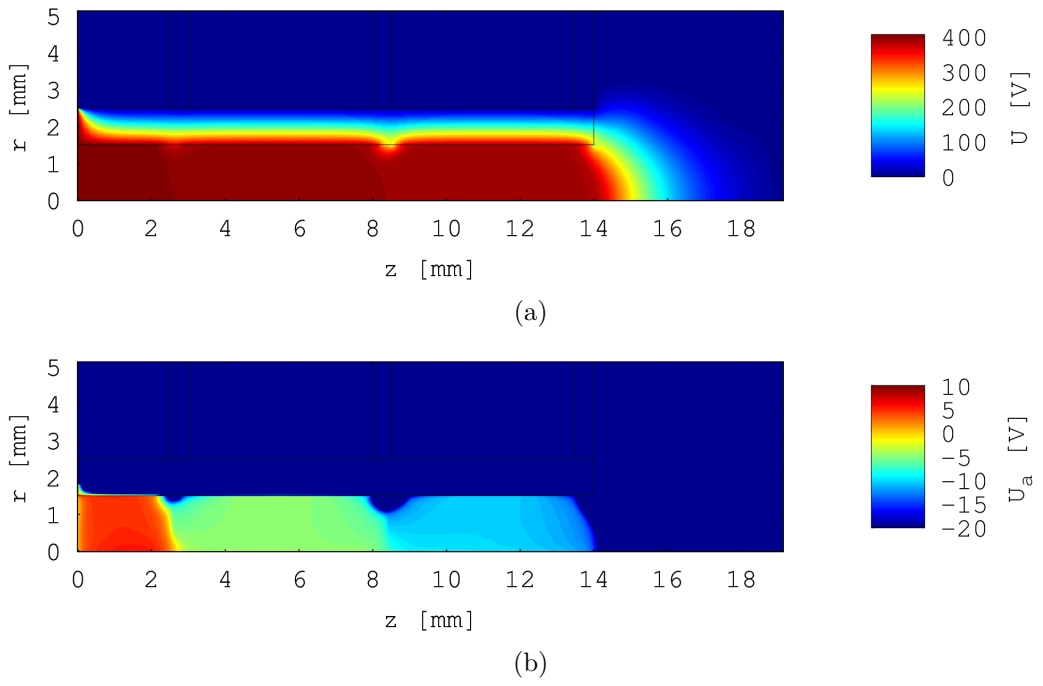

Figure 7.5: Potential profile for the complete range a), and from 380 V to 420 V b) (for the design with 2.5 mm inner diameter of the ring magnets, U_a = potential relative to 400 V).

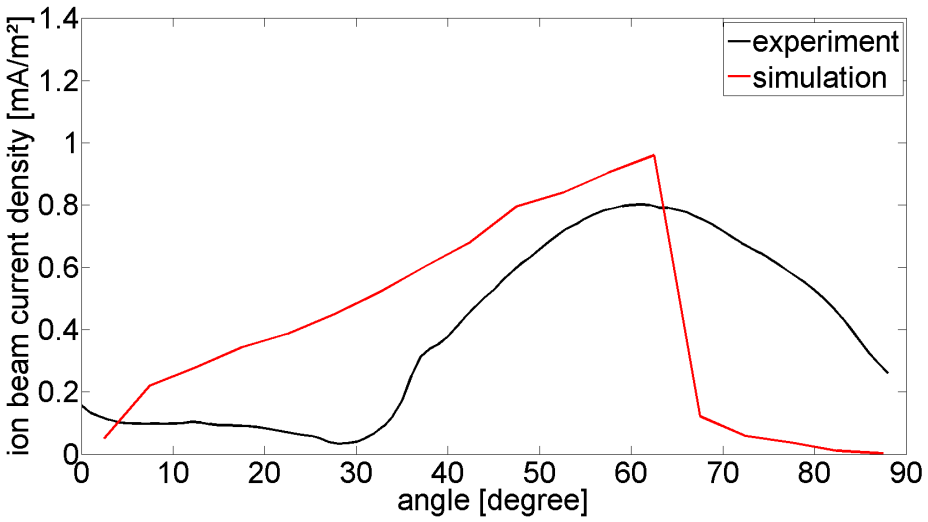

Figure 7.6: Micro-HEMPT ion beam angular distribution.

Near the thrusters exit the main potential drop is located where the electrons which originate from the external source (neutralizer) gain most of their energy. This high kinetic energy in turn causes them to have larger gyration radii (chapter 2.3) which makes it easier for them to overcome the cusps. Therefore, the difference in axial mobility between the electrons and ions is lower compared to the case where the electrons have lower energy. At the first cusp a considerable amount of the electrons has dissipated into the ionization process leading to a larger potential drop. The main potential drop forms a 'bulge' reaching beyond the positive 'anchor' of the positively charged dielectric. This 'bulge' obliquely accelerates the ions away from the symmetry axis. The precise angular distribution of their current density and velocity is of particular interest since the thrust force of the thruster can be calculated by these quantities. The thrust has also been measured in the experimental setup. For that purpose, on a 40 cm long arm Faraday cups were moved around the thrusters exit. In the simulation, the grid cells at the outer rim of the thrusters exterior region are used to determine the ion beam. These are the cells along the lines $z = 19.12$ mm, 0 mm $\leq r \leq 5.12$ mm and $r = 5.12$ mm, 1.4 mm $\leq z \leq 19.12$ mm. The super-ions per time crossing these cells yield the ion current at the position of the individual cell. The corresponding angle is measured by defining a line from the thruster exit z-position (here: $z = 14$ mm) at $r = 0$ mm to the cell position and calculating the angle towards the thruster symmetry axis. Then the angular dependent ion currents from both the simulation and the measurement can be compared directly. In both cases, the maximum is at higher angles at about 60 degrees in the experiment and in the simulation (Fig. 7.6). In the simulation, the ion current at lower angles is relatively large compared to the experiment, but still significantly lower than the maxi-

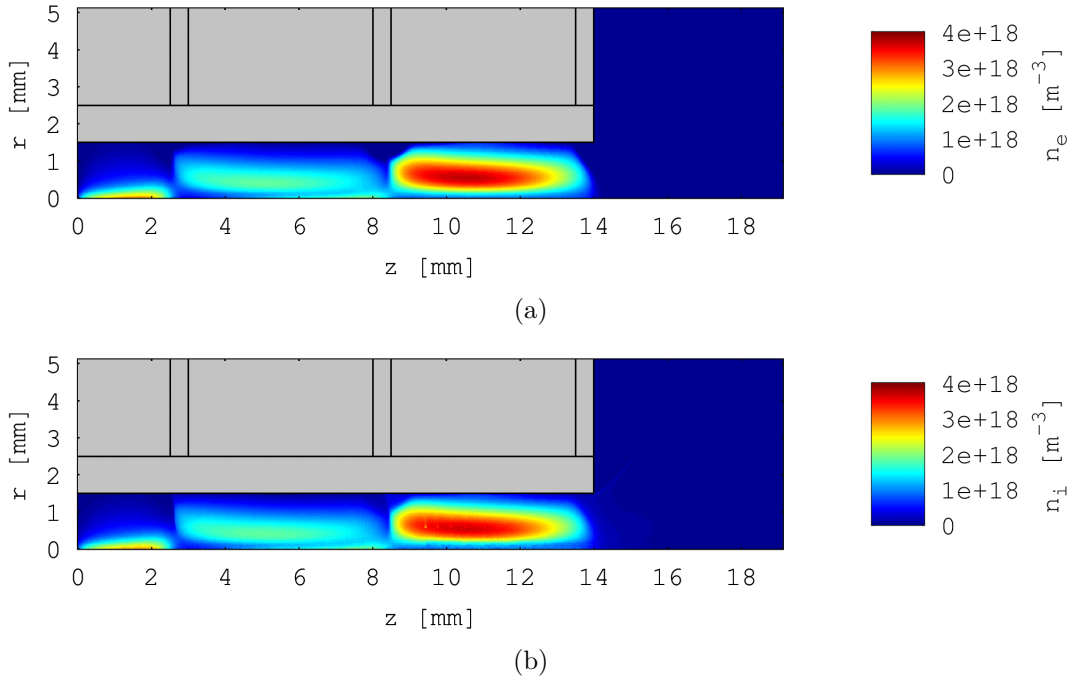

Figure 7.7: Denstiy profile of a) electrons and b) ions (for the design with 2.5 mm inner diameter of the ring magnets).

mum. Deviations from the experiment are expected since the relatively close boundary of the simulation domain with its ground potential is a strong artificial influence. Compared to that, the grounded potential of the experiment is the vacuum vessels interior surface which can be assumed in infinite distance compared to the size of a downscaled HEMPT. Also due to the self-similarity scaling used to save computation time the overall number of charged particles is lower, which causes the 'bulk' of the electric potential at the thruster exit to be less prominent. This appears to be a reasonable explanation for a larger fraction of the ion beam present at lower angles in the simulation. In principle, the hollow cone typical for HEMPTs is recreated in the simulation by having a maximum in the ion beam strength at high angles. The ion currents through the individual cells can be summed up to the total current which is 2.5 mA. This is somewhat lower than the value from the experiment which is 3.1 mA. The deviation again might be contributed to the self-similarity scaling. With the bulk being smaller also less of the high-density plasma is located beyond the thrusters exit, where it could be accelerated outwards at a high rate. The anode current can be calculated by counting the electrons that go through the cells at the anode position, that is the line $z = 0$ mm, 0 mm $\leq r \leq 1.5$ mm. The sum is 4.7 mA and in the experiment it is 4.5 mA.

The spatial electron density is shown in Fig. 7.7 a). Its spatial distribution is heavily influenced by the magnetic field structure. It is clearly divided into

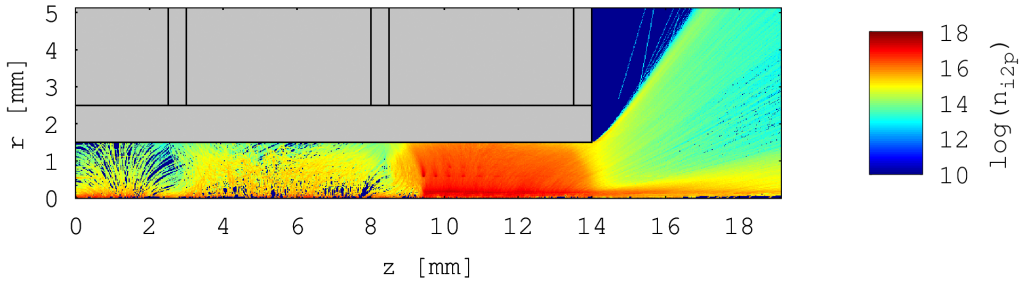

Figure 7.8: Denstiy profile double charged ions (for the design with 2.5 mm inner diameter of the ring magnets).

sections, sharply divided by the magnetic cusps. At the first section at the thrusters exit the maximum is at medium radius, apparently due to diffusion towards the walls. With each section closer to the anode the electrons become more focused towards the thrusters symmetry axis. This appears to be the consequence of electrons near the symmetry axis overcoming the cusps easier than those at larger radius, as shown in chapter 6, Fig. 6.7.

The ion density shown in 7.7 b) is very similar to the electron density. In a non-magnetized plasma the ions have a much lower mobility than the electrons due to their higher mass, while the same electric force acts upon single charged ions than on electrons. Here, the electron mobility is strongly reduced perpendicular to the magnetic field. The ion distribution being similar to the electron distribution proves that this is sufficient for the electrons to become the determining factor. Therefore, the plasma in this device can be controlled by confinement only of the electrons. Consequently, the magnetic field topology needs to be a big part of the considerations to make this thruster more efficient. The only major deviation between the ion and electron density is directly beyond the thrusters exit. There the ion density is significantly higher than the electron density. This difference generates the positive ‘bulge’ that can be seen in the potential. The potential drop of that ‘bulge’ is mainly along the magnetic field lines, perpendicular to the direction where the electrons have low mobility. There, the electrons are mainly confined by the magnetic field, whereas the ions pass unhindered. This effect generates the difference in density of the two species.

The density profile of the double charged ions is shown in Fig. 7.8. Their density is by far the highest in the discharge channel region that is closest to the exit, to such a degree that a logarithmic plot representation needs to be used to show the distribution in the other regions. This is to be expected, since double ionization occurs stronger due to high energy electrons than it is the case with single ionization. The electrons have their highest energies close to the thrusters exit.

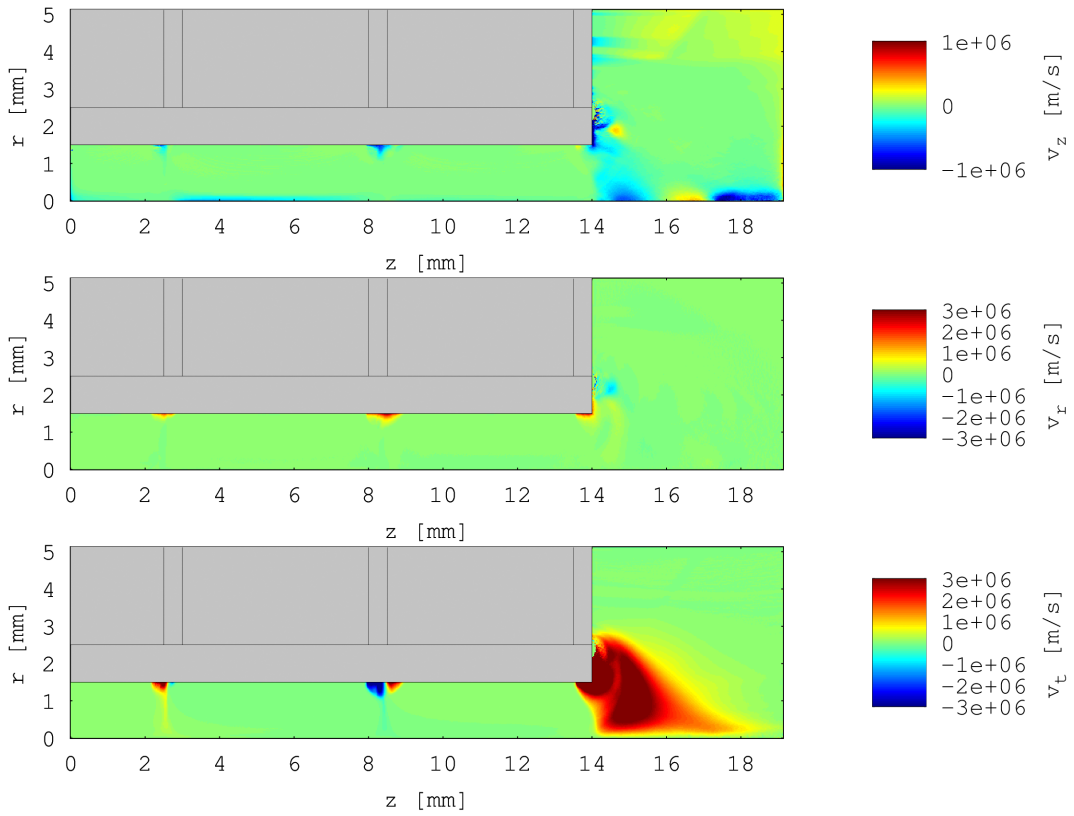

Figure 7.9: Axial, radial and azimuthal electron velocity profiles (upper, middle and lower picture; for the design with 2.5 mm inner diameter of the ring magnets).

The axial, radial and azimuthal velocities of the electrons can be seen in Fig. 7.9 a), b), c). The radial velocity shows the electrons movement towards the surface at the cusps position. The azimuthal velocity also shows some minor ring currents at these positions. The electric fields and magnetic fields are not perfectly parallel to each other in these regions, which is sufficient to generate this type of currents by $\boldsymbol{E} \times \boldsymbol{B}$ drift. The most prominent ring-current is at the thrusters exit. It is caused by crossing of the electric field lines of the potential drop of the 'bulge' and the magnetic field lines of the exit cusps.

This ring current contains high energy electrons of about 100 eV as can be recognized in Fig. 7.10. These are source electrons which gain their energy from the potential drop. They are kept in the ring current for a prolonged period of time before they enter the thruster due to normal and anomalous diffusion. In the ring current they already undergo ionizing collisions with the neutral gas leaving the thruster. This is the beginning of the avalanche effect which results in the anode and wall currents. These currents originate from

the relatively small current which enters the thruster.

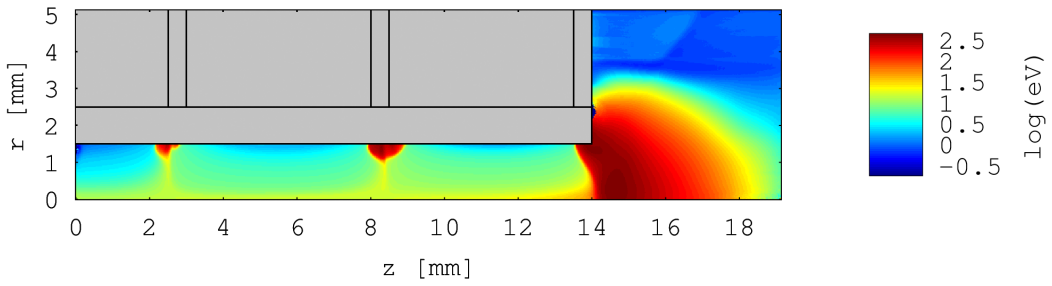

Figure 7.10: Micro-HEMPT electron energy (for the design with 2.5 mm inner diameter of the ring magnets).

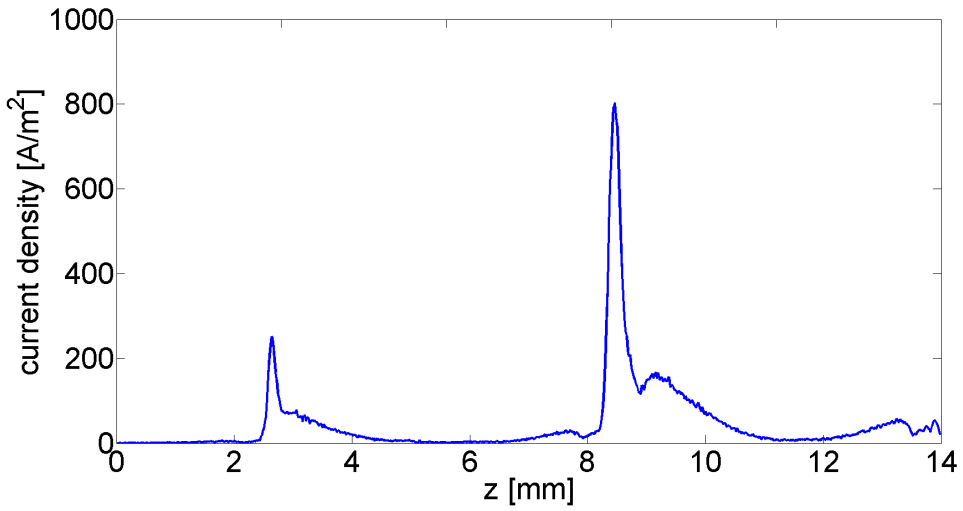

Figure 7.11: Micro-HEMPT ion flux at the channel wall (for the design with 2.5 mm inner diameter of the ring magnets).

Two small regions of high energy are near the surface at the cups position. These regions obviously have their cause in the energy the electrons gain in the drop between the bulk plasma potential to the relatively low surface potential at the cusp position. This kinetic energy is related to the radial and azimuthal velocity shown in the electrons velocity profiles. There exist also minor energy variations within the plasma bulk. Their gradient is mainly perpendicular to the magnetic field lines reflecting the low mobility of electrons in that direction.

A profile of the currents and energy fluxes of the ions towards the wall can be obtained by counting the absorbed ion-super-particles and the energy at the simulation grid cells that occupy these wall positions. The same procedure can be done for the electrons. The ions, however, are of more interest since

they cause material erosion due to sputtering (Fig. 7.11). Also in the steady state these fluxes must be the same, since neither electrons nor ions can move through the dielectric wall. Precisely, each ion is neutralized by an electron that reached the wall and cannot leave due to the potential gradient. As expected, the current density has two peaks at the cusp position, with a maximum of about 200 A/m^2 at the first cusp and about 800 A/m^2 at the second cusp. The energy also has its peaks at these positions with about 25 eV at the first cups and about 160 eV at the second cusp. This result validates the assumption that the electrons are higher energetic at the second cusp. From experimental values a sputter yield can be calculated. This is done for the second cusp since this is obviously the most critical region. For the ion energy at this position one gets an erosion of $2.97 \cdot 10^{-3}$ mm^3/C. With the current at this position given in C/s this results in an erosion of 0.684 mm over an operational time of 100 hours.

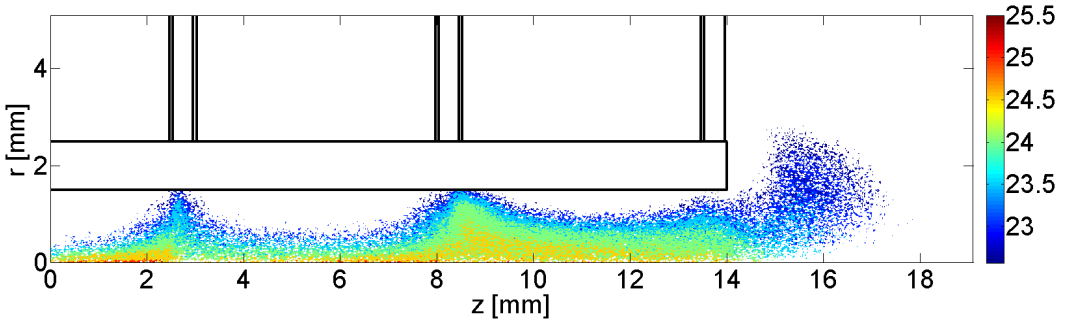

Figure 7.12: Micro-HEMPT ionization densities [log10(1/s·m^3)] (for the design with 2.5 mm inner diameter of the ring magnets).

The overall wall current is 6.1 mA. It gives a ratio from wall current to anode current of 1.3. This ratio will be necessary to estimate the plasma confinement and thruster performance. When the anode voltage is fixed, an increase in this ratio means that the wall losses are increased in relation to the thruster power consumption. It is a clear goal for the thruster development to keep the wall losses at a minimum, so that more ions that are generated by the ionization process leave the thruster and produce thrust.

The profile of the ionization is shown in Fig. 7.12. As expected, the ionization already begins outside the thruster in the proximity of its exit, caused by the high energy ring current. Inside the discharge channel, the ionization is focused towards smaller radii and becomes increasingly more focused with each cusp that is closer to the anode. This is apparently linked to the electron density whose focus increases in a similar manner. There is also strong ionization at the cusp position reaching towards larger radii, which concurs with the electrons of high energy in this region contributing partly to the ring currents at these positions.

Since practically no electrons can leave the thruster due to the steep potential drop at its exit, the overall ionization rate can be calculated from the sum of anode and wall current (4.8 mA + 3.8 mA). These are then each $6.74 \cdot 10^{16}$ electrons and ions per second. For comparison, the mass flow of 0.27 sccm corresponds to $1.1 \cdot 10^{17}$ neutrals per second. All ions that reach the wall, however, are 'recycled' as neutrals. Therefore only the value of the anode current, $(2.93 \cdot 10^{16})$ particles per second, contributes to the loss of neutral gas. It can be calculated that 27 % of the neutral gas is 'lost' due to ionization before it leaves the thruster. The number of neutrals compared to charged particles is, however, significantly higher, about 50 times. This obvious discrepancy is due to the neutrals moving significantly slower through the discharge channel than the ions.

8 Possible methods for improvement

8.1 Influence of the neutralizer

8.1.1 Experiment with an electron source focused on the thrusters axis

The simulation of HEMPT discharge sections in chapter 6 showed significant differences in the spatial plasma distribution. Nevertheless, the ratio of wall losses compared to anode current and source current did not change significantly for the downscaled version. Due to higher energy losses, however, the ionization efficiency is about half as low for the downscaled version, as derived from the anode current to source current ratio. Experiments showed that the DM3a HEMPT has an ionization efficiency of about 50 %, whereas for the micro-HEMPT it is about 25 %. A possibility to compensate the lower ionization efficiency might be to increase the fraction of the neutralizer electrons that enter the thruster discharge chamber. More source electrons inside the discharge chamber should directly cause an increase in ionization rate since these electrons gained the energy necessary for ionization (after passing through the potential drop). Furthermore, previous simulations [74] indicated that in a discharge chamber section source electrons being more focused towards smaller radii increase the ionization efficiency. Under these considerations, an experiment was designed that consisted of a neutralizer that emits electrons right in front of the thruster exit alongside its symmetry axis. The basic idea was that for electrons originating at smaller radii it is easier to overcome the exit cusp. With increasing number of electrons which reach the discharge chamber and focusing them the ionization rate should rise.

The experiment has been conducted by the use of an already existing setup of a facility at Airbus Friedrichshafen [73]. The main components of this setup are a vacuum chamber, a thrust balance, a thruster and an ion plume diagnostic of the thruster.

The neutralizer designed for this experiment consists of a housing which holds two ceramic tubes which run parallel to each other. These two tubes are bridged by a tungsten wire. This wire runs through these tubes and inside

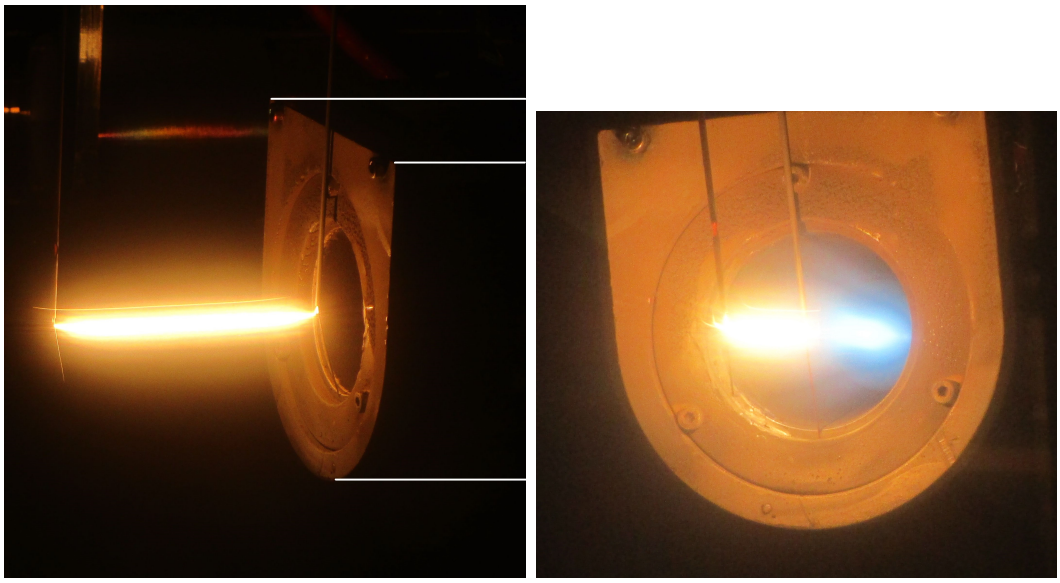

(a) side view (b) front view

Figure 8.1: The neutralizer oparating in front of the thruster.

the housing it is connected to low voltage cables which supply with electric current. The housing protects the connection between the wire and the cables from plasma particles, which would cause errors in voltage and current measurement. Once a sufficient current flows through the wire it starts glowing and emitting electrons. The bridge part, which is exposed, consequently emits electrons to its surrounding. This part can serve as a neutralizer. The whole neutralizer assembly was placed in front of the HEMP thruster that was at that time tested in Airbus Friedrichshafen (Fig. 8.1). The thruster was of conical design, similar to the version presented in [75], while the ones studied in this work are of cylindrical design. It is also somewhat larger and closer to the mN regime than the micro-HEMPT. Nevertheless, it was considered appropriate for a proof of concept. Both the thruster and the new neutralizer were placed inside a 1200 mm times 1200 mm times 880 mm vacuum chamber. Two entire sides of this chamber served as doors which enables good handling of the experimental setup. A setup which consisted of eight Faraday cups and one retarding potential analyzer (RPA) was also installed. Their purpose is to characterize the ion beam from an arbitrary thruster at certain angular resolution. The Faraday cups can measure the overall ion flux while the RPA can adjust the voltage on a grid and, thus, repel ions below a selected energy threshold. The setup is connected to the end of a 60 cm long mechanical arm and, thus, can be rotated 180 degrees of azimuthal angle around the thrusters exit. The Faraday cups are positioned over different heights to capture the elevation for about ± 40 degrees. The RPA is positioned at an elevation angle of 0.

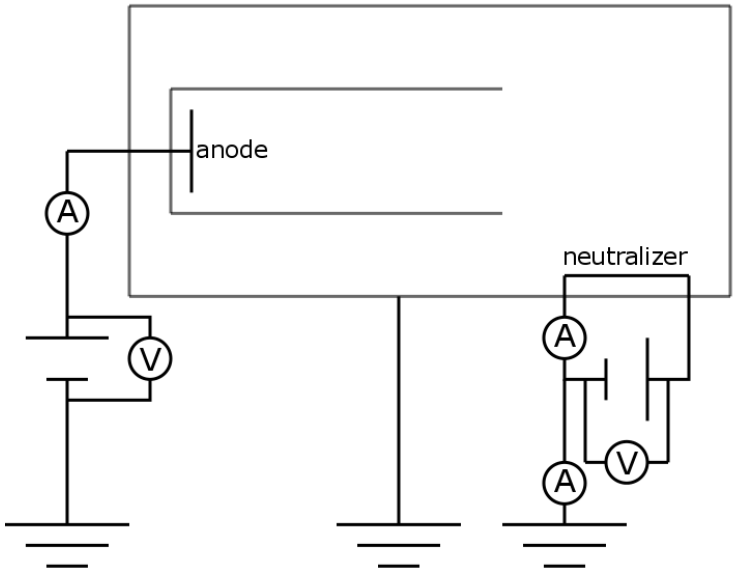

Figure 8.2: Circuit diagram of the experimental setup.

Since in this experiment only a rough estimate of the thruster performance was of interest, only the one RPA was used. The measured current was evaluated at a retarding voltage close to zero to measure the full ion current density. As typical for this experimental setup the thruster is connected to a thrust measurement balance. It could not be ruled out that the ceramic tube of the new neutralizer which is closer to the thruster generates an electrostatic force due to different surface potentials. This would disturb the thrust measurements. Therefore, the values from the balance were not evaluated. The power supplied to the thruster was monitored by an amperemeter and a voltmeter. The neutralizer was powered by its own electric circuit which also included an amperemeter and a voltmeter. The circuit of the thruster and the neutralizer were only indirectly connected via the ground (Fig. 8.2). The outflow of electrons from the neutralizer is measured by an additional amperemeter that shows the current to the ground. One forestage pump, two turbopumps and one cryopump evacuate the chamber to a base pressure in the order of magnitude of $1 \cdot 10^{-7}$ mbar. Under thruster operation the xenon gas from the thruster increases the pressure by about one order of magnitude.

For the experiment the wire bridge was placed as precise as possible along the thrusters symmetry axis with a closest distance of 14 mm from the thrusters exit. The chamber was evacuated and voltage to the thrusters and neutralizers circuit applied. A short burst of xenon gas flow was applied to ignite the thrusters plasma discharge. The constant xenon flow during the thrusters steady state operation was 2.6 sccm. For the thrusters circuit, the power sup-

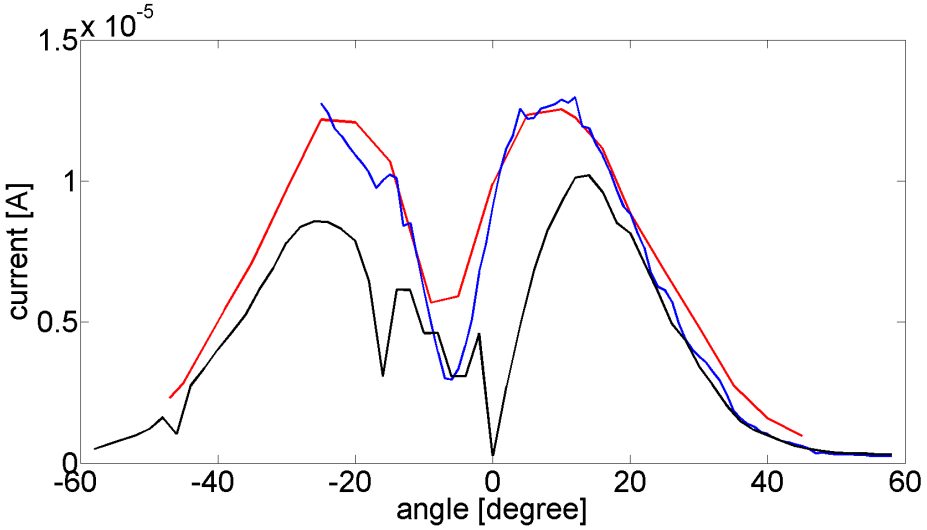

Figure 8.3: Measured maximum RPA ion current as function of angular position. Red: Light bulb neutralizer. Blue, black: Wire bridge neutralizer with 14 mm, 1 mm closest distance.

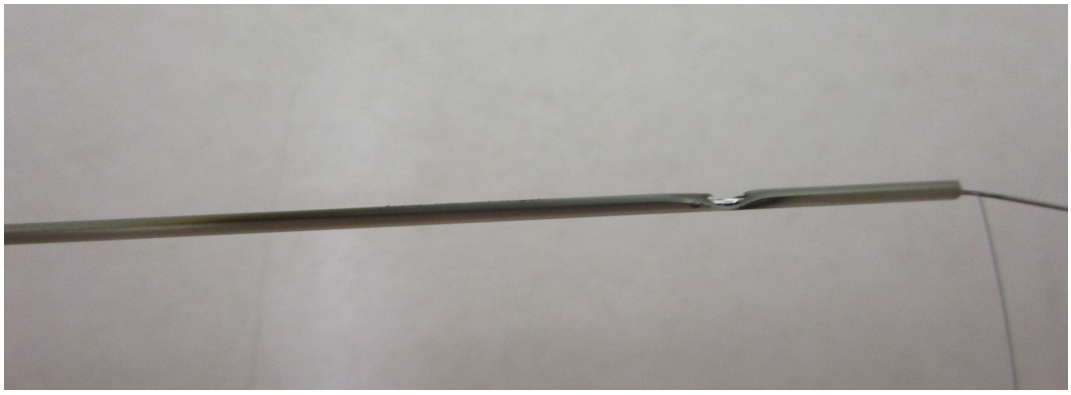

Figure 8.4: Erosion on the ceramic tube.

ply was set to a fixed voltage of 700 V. This is the voltage that was applied to the anode. An anode current of 120 mA was measured which is very similar to previous measurements with the same thruster operating parameters only with light bulb wires for a neutralizer instead. The neutralizer circuit in this experiment operated at 1.49 A and 18.99 V and emitted 0.32 mA which is also similar to the previous experiments. The results of the Faraday cup measurement against angular position is plotted in Fig. 8.3, both for this experiment and the previous one. Like for the anode current, the deviation is minor and appears to be of the same order of magnitude as the noise of the measurement. The results from the previous experiment are smoothed, while this experiment is presented as raw data. Both measurements represent the hollow cone that is typical for HEMPTs. In this case the ion beam maximum is at an angle of

about 25°. The only noticeable difference is a stronger drop in the ion beam intensity at around 0°. This is likely due to some kind of 'wind shadow' that the ceramic tubes produce in regards to the ion beam.

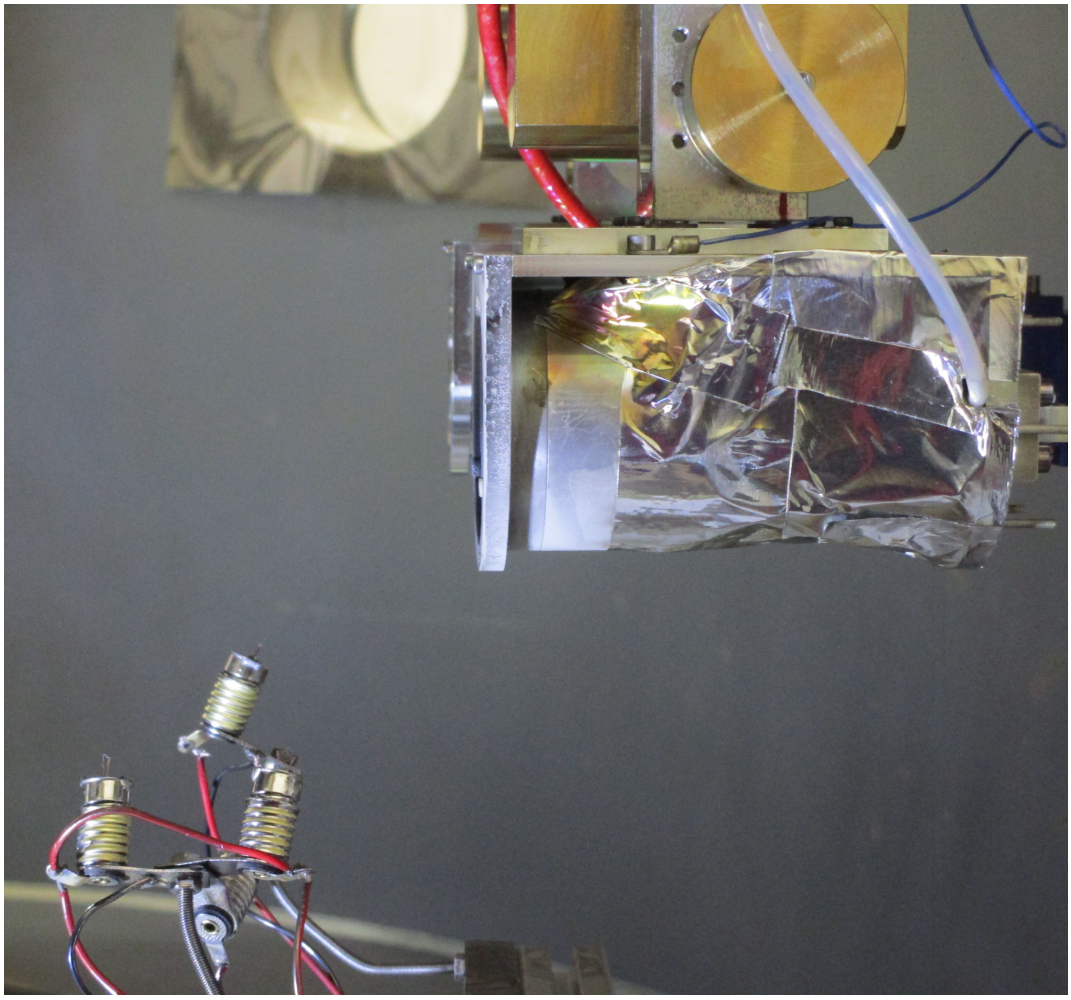

Figure 8.5: A neutralizer using lightbulb wires for electron glow emission (lower left).

It was not clear whether surface charge accumulation would cause a positive charge on the ceramic tubes to prevent ions from impacting on their surface with sufficient energy to cause sputtering. After the first test, already after a short operating time the tube showed visible erosion, which can be seen in Fig. 8.4. The ceramic tube is eroded down to the tungsten wire. Also, the 90° turns at the ends of the wire bridge became very fragile due to erosion. An additional test was executed where the thruster was run with the previously used light bulb wires (Fig. 8.5) while the wire bridge was disconnected from the power source and the ground. The floating potential of the wire bridge was

measured to be 20 to 40 V, evidently insufficient to repel 700 eV ions.

In another experiment the distance of the closer end of the bridge to the thrusters exit was reduced from 14 mm to 1 mm, even though this was likely to increase the erosion. The neutral gas flow was again set to 2.6 sccm. A stable operation point could be found at 660 V anode voltage and 150 mA anode current. However, this was again no significant improvement, the overall ion flux appeared to be even less. The electric potential of the ceramic tubes and the wire disturbed the conditions in the near field plume region.

The lack of improvement combined with the erosion makes it very unlikely that this method could be used to improve the performance of the micro-HEMPT.

8.1.2 An electron source focused on the thruster axis simulation

The preliminary runs to identify the right parameters to reach steady state for the micro-HEMPT computer models always showed a strong dependence on the electrons source strength and position. It must be determined why the experiment with the electron source along the thruster symmetry axis did not show the desired improvement of performance.

Therefore, a new kind of simulation was needed to include the only main feature that has not been applied yet, the depletion of neutral gas due to ionization. Obviously, in this case the neutral gas needs to be considered dynamic during the plasma run, so that the replenishment of neutral gas by the inlet can be simulated. Also the 'recycling' of ions, meaning that each ion that impacts on a wall 'creates' a neutral atom, needs to be included. Furthermore, the super-particle to physical particle ratio is required to be the same, since different weighting for individual particle species was not fully implemented in the code (by the time of this work). This caused a very high count for the neutral super-particles and, consequently, high memory usage.

Although the neutrals are dynamic in this plasma run, it is not desirable to start with zero neutrals in this model. This is because the time step size used in the plasma run is too short to calculate the neutral gas evolution in an acceptable number of times steps. Therefore, a neutral run with an appropriate time step size is performed in advance of the plasma run. Its result is used in the initialization of the plasma run, as it was done in the previous HEMP thruster simulations. The same mass flow as in the previous micro-HEMPT models, 0.27 sccm, was used. As expected, the result is very similar to the previous neutral simulation. This proves that with the number of super-particles used for the previous runs the model was not too coarse.

The same geometric and magnetic field parameters were used as for the 14 mm chamber length, 1.5 mm chamber radius, 1 mm dielectric thickness version. Double-charged ions were not included since it was shown that they did not significantly contribute to the performance of the thruster, and omitting them simplifies the investigation of the relation between neutrals and ions. Since the number of neutrals being ionized before leaving the thruster are about 25 % for the micro-HEMPT it is assumed that the mean neutral density will drop to 75 % of its original value. To compensate for that, the electron source was increased from 14 mA to 21 mA.

The simulation run was started for the region of the electrons source being at the outer rim of the near field plume region, exactly as it was done in the previous simulation. When the run was close to reaching steady state it was split up into two runs. One continued with this spatial distribution of the electron source, while the other one focused the source at the thrusters axis while keeping the value of 21 mA. Comparing the evolution of these two runs is supposed to show how, if at all, performance changes with a focused electron source.

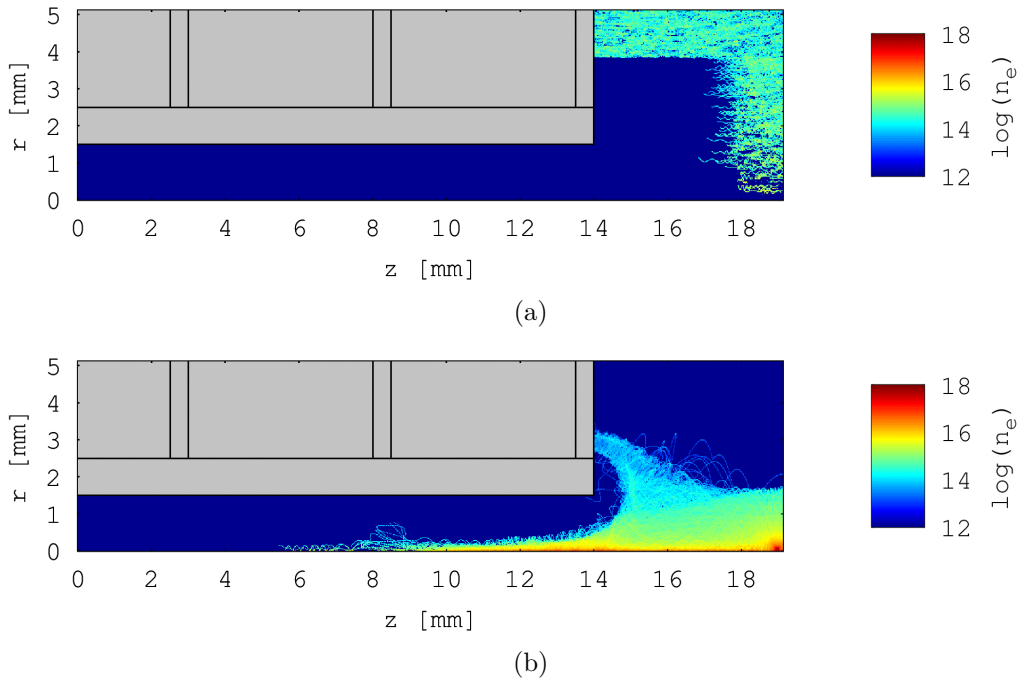

Figure 8.6: Electron density profile [log10(m^{-3})] after 1000 time steps for a) electron source at outer rim, and b) focused on z-axis.

A very brief test already shows an effect that was not anticipated and not related to the neutral gas depletion (time too short to play any role, less than

one neutral particle PiC-cycle). After only 1000 time steps the electrons have diffused strongly towards larger radii (Fig. 8.6). Even with the radii of their starting points being so close to zero, they undergo many oscillations near the exit cusp before they can pass it. Due to the time spent, this is enough for normal and anomalous diffusion to take effect. The effect of the focused source is therefore strongly diminished. To avoid this problem, all electrons would need to start at exactly $r = 0$, which is practically impossible due to the finite thickness of a tungsten wire.

The spatial plasma density profile and electric potential remained quite similar to the previous run. Therefore, this analysis will focus on the evolution over time regarding the overall number of ions and neutrals. in Fig. 8.7 the evolution of the overall ion number over time is displayed. It shows an almost constant decrease from the high original number of ions and electrons the simulation was initialized with. As expected, the number of neutrals which can be seen in Fig. 8.8 is also decreasing, presumably as discussed before, towards 75 % of its original value. Both numbers appear to level out over time. At $1.49 \cdot 10^7$ time steps, the model is branched into the two versions of electrons sources as described before. As expected the model where the electron source remains at the outer rim shows no change in the way the number of ions and neutrals evolve. For the model with the focused electron source the ion number rapidly rises, but then quickly levels out at about one-and-a-half of its original value. From there, the decline continuous at a rate similar to the previous model. The neutral number rapidly drops, but then continues at a faster but not by orders of magnitude larger reduction rate. The neutral density profiles show in Fig. 8.9 a) the original neutral density before the plasma ignition. In b) is shown the latest state for the model with the electron source at the outer rim. It becomes clear that the strongest reduction in neutrals is near the z-axis where the most electrons are and most ionization occurs for this type of thruster. As can be seen in c), where the electron source is focused towards the z-axis, the neutral depletion is even stronger near the z-axis.

It can be concluded, that the neutral gas reacts to focused electrons by localized depletion. This in turn strongly limits the increase in ionization rate. Also, in general, increased source electron strength and subsequently higher ionization decrease the overall number of neutrals, which also levels the ionization rate. Therefore, for sufficient electron strength further increase or focusing does almost not effect the ionization rate. Also, there is significant diffusion of electrons even over a short distance towards the thrusters exit. This effect, combined with disturbance by a real electron source (electric potentials, partial blocking of the ion beam) should explain why there was no significant improvement in the performance of the thruster in the experiment with the focused neutralizer.

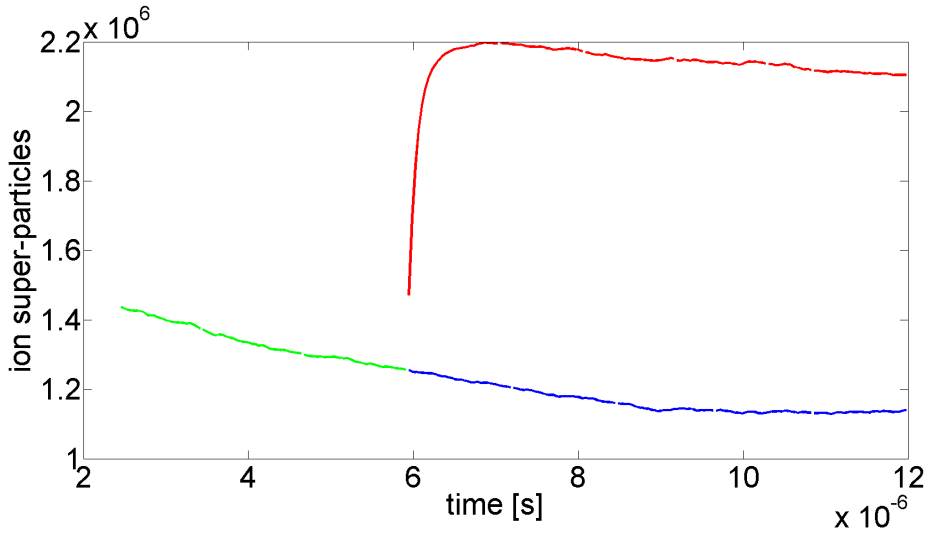

Figure 8.7: Evolution of ions with time. Green/blue outer rim electron source; red focused electron source.

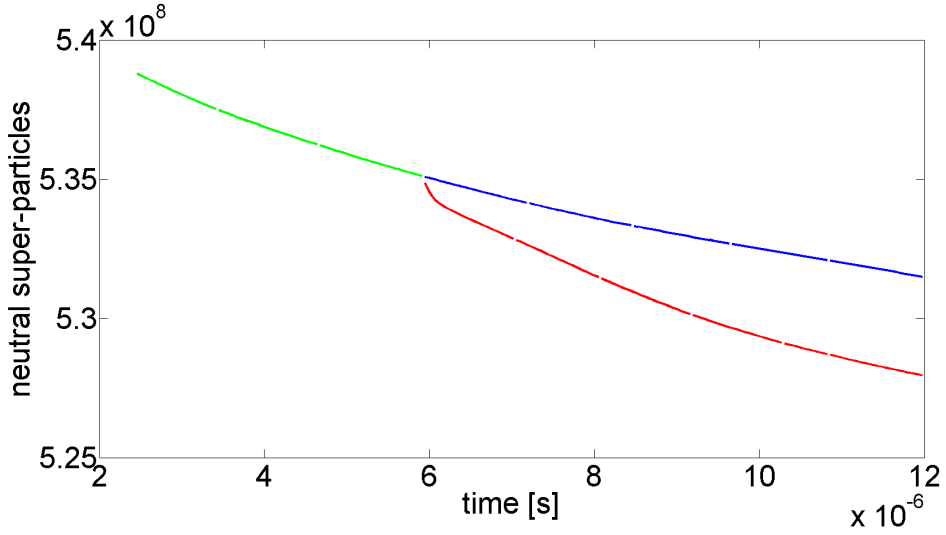

Figure 8.8: Evolution of neutrals with time. Green/blue outer rim electron source; red focused electron source.

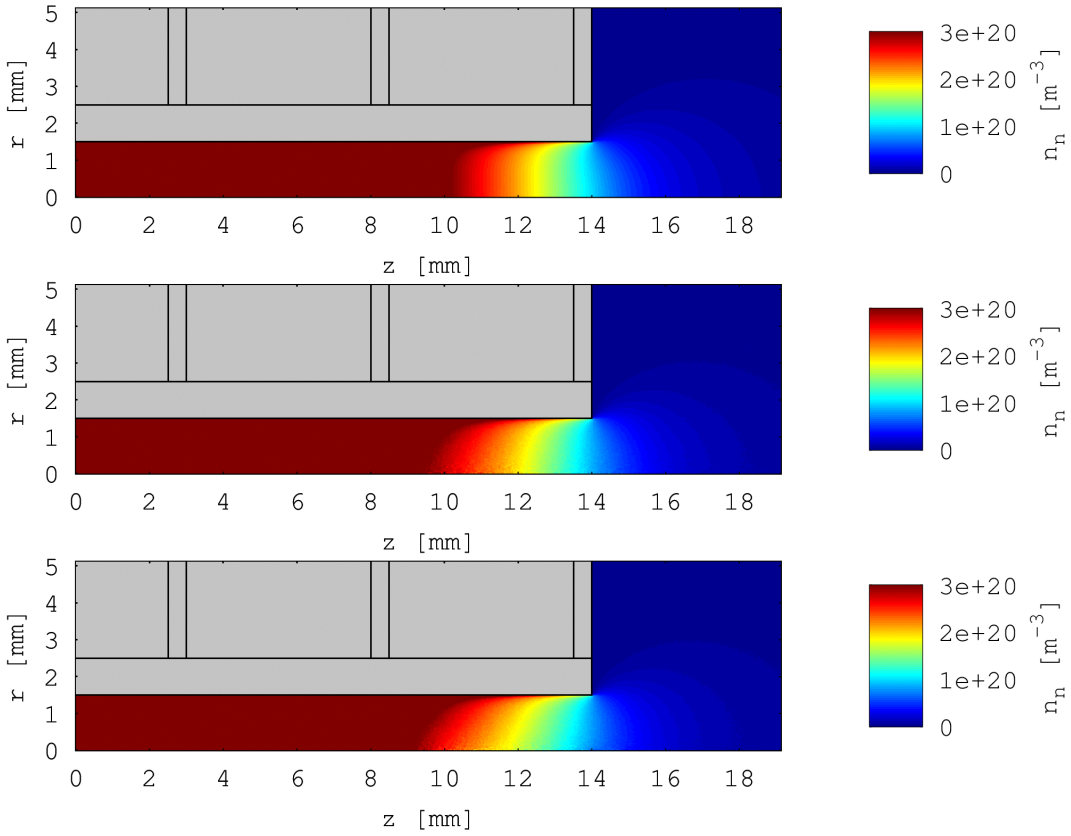

Figure 8.9: Neutral density profile. End of neutral run, outer rim electron source and focused electron source (upper, middle and lower picture). Color scheme limited to $3 \cdot 10^{20}$ m^{-3} to highlight the region near the thrusters exit.

8.2 Different thicknesses of distance rings

The specific shape of the magnetic field topology is essential for the efficiency of the magnetic confinement of the plasma. As described earlier (chapter 7.1) the setup that generates this field consists of ring magnets and distance rings with an axial thickness of 5 mm and 0.5 mm, respectively. These values are based on a build and tested device, which had improved performance characteristics compared to similar designs and these values are used throughout most simulations in this work. The simulations, however, allow for the opportunity to test many configurations in possible improvements of magnetic confinement. This chapter will be devoted to changes in the thickness of distance rings since changes in the thickness of ring magnets are not expected to cause substantial changes in the magnetic flux density. The thickness of the distance rings, consequently, determines the distance of the ring magnets to each other. It is expected, that for most cases further decreasing of this distance increases the maximum flux density at the cusp position. If this distance is down to zero,

however, fields might cancel each other out. Also, the weak iron of the distance rings focus and strengthen the magnetic field. With the distance rings thickness being zero, and consequently, them being non-existent, this effect obviously vanishes.

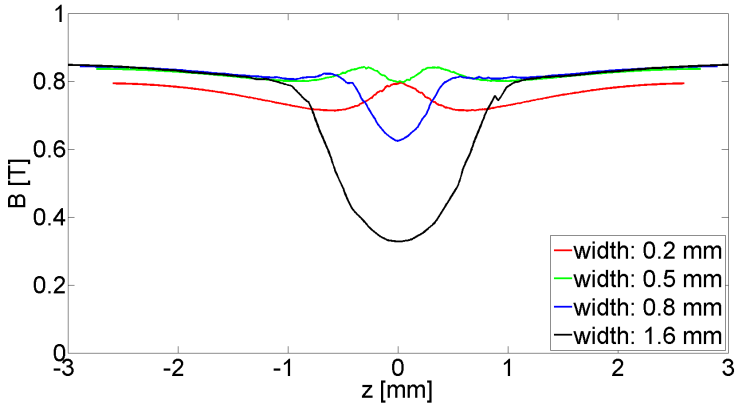

Figure 8.10: Magnetic flux density along dielectric surface.

In general, the strongest magnetic flux density of the magnetic cusp is along the chambers inner surface (dielectric surface), at the z-position of the cusp (chapter 2.5, Fig. 2.3). The strength at this position determines the efficiency of the magnetic mirror effect which has a significant contribution to the magnetic confinement.

To investigate the variation of this magnetic flux density strength in dependence of the distance ring thickness, magnetic field simulations are set up in the same manner as for the models of discharge chamber sections (chapter 6). The distances 0.2 mm, 0.5 mm, 0.8 mm and 1.6 mm are modeled. The second value of the four is the original distance. The thickness of the distance rings is kept the same.
In Fig. 8.10 one can see the magnetic flux densities for the various distance ring thicknesses along the dielectric surface. For simplicity, the starting point of the z-coordinates is set to the cusp position. It becomes evident that further reduction of the distance (from 0.5 mm to 0.2 mm) does not increase the magnetic flux density at the cusp position. Further increasing of the distance (from 0.5 mm to 0.8 mm and 1.6 mm) leads to a significant reduction of the magnetic flux density at this position.
It can be concluded that this permanent magnet setup, which is the result of several experiments, cannot be furthermore improved in this regard. Consequently, the magnetic profile cannot be improved by these method. The only apparent practical change would be using a thinner dielectric which would decrease the distance between the inner surface of both the ring magnets and

distance rings and the discharge chamber. Since the magnetic flux decreases with increasing distance from the cusp position, by this geometry change higher flux densities would be achieved in the discharge chamber. Another approach would be replacing the permanent magnets with electromagnets to overall increase the magnetic flux density. Both methods will be investigated in the following two chapters 8.3 and 8.4.

8.3 Simulating a downscaled HEMPT design with thinner dielectric

8.3.1 Setup including the magnets assembly adapted to thinner dielectric

The simulation discussed in this chapter is a direct iteration of the previous one, with the difference being that this one consists of a thin-film dielectric with 0.25 mm thickness for the discharge chamber, as opposed to a 1 mm thick hollow tube. This model setup serves for two purposes: first, with a thinner dielectric the magnet rings inner surface can be placed closer to the plasma. Since the magnetic flux decreases with the distance from the surface of the magnet the flux at the inner wall of the discharge chamber is greater than in the previous model. It shall be investigated, whether the expected increased magnetic confinement by the magnetic mirror effect increases the overall thruster performance. Second, to provide a micro-HEMP-thruster geometry that still would be somewhat typical for a normal-sized HEMPT when scaled up to its dimensions. As discussed in the simulations of discharge chamber sections, scaling up a model with inner chamber diameter 1.5 mm and dielectric thickness of 0.25 mm, by a factor of 6 yields 9 mm and 1.5 mm for these two numbers, which then are typical for a DM3a HEMP thruster. The length is with 84 mm unusually long for a DM3a, yet it has to be set this way in order to keep the geometry the same as for the micro-HEMPT. The micro-HEMPTs are designed with a relatively large length/diameter ratio to make the best use of the neutral gas despite a low ionization rate.

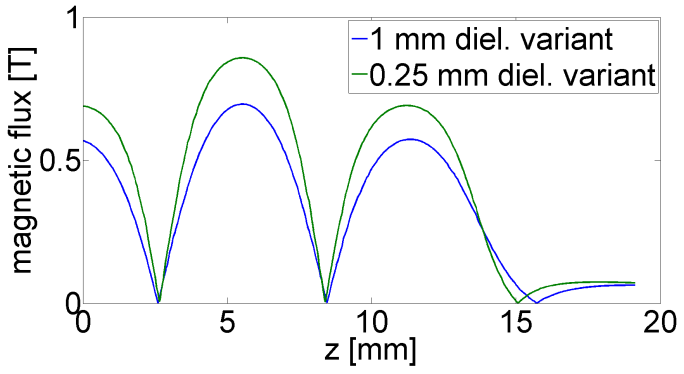

Figure 8.11: Micro-HEMPT magnetic flux along z-axis.

The magnet geometry and its simulation are in principle the same, only that the inner radius of the magnet and distance rings shifts from 2.5 mm to 1.75 mm due to the thinner dielectric. Fig. 8.11 shows the magnetic flux along the z-axis for this model and the previous one. The peak value has increased from

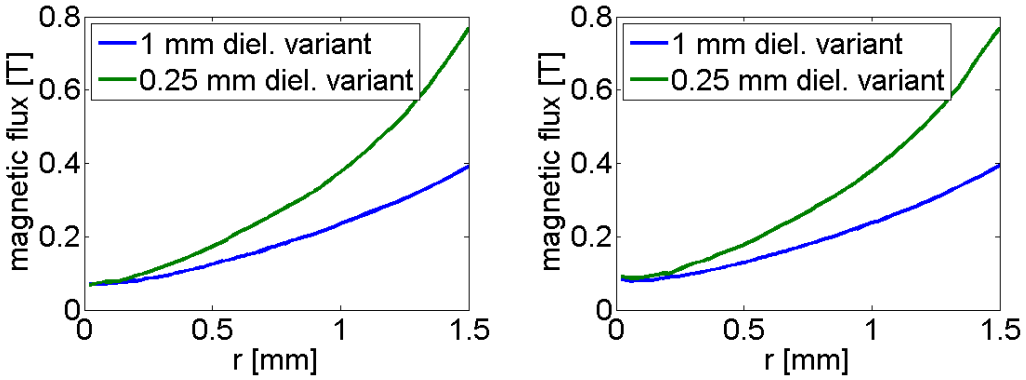

Figure 8.12: Micro-HEMPT magnetic flux at cusp1 a) and cusp2 b).

about 0.7 T to about 0.85 T. Accordingly, the diffusion from near the z-axis to the walls should be reduced, but obviously not by much. The zero-field point of the exit cusp is somewhat nearer to the anode with its position being shifted from about 1.6 mm to about 1.5 mm. Fig. 8.12 a), b) shows the magnetic flux along radial direction at the midpoint z-positions of the two distance rings related to the two cusps. Due to the asymmetry of a non-infinite periodic arrangement these positions are not exactly equal to the zero-field points. In all cases the maximum flux within the discharge chamber is at its maximum radius (1.5 mm). At both cusps this maximum flux has increased from about 0.4 T to about 0.74 T. This indicates the an increased magnetic confinement by the mirror effect.

For the neutral gas, the boundary conditions remain the same since neither the discharge chamber inner diameter nor its length are altered. The neutral gas flow remains the same (0.27 sccm) to have more shared parameters between the two models so that they could be better compared. Therefore, it was not necessary to make a new neutral gas simulation; the result from the previous model was taken.

For the electron source strength, it was originally intended to take the value from the previous model, which was 17 mA. However, it turned out that the simulated thruster reacted highly non-linear to the strengthened magnetic mirror effect. Using this source strength the resulting plasma density exceeded what the simulation grid was intended for. An increased grid resolution would have significantly increased the computation time. Instead, in an iterative process, a source strength was found that brought the anode current to a value similar to the previous model. The selected value is 7.5 mA. By use of this current strength, the plasma densities settled to values whose Debye lengths

were within the simulation grids resolution.

For the charged particles the boundary conditions also remained the same due to the unchanged discharge chamber parameters.

The electrostatic boundary conditions remain also mainly the same, only the beginning of the grounded area shifts from $r = 2.5$ mm to 1.75 mm. Also the maximum r-end of the anode potential shifts from $r = 2.5$ mm to 1.75 mm, yet this should not matter since only until $r = 1.5$ mm it has an influence on the potential of the plasma, beyond that it is shielded by the potential of the dielectric surface.

8.3.2 Discussion of results and comparison to reference model

The resulting electron and ion density profiles are shown in Fig. 8.13 a), b). They appear to be very similar to the model with 1 mm dielectric thickness. With the electron source strength selected for this model, the anode current of 6.1 mA is slightly higher than the 4.7 mA of the previous model. The same is true for the wall current of 7.0 mA towards the previous 6.1 mA.

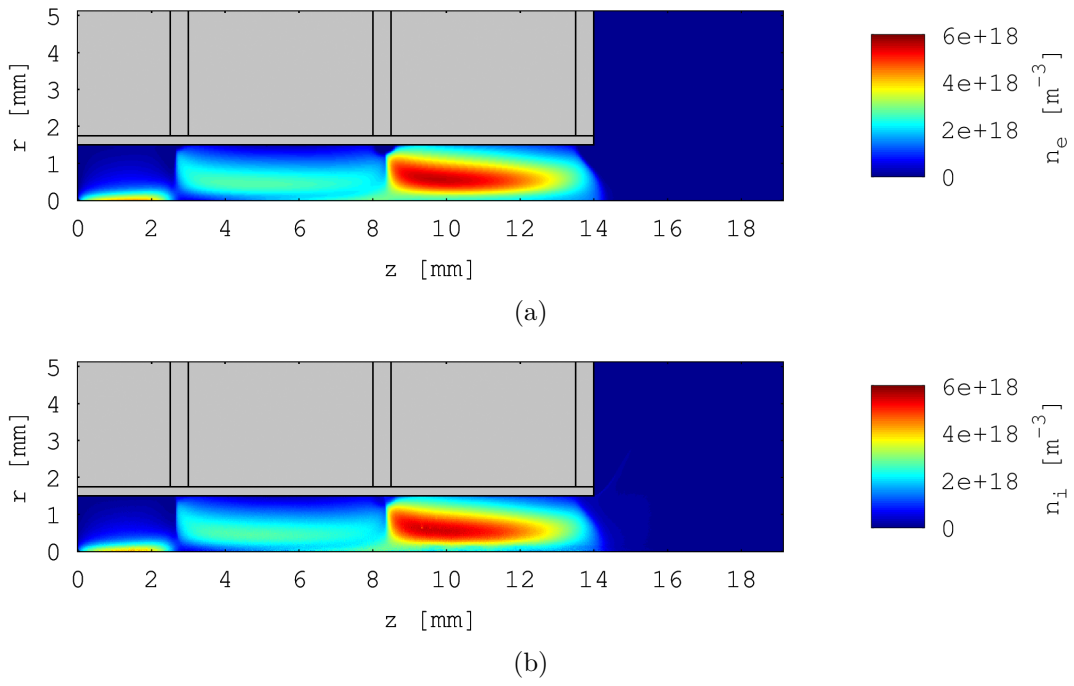

Figure 8.13: Denstiy profiles of a) electrons and b) ions (for the design with 1.75 mm inner diameter of the ring magnets).

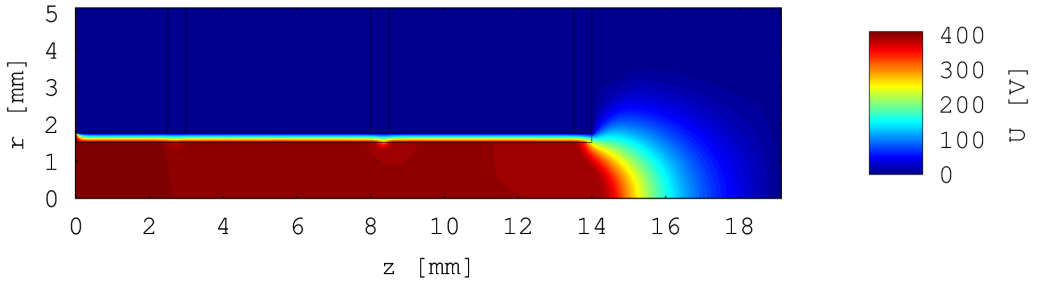

Figure 8.14: Micro-HEMPT potential profile (for the design with 1.75 mm inner diameter of the ring magnets).

Indeed, the ratio of the anode current to these wall losses has only slightly changed from 1.30 to 1.15. Yet the 0.25 mm dielectric version achieves these similar operational parameters with only about half as much source electrons (7.5 mA towards 17 mA). There must be a significant difference in how the source electrons are utilized in this version.

The electric potentials also appear very similar (Fig. 8.14). Yet a plot for the potential at the channel wall of both models highlights significant differences at the cusps z-position (Fig. 8.15). For the 0.25 mm version, the dips in the potential are only half as low. One can conclude that on average the electrons that reach the wall have only about half as much energy.

It can be further concluded that while the overall current to the wall remains similar the losses in high energy electrons are reduced. Obviously, the effect of the changed magnetic configuration is that the confinement time for the high energy electrons is increased, giving them more time to deposit their energy into the ionization process of the plasma.

A vast majority of the high energy electrons must originate in the electron source and gained energy in the main potential drop near the thrusters exit. Their utilization is decisive for the thrusters performance. This has also been seen in the findings in chapter 6.

A plot of the potentials along the thrusters symmetry axis from the anode position to the thrusters exit, given in Fig. 8.16, shows that they are very similar except that the 0.25 mm version has almost no drop at the second downstream cusp.

This observation might also indicate a higher fraction of high energy electrons which can easier overcome the cusp, due to their larger gyration radii. Thus, they increase the conductivity in the z-direction at this position.

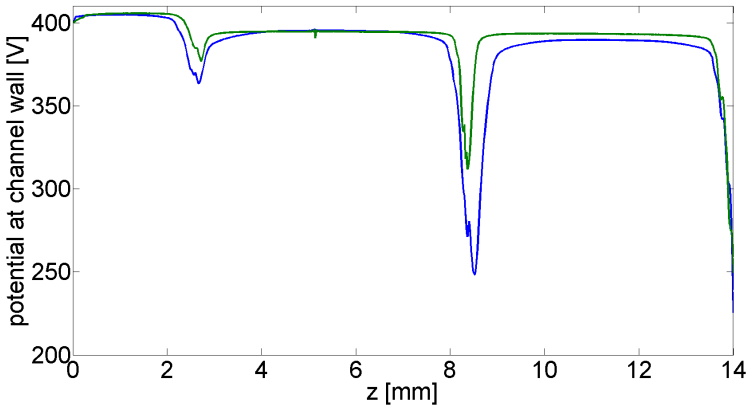

Figure 8.15: Micro-HEMPT potential at the channel wall (blue: 1 mm dielectric, green 0.25 mm dielectric variant).

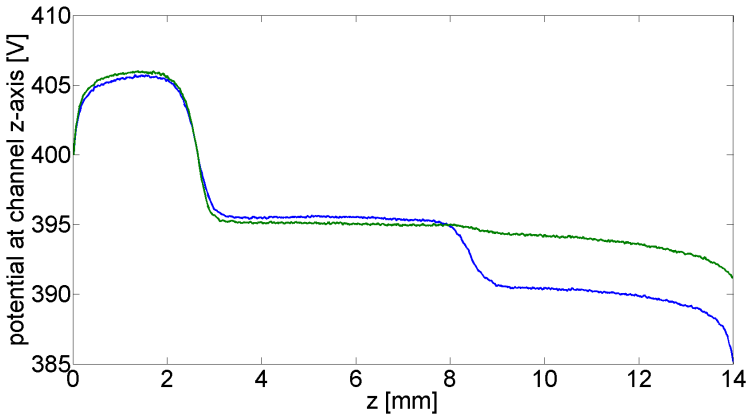

Figure 8.16: Micro-HEMPT potential at the channel z-axis (blue: 1 mm dielectric, green 0.25 mm dielectric variant).

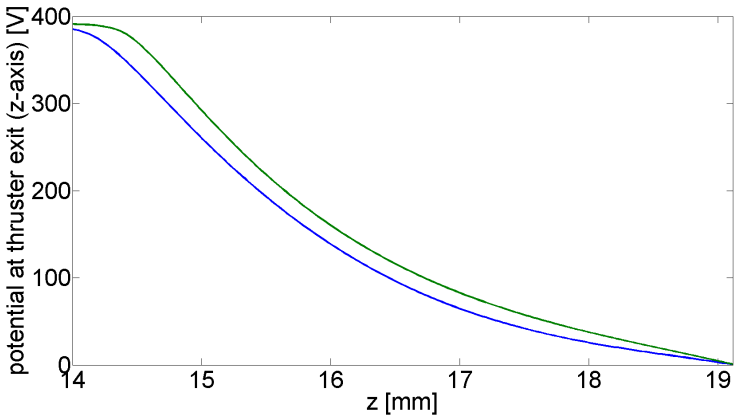

Figure 8.17: Micro-HEMPT potential at the thruster exit (z-axis) (blue: 1 mm dielectric, green 0.25 mm dielectric variant).

For the 1 mm version presumably more high energy electrons get lost to the wall at this position than to overcome the cusp. A continuation of this plot for the thruster exit region can be seen in Fig. 8.17. Between the 1 mm and 0.25 mm version is only very little variation in the potentials of the exit region.

8.4 Simulating the downscaled HEMPT with overall increased magnetic field

8.4.1 Theoretical considerations and setup for increased magnetic field

The simulations of discharge chamber sections (chapter 6) clearly showed the disadvantage of the micro-HEMPT due to its relatively weak magnetic confinement.
The ionization rate and, thus, the performance is reduced. Compensating this effect by increasing the neutral gas and, thus, increasing the ionization rate might be possible, but is not desirable due to the thrust-noise that the gas would produce. While there still might be some room for improvement in the magnets setup, the most important attribute seems to be the weak iron distance rings, who are already close to the optimal design (see chapter 8.2). The micro-HEMPT uses magnets made of Samarium-Cobalt, the strongest heat resistant material available. It has a magnet remanence of about 1 T and with the magnets setup the mean flux inside the micro-HEMPTs discharge channel is still 0.6 T. Nevertheless, according to the scaling laws this is 6 times less than required, compared to a normal sized HEMPT which is about six times larger. Superconducting electromagnets usually operate in a range from 10 T to 20 T. Hence in theory the 6 T could be easily achieved. Obviously, it is very doubtful whether it would be feasible to apply superconducting electromagnets to the micro-HEMPT, both due the high temperature gradient and due to undermining the simplicity of the original HEMPT concept. However, investigating such a setup could at least help to differentiate between the effect of increased magnetic confinement and larger amount of electrons being dragged inside due

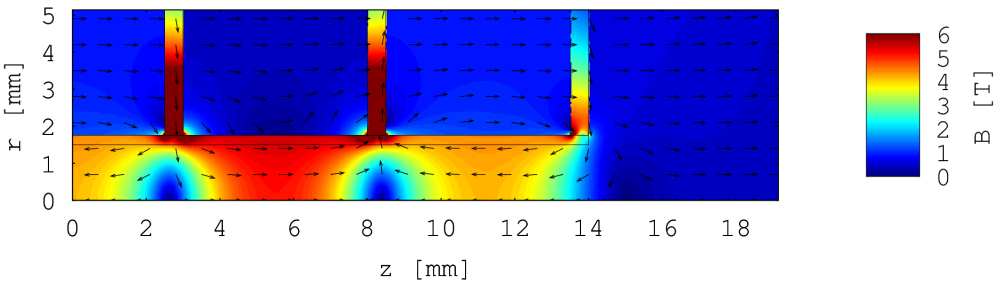

Figure 8.18: Micro-HEMPT with increased magnetic flux density.

to increased space charge as a consequence of a larger device. For simplicity, the magnetic field of the 0.25 mm dielectric micro-HEMPT version will just be increased by the factor 6 (Fig. 8.18). The technical details to achieve this by use of superconducting electromagnets will not be considered. The other setup parameters remain the same as in that simulation with one exception: It became quickly imminent that the plasma density was further increased beyond the grid resolution limits. Therefore, the source current strength was further reduced from 7.5 mA to 1.185 mA.

8.4.2 Discussion of results of an increased magnetic field

By the potential plot in Fig. 8.19 and its profile along the z-axis in Fig. 8.20 it can be recognized that again the dips in potential are smaller compared to the original. The bulk of the positive potential at the thrusters exit is of similar shape. In the enlarged version of the following chapter 9 this bulk does reach further out.
By the ion density profile in Fig. 8.21 one can conclude that the magnetic confinement is increased like in the enlarged version. This is not surprising, since in terms of magnetic confinement these two systems are self-similar to each other.

Also, like in the enlarged version, the flux to the wall is more focused at the cusps as shown in Fig. 8.22.

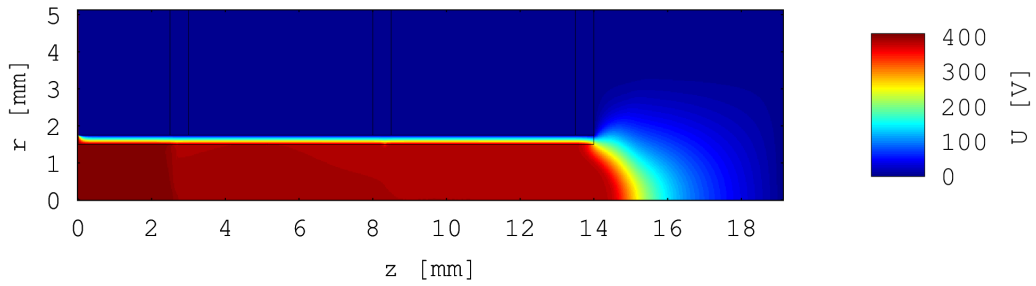

Figure 8.19: Potential profile (for the design with 1.75 mm inner diameter of the ring magnets, magnetic flux increases six times).

The anode current is 5.0 mA, and the wall losses are 4.5 mA, leading to only a slight improvement of the ratio to 0.9. Yet the multiplication factor (source current $\Rightarrow$ anode current) is with 4.2 much less than the one of the version who is enlarged according to the scaling laws (chapter 9). Table 8.1 shows the last three simulated models. It becomes evident, that with improved magnetic field this multiplication factor vastly increases.

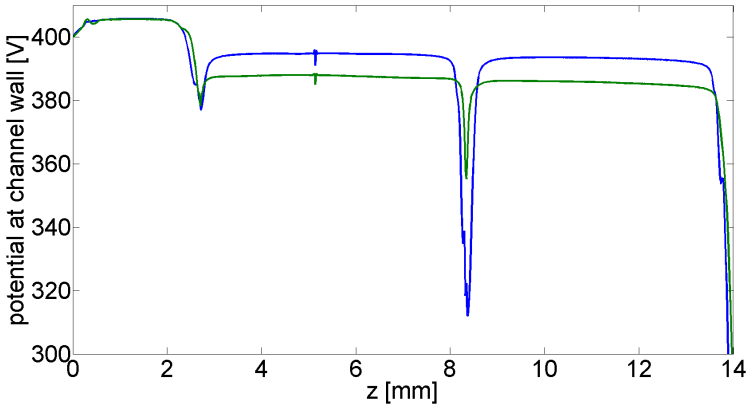

Figure 8.20: Potential at the channel wall of the conventional micro-HEMPT (blue) and with increased magnetic flux density (green); both with 1.75 mm inner diameter of the ring magnets.

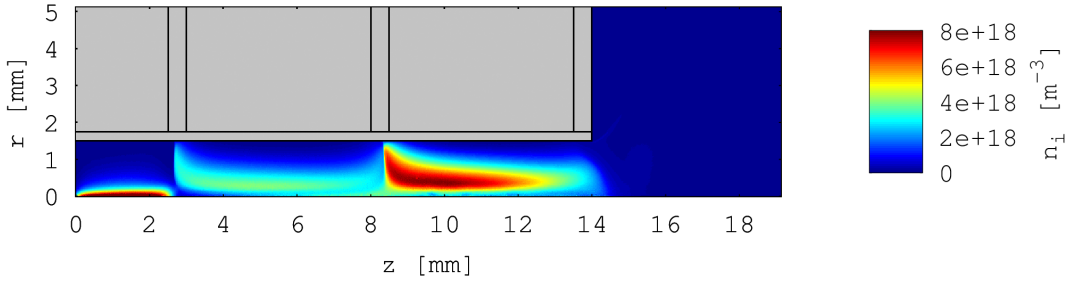

Figure 8.21: Ion density profile (for the design with 1.75 mm inner diameter of the ring magnets, magnetic flux increased six times).

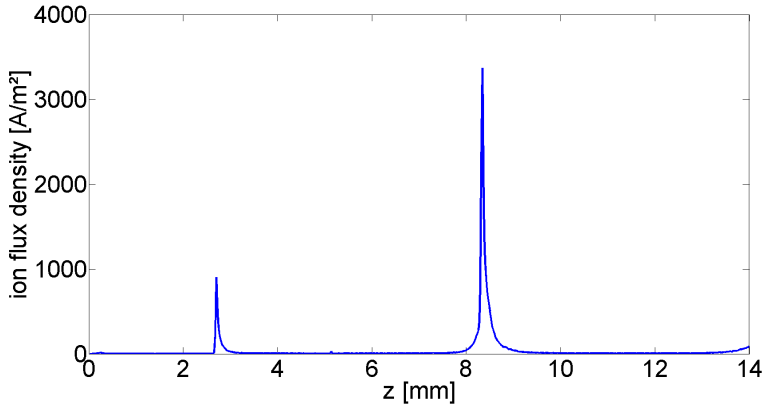

Figure 8.22: HEMPT ion flux at the channel wall (for the design with 1.75 mm inner diameter of the ring magnets, magnetic flux increased six times).

Table 8.1: Parameters of the last three HEMP thruster models. Labelled by dielectric thickness and maximum magnetic flux density inside discharge channel

	1.00 mm diel. max. B 0.7 T	0.25 mm diel. max. B 0.85 T	0.25 mm diel. max. B 5.1 T
Source	17.0 mA	7.5 mA	1.185 mA
Anode	4.7 mA	6.1 mA	5.0 mA
Wall	6.1 mA	7.0 mA	4.5 mA
Anode/Source	0.28	0.81	4.22
Wall/Anode	1.30	1.15	0.90

9 Comparison to original sized thruster

9.1 Setup with scaled geometry

As intended, the previous simulation can now be compared to a model scaled up into the dimensions of a DM3a HEMP thruster. To accomplish this, a model is created with the same geometry as that one with thinner dielectric (chapter 8.4), yet enlarged by a factor of 6. The discharge chamber radius changes from 1.5 mm to 9 mm and the dielectric thickness from 0.25 mm to 1.5 mm. The length of the discharge chamber changes from 14 mm to 84 mm. While unusually large for a DM3a HEMP this length ensures that the proportions are the same as in the previous models. The outside region near the thrusters exit of the simulation is also scaled six times from a square of side lenght 5.12 mm to 30.72 mm. This yields a simulation domain size of 144.72 mm times 30.72 mm.

The permanent magnets setup is also scaled accordingly. As expected, the magnetic field simulation (Fig. 9.1) yields the same maximum flux density as the model which also used permanent magnets (chapter 8.3). In consequence, this model and the previous one (chapter 8.4), which had increased magnetic flux density, are equivalent regarding the scaling law. This makes it of particular interest for investigation.

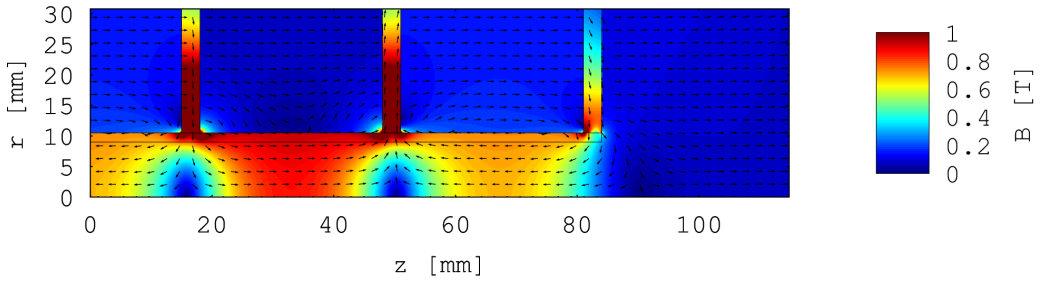

Figure 9.1: Magnetic flux density profile (for the design with 84 mm channel length and 10.5 mm inner diameter of the ring magnets).

As in the previous models a neutral gas simulation is performed in advance and the result is taken as static background for the plasma simulation. The neutral gas influx is increased by factor 6 from 0.27 sccm to 1.62 sccm in accordance with the scaling law. The density is consequently decreased by 6, as can be

seen in Fig. 9.2.

As described by the scaling law the anode voltage remains the same, which is 400 V.

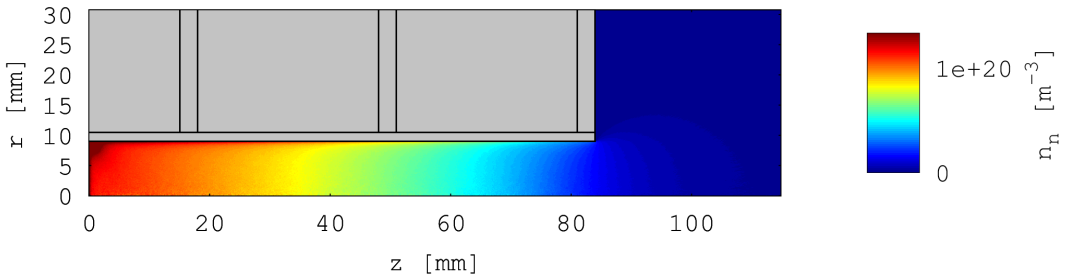

Figure 9.2: Neutral gas density profile (for the design with 84 mm channel length and 10.5 mm inner diameter of the ring magnets).

The regions of the electron source are also scaled up accordingly and remain at the outer rim of the near field region. Following the scaling law, the source strength would increase by 6 from 6 mA to 36 mA. Yet first runs of this model showed that this resulted in unreasonable high plasma densities. Therefore, the value was changed back to 6 mA, which also seemed more realistic because the intake of electrons might be quite similar, independent from the size of the thrusters exit. It was then further reduced to 1.5 mA. This of course reduces the possibility of comparison to the previous model to a rather qualitative level away from comparing absolute values. Yet it shows the large multiplication factor from source current to anode current that are typical for thrusters of this size. Even then, a high computational scaling factor had to be selected for the model in order to deal with the high plasma densities. To migrate the effect of scaling on the potential profile, which could be seen in chapter 5.5, the grid resolution was doubled in both dimensions, from 256 times 956 to 512 times 1912. The selected scaling factor was 144, which by the given grid resolution yields a maximum sustainable plasma density of $2.88 \cdot 10^{21}$ $1/\mathrm{m}^3$. This is equivalent to an unscaled model having a maximum density of $2 \cdot 10^{19}$ $1/\mathrm{m}^3$. This is two times larger than the previous model, although it should be six times smaller, even with 36 mA source current. This already showed that a thruster of this size must have a vastly more efficient ionization than its mirco-HEMPT counterpart. The results will be evaluated with a special focus why this is the case.

9.2 Comparison of the results to the micro-HEMP thruster

The resulting electric potential is shown in Fig. 9.3. Although the main principle of a mostly flat potential inside the discharge channel remains the same, a closer look reveals two divergences compared to the model in chapter 8.3. The dips in the potential at the cusps position are much smaller, only about 10 V as opposed to about 100 V, and the 'bulge' of positive potential reaches further out of the thrusters exit. The former reflects the result what was already seen in the simulations of discharge channel sections with a magnetic cusp (chapter 6). When the channel section was enlarged from $z = 5.5$ mm, $r = 1.5$ mm to $z = 3.3$ mm, $r = 9$ mm, while keeping the magnetic field constant, the dip at the cusp position became much less prominent. It was concluded that the magnetic confinement, in particular for the high energy electrons was improved in the larger configuration. Therefore, the mean energy at which the electrons impact the discharge channel wall at the cusp position is reduced. Obviously, this is here the case, too. The consequence is the higher ionization rate, as more energy of the electrons is deposited into ionizing collisions before they impact the wall.

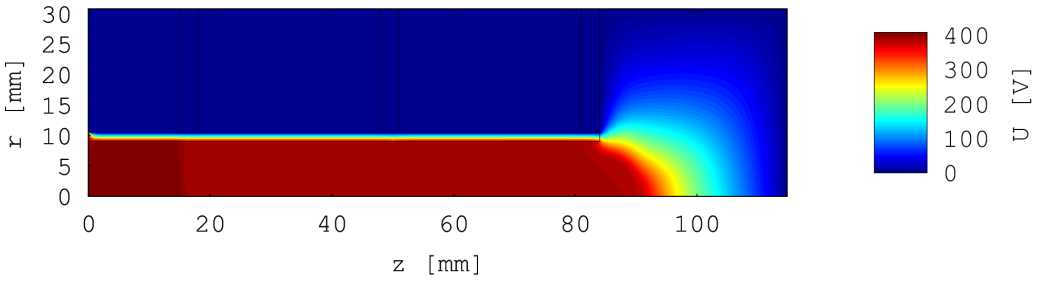

Figure 9.3: Potential profile (for the design with 84 mm channel length and 10.5 mm inner diameter of the ring magnets).

The potential of this model and the downscaled model along the z-axis can be seen in Fig. 9.4. The z-distances of both models are normalized to the discharge channel length to enable a comparison. Thereby, it becomes evident that the positive potential reaches further out in case of the larger system (in relation to the system size). Consequently, more source electrons are drawn into the thrusters exit which also helps to explain the larger multiplication factor.

One can see in the ion density profile in Fig. 9.5 that the plasma follows more strictly the magnetic field topology than it is the case for the micro-HEMPT. This was also already seen in the simulations of discharge chamber sections (chapter 6). When the system is scaled up while keeping the same magnetic flux density as the micro-HEMPT this effect equals an increase in magnetic flux

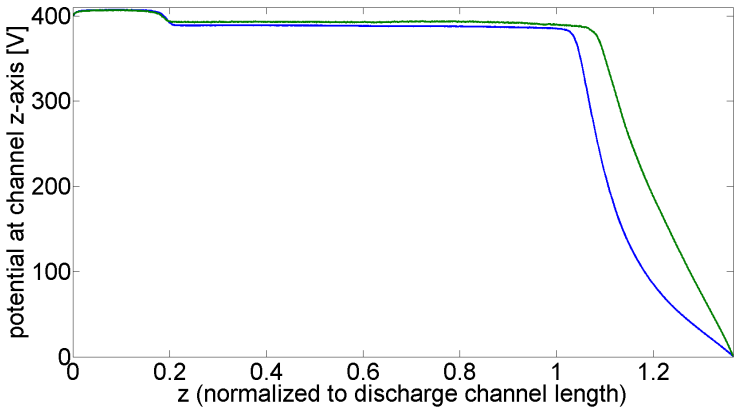

Figure 9.4: Potential at the channel z-axis of the micro-HEMPT (blue) and 84 mm (channel length) HEMPT (green). Channel lengths normalized to 1.

density relative to the values derived from the scaling law. Consequently, this model is stronger influenced by the magnetic field than the mirco-HEMPT. Vice Versa, the micro-HEMPT configuration equals a weaker magnetic field and, obviously, its plasma is more diffuse.

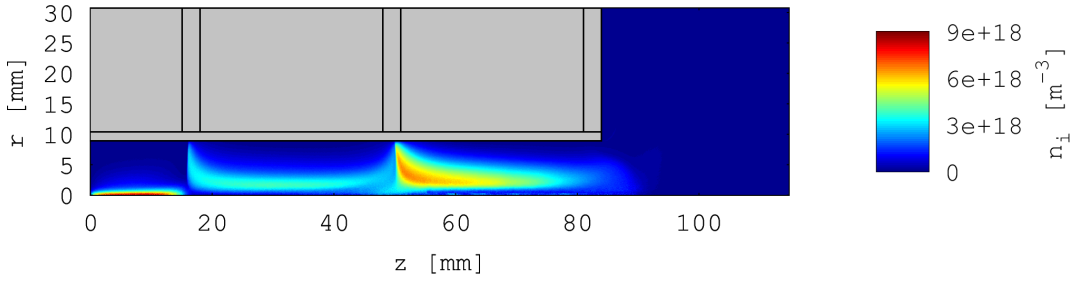

Figure 9.5: Ion density profile for the design with 84 mm channel length and 10.5 mm inner diameter of the ring magnets.

In Fig. 9.6 it can be found that the ion current towards the wall is more focused at the cusps positions, as one would expect from the previous findings.

The anode current is 145 mA. Consequently, the multiplication factor is 96.7 (1.5 mA source current). This is significantly higher than it is the case of the micro-HEMPT with 0.25 mm dielectric, where this factor was only 0.81. The wall losses are 105 mA, leading to an wall loss to anode current ratio of 0.72. While this is lower than the ratio from the micro-HEMPT, which was 1.15, the huge difference in performance can obviously not be explained by this ratio alone. Again, this was seen in the discharge chamber section simulations, where this ratio also undergoes only minor changes from micro-HEMPT sized

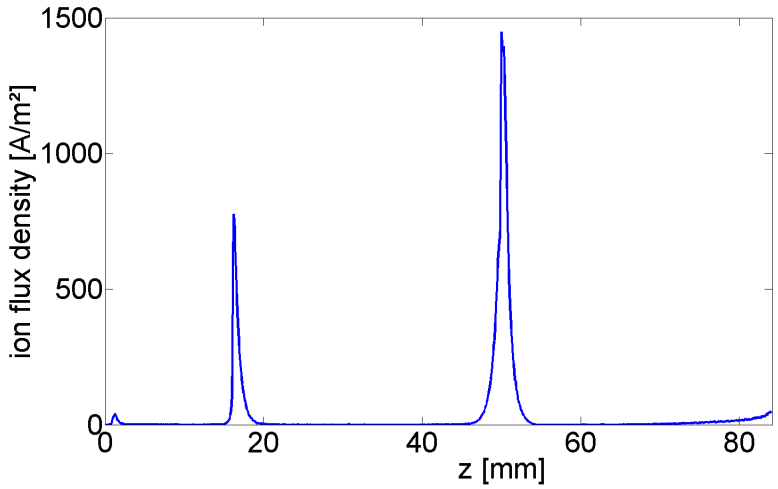

Figure 9.6: Ion flux at the channel wall (for the design with 84 mm channel length and 10.5 mm inner diameter of the ring magnets).

model to the normal sized model.

This becomes more evident by comparing this model to the micro-HEMPT with 0.25 mm dielectric and increased magnetic field, which is the self-similarity equivalent to the model investigated here. There the wall loss ratio is with 0.90 similar to the value 0.72 seen here. It shows that, as expected, the self-similarity works relativity well. Nevertheless, the difference in the multiplication factor is with 4.22 to 96.7 still very large. This can be explained by the deviations in space charge and consequently electric potential in the exit region, which attracts the source electrons. Table 9.1 gives an overview for the results of the discussed last three models.

It can be summarized that two factors contribute to the superior performance of the larger system: first, the larger size creates larger space charges which in turn enlarge the bulk of positive potential that reaches out of the thruster exit. In consequence, more electrons are drawn into the thrusters exit which otherwise would be repelled by the magnetic mirror effect. Second, the improved magnetic confinement works especially for the high energy electrons and, thereby, improves the ionization process. The reverse of these findings explains the relatively low performance of the micro-HEMPT.

It can be concluded that while in principle the same magnetic confinement inside the discharge channel can be achieved (chapter 8.4), the amount of electrons that are dragged inside by the enlarged version cannot be reproduced by the micro-HEMPT.

Table 9.1: Parameters of the last three HEMP thruster models. Labelled by dielectric thickness and maximum magnetic flux density inside discharge channel.

	0.25 mm diel. max. B 0.85 T	0.25 mm diel. max. B 5.1 T	1.5 mm diel. max. B 0.85 T unscaled
Source	7.5 mA	1.185 mA	1.5 mA
Anode	6.1 mA	5.0 mA	145 mA
Wall	7.0 mA	4.5 mA	105 mA
Anode/Source	0.81	4.22	96.7
Wall/Anode	1.15	0.90	0.72

10 Conclusion and outlook

In the thesis, numerical simulations of unscaled and downscaled HEMP thrusters and elements of them were performed in detail. A commercial PiC code (VSim, TechX cooperation), was used to gain experience in kinetic simulations. Afterward, a PiC code, written in C-language, developed at the University Greifswald, was used and adapted to the specific tasks.

A self-similarity scaling schema, originally developed by Taccogna et al., has been investigated in more detail for unbound plasma, bounded plasma, and a cylindrical plasma thruster.

A set of scaling laws for a plasma thruster has been found which agrees with the literature.

Some deviations from the scaling laws are investigated which resulted from the application of permanent magnets. The diffusion of electrons perpendicular to magnetic field lines increases with a weaker field. This has consequences for wall losses of the electrons, plasma confinement, and eventually thruster efficiency. Due to the use of permanent magnets, the magnetic flux density cannot be increased for a downscaled system in the manner that the scaling law demands. The flux density of the magnets setup remains unchanged for a scaled geometry. The consequences had been investigated both by analytical methods and by computer modeling, each for sections of the discharge chambers. The results showed lower ionization efficiency. The main reason was determined to be a lower confinement inside the channel particular of high energy electrons. The larger gyration radii of high energy electrons make them more prone to diffusion in a relatively weak magnetic field.

The magnetic cusp structure in the discharge chamber was also investigated. The different behavior of a downscaled configuration that uses permanent magnets becomes evident. In particular, this is visible in the electron and ion distribution, the profile of the electron and ion fluxes at the discharge chamber wall as well as the electric profile. For example, the maxima of the charged particle densities (ions and electrons) shifted to higher radii due to increased diffusion in the downscaled system

The next step was to set up a computer model for a downscaled HEMP thruster, including the near field region beyond the end of the thrusters discharge cham-

ber. By this approach, the physical characteristics of this thruster version (that could not be examined by diagnostics due to the size) could be determined. The angular ion beam distribution showed a relatively good agreement with the experimental data, considering the relatively small near field exit region.

The electric potential is mostly flat throughout the discharge channel and its value is close to the anode potential. The same is the case for the original sized HEMPT. Therefore, it can be assumed that the working principle remains the same as in the downscaled configuration. There are, however, structural differences. As in the simulation of discharge channel sections, for the downscaled configuration, the maximum of the plasma density has shifted to higher radii. This is for all cases due to the higher diffusion under the condition of a magnetic field that is weaker than the scaling law requires.

After these characteristics have been determined, attempts were made to apply the gained knowledge in order to retain the performance values of the original sized HEMPT.

Among the modifications that were looked upon was an electron source which is focused to the thrusters symmetry axis, both investigated in experiment and simulation. The experiment with the focused electron source showed no improvement in the ionization efficiency (visible by the anode current and the ion beam). The simulation revealed that even with their origin being close to the thrusters symmetry axis, the electrons diffuse significantly at the exit cusp, causing them to disperse to higher radii. There it is less likely that they enter the thrusters discharge chamber. Nevertheless, some more electrons enter the chamber than it is the case with a neutralizer positioned in a conventional way. The resulting larger amount of high energy electrons increases the ionization. This, however, leads to stronger depletion of the neutral gas. The reduced amount of neutral gas than levels the ionization rate. In the simulation, the electron source is idealized and causes no disturbance. In the experiment it does, which apparently counteracts the remaining positive effect that this particular electron source is supposed to bring.

Also, a small parametric study was undertaken to determine whether variations in one decisive factor of the magnetic setup can lead to an improved magnetic field topology. This factor is the distance between the magnetic rings. It turned out that no noticeable improvement could be obtained and, hence, the thruster design that served as the basis for these models is already optimal in that regard.

Furthermore, use of a thin dielectric coating instead of a dielectric tube has been investigated. The result: the use of a thinner dielectric medium brings

finally a stronger magnetic field inside the chamber. This is because the magnets are closer to the discharge chamber. The simulation for a model that uses thinner dielectric showed significant improvement in ionization efficiency, which can be related to improved magnetic confinement. With a change from 1 mm to 0.25 mm, however, the dielectric thickness already approaches zero. Therefore, no further significant improvement is to be expected.

In a rather academic investigation, the model using the 0.25 mm thick dielectric is altered by increasing the magnetic field strength six times. The ionization efficiency is furthermore improved. A laboratory application would require the use of electromagnets instead of permanent magnets.

An advantage of this particular setup is that it can serve as a basis for a model of an unscaled HEMPT with the same geometric shape as a micro-HEMPT. This model is six times larger and according to the scaling law the magnetic field is six times weaker, which is then again achievable by permanent magnets. A computer model had been set up accordingly. In the result, the ionization efficiency was vastly improved, visible by the multiplication factor from source current to anode current, which is almost two orders of magnitude higher than for the previous model. the bulk plasma inside the discharge channel follows relatively closely the scaling law, therefore its performance characteristics should remain similar to the downscaled version, as long as the electron inflow follows the scaling law as well. Therefore, the origin of this significant deviation is supposed to be for the most part in the near exit field region. Indeed, the positive potential within the exit region reaches much further out. This can be contributed to the overall larger space charge of the model. The positive potential can pull more source electrons inside the thruster against the resistance of the magnetic mirror effect. Going backward from this fact, it concludes that the reduced space charge is an inherent problem for the downscaling of HEMPT.

The characteristics of a downscaled HEMPT were defined and studied in this work. It has been shown that the main methods of changing the micro HEMPTs characteristic have no proper perspective for improving its operation. One exception is replacing the permanent magnets with electro magnets. This, however, would negate the original premise of the HEMPT being a very simple and robust design. Future works might investigate in more non-conventional means to the improvement of a micro-HEMPTs performance. Even if it would lead to no directly applicable results, a lot could be learned about the plasma properties of unusually small electric thrusters.

Furthermore, the investigated effects hint to possible increased performance for unusually large, high power HEMP thruster, which are not developed yet.

Works published in scientific journals

Eur. Phys. J. D (2015) 69: 145
Simulations on the influence of the spatial distribution of source electrons on the plasma in a cusped-field thruster
Tim Brandt, Thomas Trottenberg, Rodion Groll, Frank Jansen, Franz Georg Hey, Ulrich Johann, Holger Kersten, Claus Braxmaier

Trans. JSASS Aerospace Tech. Japan Vol. 14, No. ists30, pp. Pb 235-Pb 242, 2016
Particle-in-Cell Simulation of a Down-Scaled HEMP Thruster
Tim Brandt, Ralf Schneider, Julia Duras, Daniel Kahnfeld, Franz Georg Hey, Holger Kersten, Frank Jansen and Claus Braxmaier

Bibliography

[1] B.D. Tapley, *The GRACE mission: status and performance assessment*, Eos. Trans. AGU **83**(47), Fall Meet. Suppl., Abstract G12B-01 (2002)

[2] C.W. Everitt et al., *2011 gravity probe B: final results of a space experiment to test general relativity*, Phys. Rev. Lett. **106**, 22110 (2011)

[3] P. Amaro-Seoane et al., *Low-frequency gravitational-wave science with eLISA/NGO*, Class. Quantum Grav. **29**, 124016 (2012)

[4] B. P. Abbott et al., *Observation of Gravitational Waves from a Binary Black Hole Merger*, LIGO Scientific Collaboration and Virgo Collaboration; Received 21 January 2016; published 11 February 2016

[5] H. M. Lee , E.-O. Le Bigot, Z. H. Du, et al., *Gravitational wave astrophysics, data analysis and multimessenger astronomy*, Sci China- Phys Mech Astron, 2015, **58**(12): 120403

[6] W. P. Wright, P. Ferrer, *Electric micropropulsion systems*, Prog. Aero. Sci., vol. **74**, pp. 48-61, 2015

[7] A. Keller, P. Köhler, D. Feili, M. Berger, C. Braxmaier, D. Weise, U. Johann, *Feasibility of a down-scaled HEMP-Thruster*, IEPC-2011-138

[8] F. G. Hey, A. Keller, D. Papendorf, C. Braxmaier, M. Tajmar, U. Johann, D. Weise, *Development of a Highly Precise Micro-Newton Thrust Balance*, proceeding, 33rd International Electric Propulsion Conference, At The George Washington University, Washington, D.C., USA

[9] G. Kornfeld, N. Koch, G. Coustou, *FIRST TEST RESULTS OF THE HEMP THRUSTER CONCEPT*, Thales Electron Devices GmbH, Soeflinger Straße 100, D-89077 Ulm, Germany

[10] A. Cadiou, M. Lyszyk, and M. Dudeck, *26th International Electric Propulsion Conference*, paper IEPC-99-007 (Kitakyushu, Japan, 1999)

[11] K. Shinano, and H. Itô, *Behavior of a Charged Particle in a Cusp Field*, J. Phys. Soc. Jpn. **21**, pp. 1822-1829 (1966)

[12] K. Matyash, R. Schneider, A. Mutzke, O. Kalentev, *Comparison of SPT and HEMP thruster concepts from kinetic simulations*, IEPC-2009-159

[13] F. Taccogna, S. Longo, M. Capitelli, R. Schneider, *Particle-in-Cell Simulation of Stationary Plasma Thruster*, Contrib. Plasma Phys., 2007, **47**, 635-656

[14] A. Keller, P. Köhler, F. G. Hey, M. Berger, C. Braxmaier, D. Feili, D. Weise, U. Johann, *Parametric Study of HEMP-Thruster, Downscaling to μN Thrust Levels*, proceeding, 33rd International Electric Propulsion Conference, At The George Washington University, Washington, D.C., USA

[15] E. A. Witalis, *Hall Magnetohydrodynamics and Its Applications to Laboratory and Cosmic Plasma*, IEEE Transactions on Plasma Science (Volume:**14**, Issue: 6)

[16] K. Komurasaki, Y. Arakawa, *Two-dimensional numerical model of plasma flow in a Hall thruster*, Journal of Propulsion and Power, Vol. **11**, No. 6 (1995), pp. 1317-1323. doi: 10.2514/3.23974

[17] B. Dankongkakul, S. J. Araki, and R. E. Wirz, *Magnetic field structure influence on primary electron cusp losses for micro-scale discharges*, University of California, Los Angeles, California 90024, USA

[18] R.W. Hockney, J.W. Eastwood, *Computer Simulation Using Particles*, Adam Hilger, 1988

[19] D. Tskhakaya, K. Matyash, R. Schneider, and F. Taccogna, *The Particle-In-Cell Method*, Contrib. Plasma Phys. **47**, No. 8-9, 563 - 594 (2007)

[20] V. Khayms, *Advanced Propulsion for Microsatellites*, Thesis, Doctor of Philosophy, 2000

[21] A. Keller, *Feasibility of a down-scaled HEMP Thruster*, Doctoral Thesis, Konstanz, December 2013

[22] N. St. J. Braithwaite, *Introduction to gas discharges*, Plasma Sources Sci. Technol. **9** (2000) 517-527. Printed in the UK

[23] M. A. Lieberman, A. J. Lichtenberg, *Principles of Plasma Discharges and Materials Processing*, Wiley-Interscience, 2nd edn. 2005

[24] W. J. Moore, *Physical chemistry*, Walter de Gruyter GmbH, 1986, ISBN 3110109794

[25] B. Chakraborty, *Principles of Plasma Mechanics*, New Age International Publishers

[26] F. Chen, *Introduction to Plasma Physics and Controlled Fusion*, (Plenum, New York, 1984), Vol. **1**, pp. 30-34. ISBN 978-0-306-41332-2

[27] H. Grad, *Theory of Cusped Geometries*, I. General Survey, NYO-7969, Inst. Math. Sci., N.Y.U., December 1, 1957

[28] P. J. Catto, X. Z. Li, *Particle Loss Rates from Electrostatic Wells of Arbitrary Mirror Ratios*, Physics of Fluids **28.1** (1985): 352-57. Web. 15

[29] G Gibson, W. C. Jordan, E. Lauer, *Physical Review Letters **5**: 141 (1960)*

[30] R. Van Norton, *The motion of a charged particle near a zero field point*, New York: New York University: Courant Institute of Mathematical Sciences, 1961

[31] J. Pedlosky, *Geophysical fluid dynamics*, (1987) Springer. pp. 10-13. ISBN 978-0-387-96387-7

[32] A. Down, *Electron Plasma Waves*, February 28, 2007

[33] A. Down, *Ion Acoustic Waves*, March 05, 2007

[34] F. C. Hoh, B. Lehnert, *Diffusion processes in a plasma column in a longitudinal magnetic field*, Physics of fluids **3**(4) 600 607 1960.

[35] R. Hockney, J. Eastwood, *Computer simulation using particles*, Adam Hilger 1981

[36] R. S. Rowland, R. Taylor, *Intermolecular Nonbonded Contact Distances in Organic Crystal Structures: Comparison with Distances Expected from van der Waals Radii*, doi:10.1021/jp953141+

[37] W. C. Hinds, *Aerosol Technology: Properties, Behavior, and Measurement of Airborne Particles*, Wiley-Interscience, New York 1999, ISBN 0-471-19410-7

[38] D. Christodoulou, *The Euler Equations of Compressible Fluid Flow*, doi:10.1090/S0273-0979-07-01181-0

[39] J. Spanier, E. M. Gelbard, *Monte Carlo Principles and Neutron Transport Problems*, Addison Wesley 1969

[40] M. Melzani, R. Walder, D. Folini, C. Winisdoerffer, *Differences between real and particle-in-cell plasmas: effects of coarse-graining*, DOI: 10.1142/S201019451460194X

[41] R.D. Sydora, *Low-noise electromagnetic and relativistic particle-in-cell plasma simulation models*, doi:10.1016/S0377-0427(99)00161-2

[42] J. P. Borism, R. A. Shanny, *On Numerical Simulation of Plasmas*, EDS Proceedings of the Fourth Conference

[43] Particle In Cell Consulting, LLC

[44] K. Matyash, *Kinetic Modeling of Multi-Component Edge Plasmas*, Ph.D. thesis, Ernst-Moritz-Arndt-Universit at Greifswald 2003

[45] C. Ren, *Introduction to Particle-in-Cell Methods in Plasma Simulations*, University of Rochester, The 2011 HEDP Summer School

[46] F. Taccogna, S. Longo, M. Capitelli et al., *Particle-in-cell simulation of stationary plasma thruster*, Contributions to Plasma Physics, **47**(8-9) 635-656 2007. DOI:10.1002/ctpp.200710074

[47] J.N. Reddy, *An Introduction to the Finite Element Method (Third ed)*, (2006) McGraw-Hill. ISBN 9780071267618

[48] C.K. Birdsall, A.B Langdon, *Plasma Physics via Computer Simulation*, Taylor and Francis Group

[49] J. W. Demmel, S. C. Eisenstat, J. R. Gilbert et al., *A supernodal approach to sparse partial pivoting*, SIAM J Matrix Analysis and Applications, **20**(3) 720755 1999

[50] X. S. Li., *An overview of SuperLU: Algorithms, implementation, and user interface*, ACM Trans Mathematical Software, **31** 302-325 2005

[51] K. Matyash, R. Schneider, A. Mutzke, O. Kalentev, *Comparison of SPT and HEMP thruster concepts from kinetic simulations*, IEPC-2009-159

[52] Yu. N. Grigoryev, V. A. Vshivkov, M. P. Fedoruk, *Numerical 'Particle-in-Cell' Methods: Theory and Applications*, Walter de Gruyter GmbH

[53] R. Schneider, A. Weiße, *Computational Many-Particle Physics*, Springer Verlag, 10. Dezember 2007

[54] G. E. P. Box, M. E. Muller, *A note on the generation of random normal deviates*, In: Annals of Mathematical Statistics, Jg. **29** (1958), Heft 2, ISSN 0003-4851, S. 610-611

[55] T. Takizuka, H. Abe, *A binary collision model for plasma simulation with a particle code*, J Comp Phys, **25** 205-219 1977

[56] H. Risken, *The Fokker-Planck Equation. Methods of Solutions and Applications*, Springer, Berlin u. a. 1996, ISBN 3-540-61530-X

[57] B. A. Trubnikov, *Particle interactions in a fully ionized plasma*, Reviews of Plasma Physics, **1** 105-204 1965

[58] S. T. Perkins, D. E. Cullen, S. M. Seltzer, *Tables and graphs of electron-interaction cross sections from 10 eV to 100 GeV derived from the LLNL Evaluated Electron Data Library (EEDL), Z = 1 to 100*, November 12, 1991

[59] C.K. Birdsall, *Particle-in-Cell Charged-Particle Simulations, Plus Monte Carlo Collisions With Neutral Atoms, PIC-MCC*, IEEE Trans. on Plasma Science, vol. **19**, no. 2, 1991

[60] Aalto University, N. Hyvoenen, *Computational methods in inverse problems*, Twelfth lecture

[61] *About Air Ions*, AlphaLab Inc.

[62] K. Matyash, R. Schneider, A. Mutzke et al., *Kinetic Simulations of SPT and HEMP Thrusters Including the Near-Field Plume Region*, IEEE Transactions on Plasma Since, **38**(9, Part 1) 2274 2280 2010. DOI:10.1109/ TPS.2010.2056936

[63] F. Taccogna, S. Longo, M. Capitelli, R. Schneider, *Self-similarity in Hall plasma discharges: Applications to particle models*, Physics of Plasmas (1994-present) **12**, 053502 (2005); DOI: 10.1063/1.1877517

[64] H. Ohtani, R. Horiuchi, *Open Boundary Condition for Particle Simulation in Magnetic Reconnection Research*, DOI: 10.1585/pfr.4.024

[65] D. P. Weaver, D. H. Campbell, E. P. Muntz, *Scaling Rules and Time Averaging in Molecular Dynamics Computations of Transport Properties*, Rarefied Gas Dynamics: Theoretical and Computational Techniques, Progress in Astronautics and Aeronautics, pp. 194-207

[66] N. M. Laurendeau, *Statistical thermodynamics: fundamentals and applications*, 2005, Cambridge University Press. p. 306. ISBN 0-521-84635-8., Appendix N, page 434

[67] F. Brand, *PLASMA PHYSICS*, School of Physics, University of Sydney NSW 2006, AUSTRALIA

[68] R. A. Bailey and K. G. Emeleus, *Plasma-electron oscillations*, Proc. Roy. Irish Acad. A, vol. **57**, p. 53, 1955

[69] Source: Hayashi NIFS report 2003, http://www.nifs.ac.jp/report/NIFS-DATA-079.pdf p.134

[70] Source: Hayashi NIFS report 2003, http://www.nifs.ac.jp/report/NIFS-DATA-079.pdf p.129

[71] Source: M. Hayashi, Journal of Physics D: **16** (1983) 581

[72] Source: http://jila.colorado.edu/ avp/collision data/ionneutral/IONATOM.TXT

[73] A. Keller, P. Koehler, W. Gartner, B. Lotz, D. Feili, P. Dold, M. Berger, *Feasibility of a down-scaled HEMP-Thruster*, IEPC-2011-138

[74] T. Brandt, Th. Trottenberg, R. Groll, F. Jansen, F. G. Hey, U. Johann, H. Kersten, and C. Braxmaier, *Simulations on the influence of the spatial distribution of source electrons on the plasma in a cusped-field thruster*, Eur. Phys. J. D (2015) **69**: 145

[75] D. G. Courtney and M. Martinez-Sanchez, *Diverging Cusped-Field Hall Thruster*, IEPC-2007-39

Danksagung

Zuerst möchte ich mich bei Herrn Prof. Holger Kersten, dem Arbeitsgruppenleiter der AG Plasmatechnologie der Christian-Albrechts-Universität zu Kiel bedanken. Er hat mir die Durchführung einer Dissertation mit diesem faszinierenden Thema ermöglicht.
Des Weiteren möchte ich mich bei meinen Arbeitsgeber und Betreuer Prof. Claus Braxmaier bedanken. Er ermöglichte es mir, mich schnell und problemlos im Deutschen Zentrum für Luft- und Raumfahrt (DLR) zurechtzufinden. Diese Doktorarbeit wurde am DLR Institut für Raumfahrtsysteme durchgeführt und finanziert, mit Dr. Frank Jansen als Betreuer.
Von ganzem Herzen bedanke ich mich bei meiner Familie, die immer an mich geglaubt und mich unterstützt haben.
Ein besonderer Dank gilt an die Arbeitsgruppe von Prof. Ralf Schneider der Universität Greifswald. Sie hat mir die Nutzung ihres Simulationscodes ermöglicht, mich in diesen eingearbeitet sowie mir Computerressourcen zur Verfügung gestellt.
Ein weiterer Dank gilt an die Arbeitsgruppe von Dr. Johann Ulrich von Airbus Friedrichshafen, welche mir experimentelle Daten zur Verfügung stellte, sowie die Durchführung eigener Experimente ermöglichte.
In dem Zusammenhang möchte ich mich auch bei dem Werkstattleiter Michael Brix der Universität Kiel bedanken, da er für meine Experimente die Bauteile entsprechend meinen Plänen anfertigte.
Auch bedanken möchte ich mich bei PD Dr.-Ing. habil. Rodion Groll (ZARM Bremen), welcher mir anfänglich bei der Entwicklung von Neutralgas-Simulationen half.
Bedanken möchte ich mich auch bei den Mitarbeitern der Firma Tech-X Corp., die mir mit ihrem kommerziellen Produkt erste Erfahrungen in der Particle-in-Cell Simulationstechnik ermöglichten.
Zuletzt bedanke ich mich bei Dr. Thomas Trottenberg, Mitarbeiter der Arbeitsgruppe von Prof. Holger Kersten, da er mir mit seiner Erfahrung wesentlich bei der qualitativen Verbesserung meiner Dissertation geholfen hat.

Erklärung

Ich versichere an Eides statt, dass die vorliegende Arbeit - abgesehen von der Beratung durch meine wissenschaftlichen Betreuer und der Verwendung der angegebenen Hilfsmittel - nach Inhalt und Form die eigene Arbeit ist. Die Arbeit hat weder ganz noch in Teilen an einer anderen Stelle im Rahmen eines Prüfungsverfahrens vorgelegen. Außerdem erkläre ich, dass diese Arbeit unter Einhaltung der Regeln guter wissenschaftlicher Praxis der Deutschen Forschungsgemeinschaft entstanden ist.

Kiel, den 20. Oktober 2017

_____

Vorname Nachname